Coupled Surface Acoustic Wave Cavities

By André Luiz Oliveira Bilobran
Supervised by Maurício Morais de Lima Jr.

Departamento de Física Aplicada y Electromagnetismo

Universidad de Valencia

Programa Oficial de Doctorado en Física 3126

November 2020

Maurício Morais de Lima Jr., profesor titular de la Universidad de Valencia,

CERTIFICA: Que la presente memoria "Coupled Surface Acoustic Wave Cavities" ha sido realizada bajo mi dirección en el Instituto de Ciencia de los Materiales, centro de la Universidad de Valencia, por André Luiz Oliveira Bilobran y constituye su Tesis para optar al grado de Doctor en Física.

Y para que así conste, en cumplimiento de la legislación vigente, presenta en el Departamento de Física Aplicada de la Universidad de Valencia la referida Tesis Doctoral, firmando el presente certificado.

Fdo: Maurício Morais de Lima Jr.

This thesis was done within the framework and received funding from

SAWtrain Network: European Union's Horizon 2020 research and innovation programme under grant agreement No 642688.

Abstract

Over the last two decades surface acoustic wave (SAW) propagating in periodic structures have attracted a great deal of attention and have been the basis of a vast number of investigations. SAW tags, for example, explore the possibility to use active or passive devices to encode information and use it in many applications, from traffic control, to security or identification of parts on conveyer lines. Much similar designs are used for sensing applications, especially of temperature and mass. In addition, a myriad of scientific advances have been made in the study of phononic crystals (PnCs). PnCs are defined as artificial materials made of periodic arrangement of scatterers embedded in a matrix, and they enable the control of the propagation of elastic waves. The growing interest in these structures arise from the exhibition of very interesting features, such as absolute acoustic band gaps – spectral bands where propagation of waves is forbidden independently of the direction of propagation – and also of dispersion curves with a negative slope – when the wave group velocity is antiparallel to the wave vector. Both effects allowed relevant experimental achievements. The former, for perfect mirrors, vibration isolation and acoustic filters. The latter, on flat superlenses, able to focus elastic

waves with a resolution that beats the diffraction limit. Such superlenses have potential applications in the fields of medical imaging or ultrasonic beam-based therapy. Moreover, the confinement of acoustic energy in carefully designed modes made possible the fabrication of very efficient waveguides. Defect modes lead also to functionalities such as filtering and multiplexing. All these functions can be achieved in a very tight space of the order of some acoustic wavelengths. Phononic crystals are similar to photonic crystals except for the peculiarities of elastic waves as compared to optical ones. Elastic waves can be strongly anisotropic and exhibit different combinations of shear and longitudinal polarizations. Also, surface modes almost always exist at the phononic crystal boundaries. Most studies of PnCs focus on the propagation of bulk acoustic or elastic waves. However, bulk elastic waves are generally generated outside the sample of interest. SAWs, on the other hand, can be conveniently excited at the surface of a piezoelectric solid.

Motivated to expand further the realm of possibilities granted by this kind of periodic structures we investigated the *coupling* between defects, i. e., cavities, introduced in the matrix of scatterers. Based on previous results, where the coupling between several cavities was achieved in a one-dimensional grid, we were able to achieve two key experimental results. First, the dynamical tuning of this cavities in one dimension. And second, the extension of this 1D coupling of cavities for a two-dimensional grid composed of rectangular pillars. That is, we

realized the simultaneous coupling of cavities on perpendicular directions. The major tool used to investigate these devices was a finite element method (FEM) simulation model. With the successful development of the model, we were able to predict the behavior of our devices with great accuracy.

Moreover, we present a third key result, reached in close collaboration with the group of Prof. Dr. Per Delsing of the Chalmers University of Technology, in Gothemburg, Sweden, during a temporary stay there. With the use of a SAW cavity at very low temperature we studied sources of loss in superconducting quantum circuits. More specifically, losses due to two-level systems (TLS). TLSs are tunneling states, regarded as an uncontrolled intrinsic systems, which have a broad distribution of energy splitting and can be thermally activated at low temperatures, being an important source of loss. Our results shed some light into the linewidth of the TLSs ensemble and suggest a way to mitigate TLS loss in superconducting qubits.

This thesis is structured as follows: on the Introduction we provide explanation of the basic concepts used throughout our work, accompanied by a brief historical introduction on each subject; on Methods we expose all the simulations models used for designing our devices and show fabrication and measurement details; on Results we display the most relevant simulation results achieved (with 2D and 3D simulation models) together with the experimental results, showing their agreement. Also, we write a section with the motivation, basic concepts and

experimental results of the investigation on TLSs derived from the collaboration with Chalmers. On Conclusion we summarize our findings and give future prospects which can arise from our discoveries.

To the surface acoustic wave aficionados.

Acknowledgements

Although it is me who is writing all the text, it was only through the support and effort of a big number of people that this work was made possible. Here I want to thank all these wonderful humans who made some contribution to this journey.

First and foremost, I would like to thank my supervisor, Mauricio, for giving me the opportunity to explore such a vibrant research field and for the close guidance throughout all these years. Thank you for all of your teachings. Special thank to Andrés as well for providing for our lab and helping me with such energy whenever needed, distinctively for the financial support in the end. To Alberto I thank for several insightful discussions about simulation tricks. Many many thanks for all of the SAWtrain network for the good vibes and exciting scientific discussions. In particular, I thank Emeline, Sixuan and all the people in Augsburg for making me feel like home during my one month stay there. I also thank those in Gothemburg for making my three month stay so pleasant and memorable, specially Gustav for being such an excellent host. I really enjoy it and was inspired by the swedish atmosphere. A special thanks to the PDI people for fabricating my samples, and

specially Paulo, for the decisive meetings. A big thank you to Antonio for doing all the interferometry measurements so well and with such a positive attitude.

I also want to thank those from the ICMUV for all the help. M Ángeles for the efficient work as secretary, Pascual for solving technical issues in the lab. ICMUV and IFIC friends and colleagues: Antonio, Eleonora, Victor (Pope), María José, Carlos, Alberto, Álvaro, Damián, Javi B, Miguel Angél, Nuria, Dani, Rosa, Mariluz, Victor, Giulia, Rebecca, Valentina, Martín. To the close friends who made the weekends more special. Ana, thank you so much for the weekends in Jávea and hiking at amazing speeds; Pablo for deep conversations and the good laughs (I miss you). Also thanks to Rober and Salo for being like a family to me. To Carlos, for being so helpful, kind and a terrific flatmate. To Mario, for being such good company in this last year. I would also like to thank all from the Terminales for welcoming me in the group, the adventurous spirit you share and the sentiment of belonging that you gave me. In particular, to Davide and Javi at the beginning, encouraging me to regain my love for the rocks. And lately, to Alex and Ana for consistently being a pair of titans, providing unforgettable weekends. Thank you to Christian as well, the type of friend you do not make, you simply recognize.

Domi, a small paragraph is just not enough to show the appreciation I have for you. I am eternally grateful for being so lucky to have had you by my side, going through all that we

have been through during all these years. Thank you for the amazing friendship, support and your incomparable kindness.

Thank you to all the brazillian friends and my family. The time away only made me appreciate you even more. Alexandre and Koskies, in particular, for long skype conversations every three months at the most different time zones possible. And Sky as well, for the whatsapp audios and remarkable youtube comments shared with me. Mom, dad and Guto, thank you so very much for the emotional support and for the unconditional love you have been giving me since the day I was born. Lastly, thank you Mariana for everything. For understanding and for giving me support, with such love, in every decision I made. You are the rock upon which I stand.

Contents

List of Figures

LIST OF FIGURES

List of Tables

LIST OF TABLES

1

Introduction

Here we provide a short but complete set of the very basic concepts which are used throughout this thesis.

1.1 Surface Acoustic Wave (SAW)

Surface acoustic waves (SAWs) are modes of propagation of elastic energy along the surface of a solid whose displacement amplitudes exponentially decays away from this surface. When propagating in piezoelectric materials, an electric potential with the same spatial and temporal periodicity accompanies the surface wave. The existence of the basic type of SAW, in an isotropic material, was first demonstrated in 1885 by Lord Rayleigh [1], therefore the wave is often called a Rayleigh wave. This wave propagates along the plane surface of a half-space, with the particle motion in the sagittal plane (the plane containing the surface normal and the propagation direction). Rayleigh's studies was about seismic signals observed after a ground shock. Others followed Rayleigh's interest on seismic waves. On a treatise published in 1911[2], Love studied shear surface waves, whose

motion is perpendicular to the sagittal plane. This so-called Love wave, can exist when a half-space is covered with a layer of material with lower bulk shear wave velocity. Love also showed that a Rayleigh-type wave could exist in a layered system. Work on the layered Rayleigh wave at the Earthquake Research Institute, Tokyo, in the 1920s [3] showed that a series of higher modes could exist in addition to the fundamental, being the first of this higher modes, known as the Sezawa wave. Although arising from studies on earthquakes, Rayleigh, Love and Sezawa waves have and are all been used in modern SAW devices.

The interest in SAW for applications in electronics arose from radar improvement requirements in the late 1950s. The first suggestion for using planar SAW transducers was made independently by Rowen and Mortley in two patents in 1963 [4, 5]. Their motivation was to simplify the behavior and the fabrication of the traditional signal delay devices used for pulse compression (a requirement to improve the range capability of radars at that time). The first experimental realization of this planar structures was made by White and Voltmer in 1965 [6]. They demonstrated the uniform interdigital transducer (IDT), a device used for generating and receiving the waves on a piezoelectric substrate, in order to couple electric to elastic fields (see Fig. 1.1). To behave like a half-space, the substrate only needs to be a few wavelengths thick because the wave has a small penetration depth (see Fig. 1.2). With the invention of this component, the devices could be made easily and cheaply by lithographic techniques borrowed from semiconductor manufacture. In addition to the IDT, a range of other components were developed, particularly reflecting gratings, which are used for resonators (as you will see in our work). In the subsequent years, a very wide variety of devices have been developed, including delay lines, bandpass filters, oscillators and matched filters. The devices are found

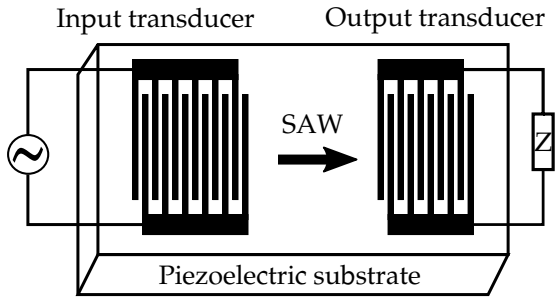

Figure 1.1: Schematic of a basic SAW device. An applied alternating voltage to the bus bars makes the piezoelectric substrate vibrate, generating the surface waves through the inverse piezoelectric effect. At the output port, the incoming waves generate a voltage difference, through the direct piezoelectric effect, which can then be measured.

in many practical systems, such as identity tags, professional radar pulse compression and expansion, RF and IF filters, TV and communications equipment and oscillators, as well as in consumer applications such as TV receivers and smartphones. More modern applications of SAW devices range from touch screens to a variety of sensors (for temperature, pressure, chemicals). Further information on the history of the SAW can be found on [7].

1.2 Material

Piezoelectricity can only be present if the material is anisotropic, that is, if its properties vary with direction in relation to the internal structure. Typical materials used are quartz (SiO_2), lithium niobate ($LiNbO_3$), lithium tantalate ($LiTaO_3$), PZT (lead zirconium titanate), zinc oxide (ZnO) and aluminum nitrate (AlN). Each of which present advantages and disadvantages depending on the application requirements. Also, due

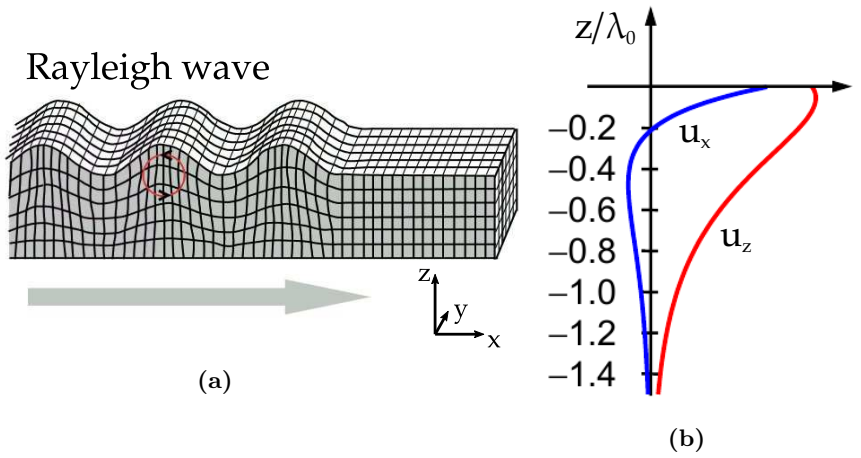

Figure 1.2: (a) Displacement during the propagation of a Rayleigh-type wave. The particles on the crystal undergo a ellipsoid movement on the sagittal plane, whose amplitude decays exponentially away from the surface. Therefore, a substrate of only a couple wavelengths is sufficient to act as a half-plane. (b) On the horizontal axis we represent the amplitude of displacement (arbitrary units) of the Rayleigh wave in the X (u_X) and the Z (u_Z) directions along the depth (z). Almost all the energy of the wave is confined to a $1.5\lambda_0$ layer of the substrate.

to the anisotropy, not only the choice of the material but the cut and direction of propagation of the wave along the crystal are of relevance. For example, the Y-Z cut of $LiNbO_3$* present a strong piezoelectric coupling, meaning that the conversion efficiency between electrical and acoustic energy is high. However, it also exhibit a high temperature instability, making it unsuitable for some practical applications. Another example: the ST-X cut of quartz present a weak piezoelectric coupling, however its properties are very temperature independent. Each material has its

*The notation indicates that the surface is normal to the crystal Y-axis and the wave propagates in the crystal Z-direction.

peculiarity and for this reason, a lot of investigation have been done on measuring materials properties and on discovering new and improved type of materials for different applications. The usual parameters taken into account are the SAW velocity (v_0), the temperature coefficient of delay (TCD), which quantifies the temperature stability, and the piezoelectric coupling coefficient (k^2), defined as the ratio of the mechanical energy accumulated in response to an electrical input. As a basic information we refer to the Table 1.1 which contains the information found on [7]. For our purposes we chose the Y-cut of the 128°-rotated $LiNbO_3$[†] due to its strong coupling and low conversion to bulk waves. More on why this is our preferred material will be made clear throughout our analysis.

Table 1.1: Comparison of parameters of commonly used materials. TCD stands for the temperature coefficient of delay.

Material	v_0 **(m/s)**	k^2	**TCD** (ppm/°C)	**Comments**
Lithium niobate, Y-Z	3488	4.8%	94	Strong coupling, large TCD minimal diffraction, bad bulk waves
Lithium niobate, 128°Y-X	3992	5.3%	75	Strong coupling, large TCD Free of bulk waves
Quartz, ST-X	3159	0.12%	0	Weak coupling, low TCD
Lithium tantalate, X-112°Y	3300	0.7%	18	Intermediate coupling and TCD Free of bulk waves
PZT ceramic, Z-X	2360	2%	40	Too lossy above 50 MHz Poor repeatability
ZnO/glass	2576	1.4%	11	Fabrication complex Not very repeatable

[†]This is a rotated Y-cut. The surface normal makes an angle of 128° with the crystal Y-axis, and the wave propagates in the crystal X-direction.

1.3 Fabrication

Typical SAW devices are fabricated through basic lithography. This is a process used to form patterns in a layer of an energy-definable polymer (resist) that can be transferred, by selective etching, into an underlying substrate [‡]. This is the technique that patterns and guides the fabrication of semiconductor components devices and circuitry. To build the complex structures that make up a transistor and the many wires that connect the millions of transistors of a circuit, lithography and etch pattern transfer steps are repeated at least 10 times, but more typically 25 to 40 times to make one circuit. Due to the large number of lithography steps needed in integrated circuit (IC) manufacturing, lithography typically accounts for about 30% of the cost of manufacturing a chip [8]. Moreover, lithography has been, historically, the bottleneck of advances in IC cost and performance, being the technical limiter for further advances in transistor size reduction and, thus, chip performance. The most advanced mass-produced large-scale integrated circuits have a critical dimension of around 180 nm. However, the most common limit in the standard research laboratory is about 500 nm. For a typical velocity of 3000 m/s this gives a maximum operating frequency of 1.5 GHz, though special techniques can extend this to 5 GHz. This can be done, for example, by growing a thin layer of a piezoelectric material on top of a hard elastic solid in which the waves propagate faster. This way the waves can be generated by standard IDTs but with a higher frequency than compared with that of the piezoelectric material alone.

[‡]A detailed explanation of this process is given in the next chapter.

1.4 Interdigital transducer (IDT)

An IDT consists of an interlocking comb-shaped metallic pattern. Applied to a piezoelectric substrate, they are the most convenient way for converting microwave voltages to surface acoustic waves, and vice versa. On the input port of a basic two-transducer surface-wave device (Fig. 1.1) the waves are strongly generated for frequencies such that the wavelength is similar to twice the transducer pitch, p. However, this configuration has a drawback, namely the reflection of the waves by the transducers. This usually unwanted reflections reach the output after three transits of the device, in what is called 'triple transit' signal (see Fig. 1.3a). Each electrode reflects only weakly, but the reflections become significant if they are added in phase. In a 'single-electrode' transducer the center-frequency wavelength is $\lambda_0 = 2\mathrm{p}$ and the reflections add in phase at its central frequency of operation. A well known method for avoid this problem is to use a double-electrode transducer, or 'split-finger transducer', where the electrodes are connected to the two bus bars in pairs so that the electrode pitch p is now $\lambda_0/4$ (see Fig. 1.3b). Therefore, they are non-reflective and for this reason are often preferred over the single-electrode configuration. There is a trade-off, however, because the reduction of the electrode pitch in half can be limited by the fabrication resolution, being unsuitable for high frequency applications.

It is also important to note that the more fingers used, more the signal will be sharply concentrated around the central frequency which it was designed for. In Fig. 1.4 one can see the difference in the transmission shape for different number of fingers in the IDTs (this was calculated with a simulation model developed by us which we will introduce further on this thesis). The fundamental frequency, f_0, is given by $\mathrm{f}_0 = v_0/\lambda_0$.

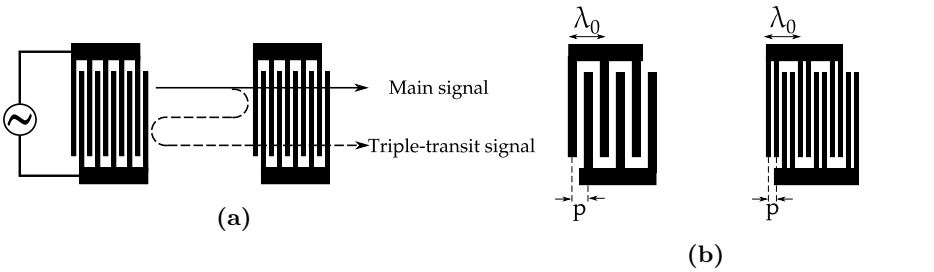

Figure 1.3: (a) Origin of triple-transit signals on single-electrode IDTs. (b) Comparison of the single and double-electrode design of IDTs. The pitch, p, is reduced from $\lambda_0/2$ to $\lambda_0/4$ which makes the structure non-reflective, thus avoiding the unwanted signals.

The message here is that the number of finger pairs is a very important parameter for designing these devices, besides the pitch which determines the central frequency of operation.

1.5 Bragg reflector (BR)

Taking advantage of the above discussion about the reflective IDTs we introduce a commonly used SAW device, the Bragg reflector (BR). These are interferometric mirror structures which consists of an alternating sequence of perturbations in the path where the waves travel. The most frequently used design is that of a quarter-wave mirror, where the thickness of the perturbation corresponds to one quarter of the wavelength of the wave for which the mirror is designed, considering normal incidence. In optics, this is done by alternating two materials with different refractive index. For SAWs this is usually accomplished by depositing metals strips of $\lambda_0/4$ width on the surface of the substrate, by exactly the same process of fabricating IDTs. Each strip reflects only a small part of the incoming

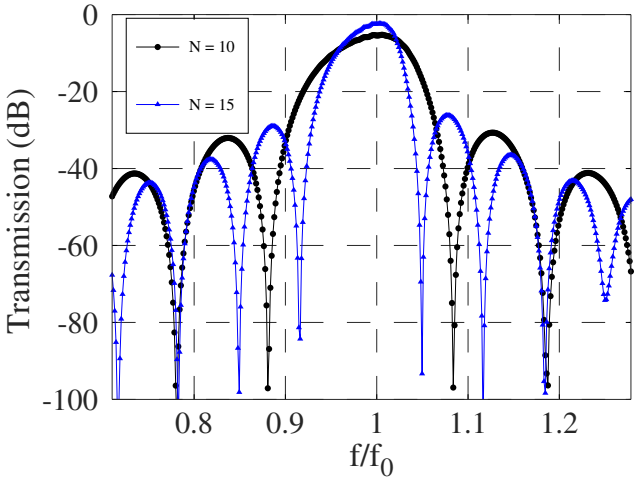

Figure 1.4: Two simulation results for the transmission between IDTs in a delay line on lithium niobate where the number of IDTs' fingers pairs (N) was changed from 10 to 15. The bandwidth of the transmission between IDTs in the vicinity of the fundamental frequency is inversely proportional to N. This was calculated using a simulation model developed by us which will be introduced later on.

wave. However, using $\lambda_0/4$ wide fingers and spacing them by the same amount, results in the constructive interference of the reflected waves, thus creating efficient mirrors. This is why they are also called *distributed Bragg reflectors*. Effectively, this creates a stop band in the transmission spectrum of the incoming wave, whose shape and magnitude depend on several factors, such as the number and height of the strips and the material used. The two basic mechanisms controlling how much of the wave is reflected by a strip are the *mass-loading* and the *piezoelectric screening*. Both cause a relevant change in the properties of the substrate underneath. The first, by the weight, which depends on the height and on the density of

the material. The last, by screening the electric potential on the surface of the area it covers, due to the high conductivity of metals. The conjunction of these effects forms the *reflectivity* of the strip, r, which can be divided in the two contributions, so that $r = r_M \pm r_E$. r_M is related to the mass loading and r_E, to the piezoelectric screening. The sign of r_E depends on the electrical condition of the strips of the mirror. If the strips are sitting next to each other, in what is called the floating configuration (see differences between BRs in Fig. 1.5a and Fig. 1.5b), the positive sign is used. If the ends of the strips are connected by an additional metal strip, short circuiting all strips together (shorted configuration), then the negative sign is to be used. As the r_M is usually negative, a shorted configuration is preferred for higher reflection. However, for some materials, r_M can be positive, so that for a specific combination the reflectivity can even be zero. The total reflection, R, of a BR at its resonance frequency is given by $R = \tanh(\mathrm{M}|r|)$, being M the number of strips in the BR. This is a result derived in [9], where the Reflective Array Method (RAM) was used. This is one of the theoretical approaches for studying SAW devices which considers the scattering by individual strips. The same reference gives us the stop band derived from the mirror to be $\Delta \mathrm{f}_{SB} = (2\mathrm{f}_0/\pi)\sin^{-1}|r|$. On the next chapter we will comment on RAM as well as on some of the most known theoretical methods.

1.6 Cavities

A cavity (or a resonator) is a device designed to confine the energy of the waves. The final purpose is very diverse, but usually they are used to generate waves of specific frequencies or to select specific frequencies from a signal. The most common cavity used in optics is the Fabry–Pérot

cavity, made from two parallel mirrors. The acoustic version is the usual SAW resonator, made from two BRs (see Fig. 1.5 for two example designs). For the design in Fig. 1.5b one usually measures the transmission between input and output IDTs. A single mirror in the path of the wave will create a stop band in the transmission spectrum. A cavity is formed by properly spacing the BRs by an integer multiple of $\lambda/2$, allowing the waves in between to interfere constructively, which in turn creates a transmission peak inside of the stop band. For the design in Fig. 1.5a, the measurement is a little different. The IDT provides both input and output port and the resonator is probed by measuring the reflection of the IDT. These resonators can exhibit one or more resonant modes. If the mode spacing of the cavity (also called *free spectral range, FSR*), which is the frequency spacing of its resonance modes, is bigger than the stop band of its mirrors, then the resonator supports only one resonant mode. On the contrary, if FSR $< \Delta f_{SB}$, then more modes are observed. This occurs for longer resonators, given that FSR$= v/L_c$, being L_c the length of the cavity. Note that, however, L_c is not equal to the nominal distance between the first strip of each mirror, d. As the reflectivity of each strip usually is small, the resonant mode partly penetrate into the mirrors an effective penetration depth of $L_p = a/|r|$, a being the width of the strip, so that $L_c = d + 2L_p$. See [10] for a discussion on resonator properties.

The efficiency of a cavity is measured by the figure of merit called the quality factor, Q, defined as

$$Q = \frac{2\pi f_0(stored\ energy)}{(power\ loss\ per\ cycle)} \ . \tag{1.1}$$

As there are several loss mechanisms, this parameter can be further split into two, one part related to external circuitry coupled to the cavity (Q_e) and one part concerning intrinsic losses (Q_i) such as the finite grating

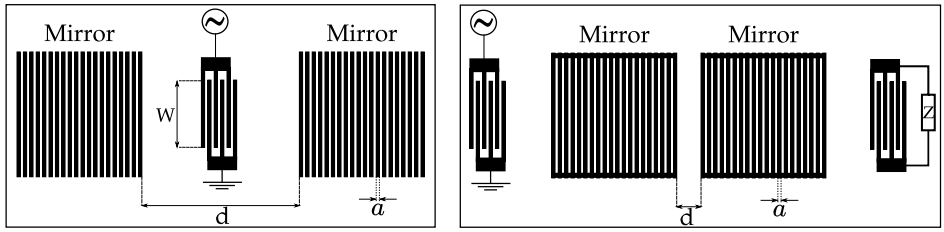

Figure 1.5: (a) One port SAW resonator consisting of two BRs (floating configuration) separated by a distance d. The width of the strips normally is $a = \lambda_0/4$. W is the aperture of the IDT. (b) Two port, one cavity SAW device. The BRs here use a shorted configuration.

reflectivity, diffraction losses, conversion of surface acoustic waves into bulk modes, material losses and resistivity of the electrodes. The total Q, also called 'loaded Q', is then defined as $1/Q = 1/Q_i + 1/Q_e$. In practice, this Q-factor is extracted directly from a Lorentzian or Gaussian fit of the resonant peak, calculated as $Q = \omega/FWHM$, where $\omega = 2\pi f$ and FHWM is the full width at half maximum of the peak.

1.7 Previous work – Coupled cavities

Now that we have introduced most of the basic elements and concepts used in our work we are in position to present the most interesting results achieved before the beginning of the original investigation exposed here. In this section we expose the foundation on which this thesis was built upon.

We have already mentioned that a cavity consists of two BRs separated by a conveniently chosen distance. The signature of this configuration is a peak inside of the stop band of the transmission spectrum. But, what

happens when another BR is placed next to it, forming another identical cavity? A naive prediction would say that the observed peak would be the same (except maybe more pronounced) given that the spacing is the same and, therefore, the range of frequencies that are allowed to resonate would remain the same. However, this is not the case. Actually, due to the finite reflectivity of the BRs, the resonant acoustic energy is not confined only to the area of the cavity, but it is spread along the device. Being the second cavity located close enough to be in the area of influence of the first, the cavities will "see", i. e. be affected by, each other. Thus, they will not be isolated but *coupled* together. For didactic purposes, an analogy can be made with the formation of molecular orbitals. If, for example, two hydrogen atoms are initially isolated, they have identical atomic orbitals. However, as they are brought together, the electron wave functions begin to overlap. Each original atomic orbital of the isolated atoms splits into two molecular orbitals belonging to the pair, one lower and one higher in energy than the original atomic level, in what is called bonding and anti-bonding orbitals. In the case of dealing with SAW cavities at room temperature, although no quantum mechanical effect is in place, the same energy splitting occurs. This was experimentally achieved in [11], where it was reported the fabrication and measurement of devices composed from two to up to five coupled cavities. In Fig. 1.6 we see a micrograph of one of this devices, composed of five cavities. The SAW cavities are formed within the spacing between the distributed Bragg reflectors (BRs), each of which is composed of 20 gold strips deposited on a 128°-rotated Y-cut $LiNbO_3$ delay line. Three pairs of split-finger aluminum IDTs were designed for an acoustic wavelength of $\lambda_{SAW} = 11.2\ \mu$m, which corresponds to a center resonance frequency of approximately 340 MHz for a Rayleigh wave propagating in the X-direction. The coupled cavities were fabricated

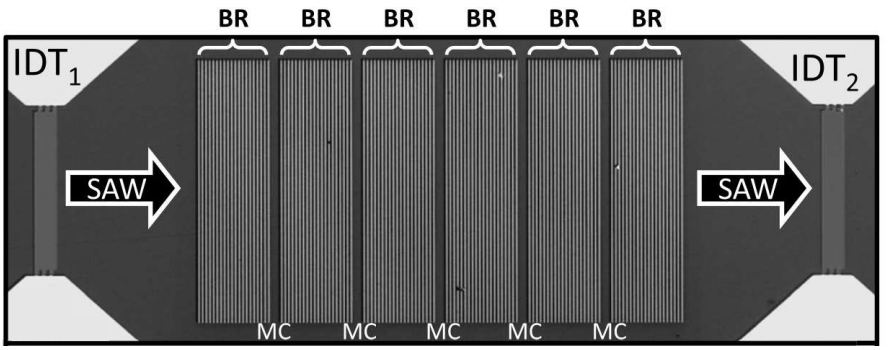

Figure 1.6: Micrograph of a sample with five coupled microcavities (MC). The split-fingers IDTs are composed of 3 pairs of aluminium fingers; each Bragg reflector (BR) have 20 gold strips $\lambda_{SAW}/4$ wide, separated from each other also by $\lambda_{SAW}/4$. The cavities are $3\lambda_{SAW}/2$ wide. Figure extracted from [11].

by depositing NiCr/Au gratings with thicknesses h = 10/110 nm within the SAW delay lines. Gold was used to favor the mass loading and the NiCr layer is for better adhesion to the substrate. The response of each device is seen in Fig. 1.7 and compared with a simulation model based on the transfer matrix method. Besides the coupling of a different number of cavities, the authors show the differences in using a shorted or floating configuration for the mirrors. The main result is that the frequency of the resonances decreases by approximately 1.6% from the floating to the shorted case. So the central message is that these results demonstrate the possibility of an electrical tuning of the acoustic response of the coupled cavities. That is, the response of the devices can, in principle, be electrically controlled by varying the impedance between the strips.

Furthermore, the authors also access the acoustic field along the structures via interferometry, an experiment that we will explain in detail on the next chapter. The signal measured $\langle u_z'^2 \rangle$ is not exactly but proportional

to the time-averaged squared amplitude of the vertical particle displacement. The results are for the excitation frequencies corresponding to the 5 maxima of the Fabry-Pérot oscillations in the transmission experiments of Fig. 1.7(a). The evolution of the field distribution demonstrates the

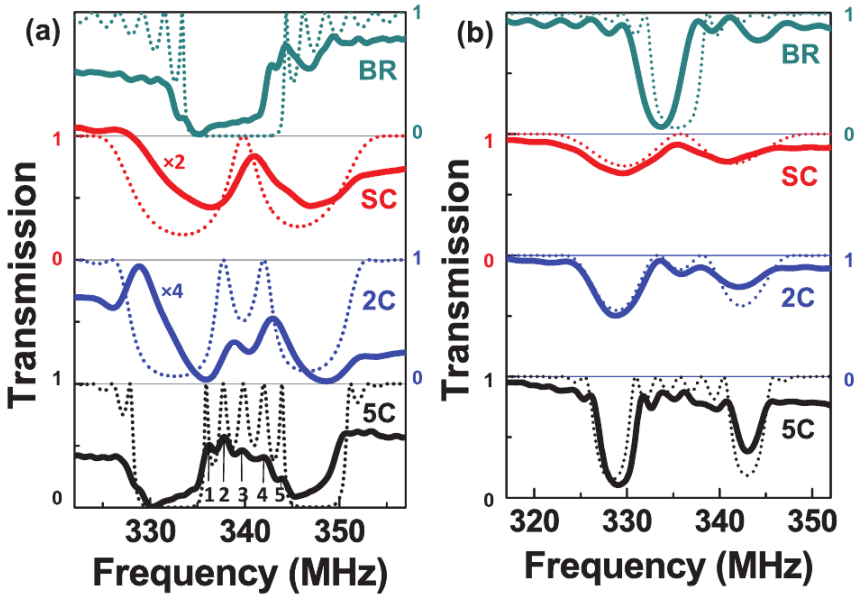

Figure 1.7: Experimental (solid lines) and calculated (dotted lines) transmission spectra for a set of grating structures with (a) floating and (b) short-circuited strips. From top to bottom, they correspond to a 120-strips BR, a single cavity (SC), two coupled cavities (2C), and five coupled cavities (5C). The BRs of the structures with cavities are 20-strip. The numbers from 1 to 5 indicate the order of the Fabry-Pérot modes. Figure extracted from [11].

positive dispersion of the transmission mini-band investigated. In other words, the eigenfunction of the lowest eigenfrequency corresponds to a mode with the smallest wavevector, as it is sketched in Fig. 1.8(c) for the envelop of u_z. This sketch give us a good insight on the acoustic

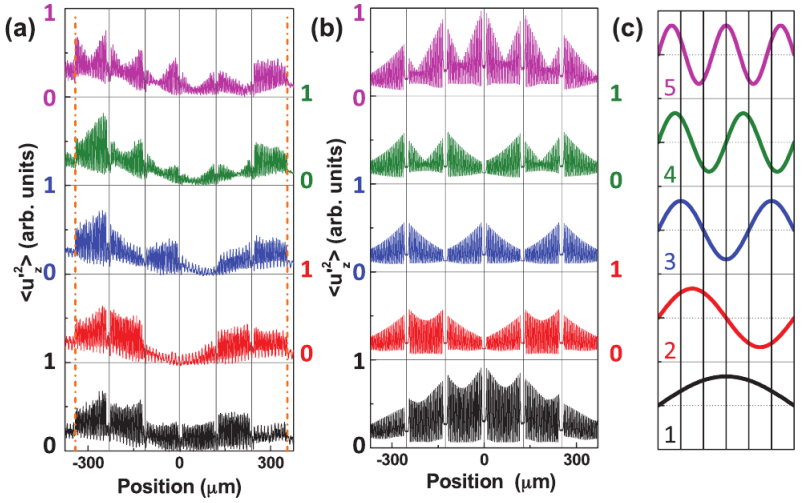

Figure 1.8: (a) Measured and (b) calculated $\langle u_z'^2 \rangle$ profiles for five coupled MCs (5C) with floating strips for the excitation frequencies 1 to 5 (from bottom to top) indicated in the lowest panel of Fig. 1.7. The vertical dash-dotted lines indicate the edges of the structure while the vertical solid lines mark the position of the MCs spacers. (c) Schematic diagram illustrating the expected field envelops for minibands with positive dispersion. Figure extracted from [11].

field distribution connected to each of the resonant modes. Focus on the frequencies excitation "1" and "2", for example. The cavities located at approximately -240 μm and 240 μm vibrate nearly by the same amount (same amplitude of vertical displacement). However, while both cavities vibrate in phase in the case "1", they actually vibrate out of phase for mode "2". That is the type of control which the coupled cavities allow. A change in the relation of acoustic fields in different areas of the same device by simple variation of the frequency excitation.

2

Methods

Here we introduce the invaluable simulation models developed by us and compare it with some other available methods for investigating SAW. Also, we explain in detail the design and fabrication of our devices. And finally, we explicit the setup of the experiments performed.

2.1 Finite element method (FEM)

A great deal of physical phenomena can be described in terms of partial differential equations (PDEs). It is difficult to overstate this, since the wave equation, the heat equation, Laplace's equation, Poisson's equation, Schrödinger's equation, transport equation, Maxwell's equations and the Burger's equation (to name a few!) compose a set of examples of PDEs in Physics. However, for the majority of geometries and practical situations, these PDEs cannot be solved analytically. Instead, an approximation of the equations can be constructed, based upon different types of discretizations. These discretization methods approximate the PDEs with numerical model equations, which can be solved using numerical methods. The finite element

method (FEM) is one of the most prominent numerical techniques used to perform such approximations.

Historically, FEM is said to have its origins in the *Introduction to the Analysis of the Infinite*(1748), by Leonhard Euler [12], which lays the foundations of mathematical analysis. However, the earliest mathematical papers on FEM can be found in the works of Schellbach [13], in 1851, and Courant [14], in 1943. The modern developments began in the mid-1950s, being independently developed by engineers to address problems related to aerospace and civil engineering in stress analysis, fluid flow, heat transfer, and other areas. The first book on the FEM by Zienkiewiczand Chung [15] was published in 1967.

Following the discussion in [16] we are going to use a simple 1D problem to go through the various steps involved in finite element analysis (FEA) as a way to introduce its more basic elements. Consider the equation and boundary conditions shown below

$$-(p(x)u'(x))' + q(x)u(x) = f(x),\ x\ \in (0,1),$$
$$u(0) = 0,\ u(1) = 0\ .$$

The equation is multiplied by a trial function $v(x)$ on both sides and integrated in the domain $[0,1]$

$$\int_0^1 -(p(x)u'(x))'v(x)\mathrm{d}x + \int_0^1 q(x)u(x)v(x)\ \mathrm{d}x = \int_0^1 f(x)v(x)\ \mathrm{d}x\ .$$

In the first term of the left-hand side we use integration by parts and apply the boundary conditions, so that we have

$$\int_0^1 p(x)u'(x)v'(x)\mathrm{d}x + \int_0^1 q(x)u(x)v(x)\ \mathrm{d}x = \int_0^1 f(x)v(x)\ \mathrm{d}x\ .$$

We have changed from the differential form of the equation, known as the strong form, to the integral form, known as the weak form. As a result,

the order of continuity required for the unknown function $u(x)$ is reduced by one. This is also true for multi-dimensional functions, replacing the derivatives by gradients and divergence. Avoiding going into much detail, we note that the Riesz representation theorem can prove that there is a unique solution for $u(x)$ for the integral, and hence the differential form. Moreover, if $f(x)$ is smooth, it also ensures that $u(x)$ is smooth.

The next step is discretization. As we want to solve it by numerical methods, the integral must be converted into a summation. The domain must then be divided into N subintervals $[x_i, x_{i+1}]$, $i = 0, ..., (N-1)$, known as *elements* and the points on the corner of each element, x_i, are known as *nodes*. Interpolation functions are defined for each element to interpolate, for values inside the element, using nodal values. These interpolation functions are also often referred to as shape, ansatz or basis functions. In the $(N-1)$-dimensional subspace of the original space we must find u_h such that

$$\int_0^1 p(x)u_h'(x)v_h'(x)\mathrm{d}x + \int_0^1 q(x)u_h(x)v_h(x)\mathrm{d}x = \int_0^1 f(x)v_h(x)\mathrm{d}x \ .$$

The unknown function $u(x)$ can be approximated by a function u_h using linear combinations of basis functions, which will be calculated at the nodal points

$$u_h(x) = \sum_{i=1}^{N-1} U_i\psi_i(x)$$

where $\psi_i(x)$ and U_i are the interpolation (or basis) functions and its coefficients associated with node i, respectively. One of the benefits of using the finite element method is that it offers great freedom in the selection of discretization, both in the elements that may be used to discretize space and the basis functions. Similarly, interpolation can be

used for $v(x)$ present in the weak form, so that it can be rewritten as

$$\sum_{i=1}^{N-1} U_i \int_0^1 [p(x)\psi_i'(x)\psi_j'(x) + q(x)\psi_i(x)\psi_j(x)]\mathrm{d}x = \int_0^1 f(x)\psi_j(x)\mathrm{d}x \ ,$$

for $j = 1, ..., (N-1)$.

Letting

$$a_{ji} := \int_0^1 [p(x)\psi_i'(x)\psi_j'(x) + q(x)\psi_i(x)\psi_j(x)]\mathrm{d}x \ , \text{ and}$$
$$F_j := \int_0^1 f(x)\psi_j(x)\mathrm{d}x \ ,$$

the summation schemes can be transformed into matrix products and then the weak form can be written as a matrix form

$$AU = F$$

where $A = (a_{ji})$ and $F = (F_1, ..., F_{N-1})^T$. A is a $(N-1)$x$(N-1)$ matrix containing the coefficients of U_i in each equation j within its components a_{ji}, known as the stiffness matrix for historical reasons. U is the vector of nodal unknowns, $U = (U_1, ..., U_i, ..., U_{N-1})$. The solution of the system of algebraic equations gives an approximation of the solution to the PDE. The denser the discretization is, the closer the approximate solution gets to the actual solution. In effect, the finite element method is a systematic way to convert the functions in an infinite dimensional function space to functions in a finite dimensional function space and then finally ordinary vectors (in a vector space) that are tractable with numerical methods.

Once the matrix equations have been established, the equations are passed on to a solver to solve the system of equations. Depending on the type of problem, a direct or an iterative solver can be used. Commonly adopted approaches to directly calculate the solution include Gaussian

elimination, LU (lower-upper), Cholesky and QR decompositions. However, such direct methods fail when the matrices are very large, for example, in the order of a few million. If the matrix is of order n, then n x n x n operations are needed to solve the system using Gaussian elimination. So if the system has 10 million unknowns it would need operations of the order of exaFLOPS (10^{18} floating point operations per second). In this case, an iterative solver is more suitable. The iterative solver starts by assuming an approximate solution for the unknowns U and the solution is iterated in order to reach an "exact" solution.

2.2 FEM compared to other methods

Several phenomenological methods have been proposed for modeling and analysis of acoustic waves. These include the coupling-of-modes (COM) model, P-matrix model, equivalent circuit models, and angular spectrum of waves model. The comparison of these models [17] shows that, if used correctly and with accurate parameters, almost identical results are obtained with all of them. For the case of a classic Rayleigh-type SAW on quartz substrate, with weak interactions and narrow frequency band, all models give excellent results. On the other hand, all models provide only satisfactory descriptions of devices employing surface transverse waves (STWs) and leaky surface-acoustic waves (LSAW).

As they are phenomenological, their function depends crucially on certain explicit parameters, which must be known to high accuracy. The parameters may be achieved in various ways: directly, for example, by laser probe techniques, indirectly by plotting one of the cited models to electric measurements from devices or test structures, or theoretically from analytic perturbation theories or more rigorous numerical simulations. Among these,

the electric measurements from specially designed test structures are said to be the most reliable method. And it is precisely the electric response which is usually of the main interest in SAW devices. Unfortunately, experimental parameter extraction are both expensive and time-consuming, since the parameters have to be individually determined for each substrate with every material, size, shape, and structure of the electrodes. Moreover, uncertainties in the properties and the geometry of the electrodes due to the manufacturing technology limit the accuracy of the results obtained. For this reason, numerical methods based on the finite-element method or rigorous Green's function techniques have recently been developed and used with this purpose. As Plessky [18] puts it, relating to COM model: "As a general simplified description of waves of different physical nature in periodic media the model will be used always, but for exact design the tendency will be to use the numerical FEM/BEM methods, at least for the determination of the COM parameters."

There are some disadvantages on using the FEM [19]. For example, the solution never is in a closed-form, not permitting the examination of a system response to a change in a certain parameter. Moreover, inherent errors exist: the true geometry is simplified; the field quantity is always assumed to be a polynomial over an element; and the use of very simple integration techniques, such as Gauss quadrature. And finally, there are inherent computational errors such as the finite number of digits ($\pi = 3.14159265$, for example). Nonetheless, the advantages are huge: it can handle very complex geometry, boundary conditions and loading (time or frequency dependent) in a wide variety of physics problems.

When dealing with FEM, usually a lot of mathematics is involved in the decision of choosing interpolation functions, which requires knowledge of functional spaces (such as Hilbert and Sobolev), and also a lot of tests

have to be done to decide the type of solver and numerical approach to use. Fortunately, nowadays, a vast number of commercial software are available that provides the user with instructions on the best models for each physics related problem one wants to solve. In our case, we use COMSOL Mutiphysics software platform [20] with its built 3D CAD engine, as well as its integrated solver. As we will see next, some very low-time consuming simulations can be useful to give invaluable insight on the possible design of devices. In addition, we find that the 2- and 3-D simulations, in spite of time-consuming, give accurate results for very different situations. The simulations were run on a desktop personal computer with Linux (Ubuntu) 3.40 GHz 64-bit processor and 16 GB RAM.

2.3 Simulations models

In this section we provide the details of the simulation models built with COMSOL Multiphysics software platform [20], starting from the most simple 2-dimensional eingenfrequency study until the 3D model that simulates the whole device. Before we go any further, a few general remarks and some caveats are in order.

Physics modules: after choosing the geometry to work with, 2- or 3-dimensional, COMSOL Multiphysics [20] allows you to choose from a variety of predefined modules, each tailored for specific physical problems. We chose "Piezoelectric Devices" in the model wizard, which automatically adds two modules by default, the "Solid Mechanics" and the "Electrostatics". The coupling between both is implemented using the well-known coupled constitutive law for piezoelectric materials. At first glance, the use of Electrostatics might seen strange. However, the term "statics" is not to be interpreted literally. It is the observation time, or time scale at which the

applied excitation changes, that is short compared to the charge relaxation time. Generically, the relaxation time of the material is defined as $\tau = \epsilon/\sigma$, being ϵ the dielectric constant and σ the electrical conductivity. For a good conductor τ is about 10^{-19} s, for a good insulator, 10^3 s. Considering the typical excitation we apply, of around 300 MHz, this corresponds to a time scale $T \approx 3$ ns. It is clear that for the typical substrate $\tau >> T$ and electrostatics can be safely applied. On the metal strips, the workaround is to define suitable electrical boundary conditions.

Material parameters: COMSOL Multiphysics [20] provides an extended library with the physical properties of the most commonly used materials. Moreover, when dealing with a 3D geometry, there is a built-in engine that performs rotations so that one can easily choose the preferred cut and direction one wants to work by simply providing the software with the appropriated Euler angles - which can be consulted in a table, in [9] for example. However, for 2D models one have to perform the rotation by oneself. The way to do it is to perform a Bond rotation [21] of the matrices containing the relevant parameters which depend on the cut and direction, such as the elastic, coupling and dielectric constants.

Mesh: as we have mentioned earlier, the idea behind FEM is to use a simple discretization method where the errors become unnoticeable as the size of the subregions gets smaller. The idea is very simple: take a geometric shape, break it into smaller, simpler shapes, in such a way that we can put it all back together when calculations are done. This is done when generating the mesh. However, this can be quite troublesome if one realizes the kinds of conditions the mesh must meet, such as smoothly change in size near the boundaries where the solution is expected to change a lot or be placed around regions including holes and edges, or even adapt to curvatures (in the 3D case). Fortunately, our geometries are quite

simple and we mostly use a "Free Triangular" definition for almost all domains. This method uses a *Delaunay triangulation*, which maximize the minimum angle of all the angles of the triangles in the triangulation. It is a tessellation named after Boris Delaunay for his work done on this topic in 1934 [22]. Each small subregion is an *element*. The unknown field variable is expressed in terms of the assumed approximating functions within each element. These interpolation (or basis) functions are defined in terms of the values of the field variables at specific points, referred to as *nodes*. Nodes are usually located along the element boundaries, and they connect adjacent elements. These elements are connected to each other by their shared nodes. A node specifies the coordinate location in space where degrees of freedom and actions of the physical problem exist. The nodal unknowns in the matrix system of equations represents the primary field variables. Nodal variables assigned to an element are called the degrees of freedom (DOF) of the element. The common nodes provide continuity for the nodal variables. The DOF of a node are dictated by the physical nature of the problem and the element type. As we deal with both structural mechanics and with electrostatics, the DOF are the displacement field and electric potential.

Concerning the resolution, the finer the better. But, as the finer mesh demands more computational power, some testing is required to adequate the mesh according to the computational resources. Best practices recommendation is to have elements with $\lambda/20$ (minimum size) in the most important parts of the domain, and have it coarse as the borders approach. In Fig. 2.1c we exhibit an example of a mesh tailored to have higher element density closer to the surface, where the energy of the Rayleigh waves are concentrated.

Perfectly matched layer (PML): when dealing with simulations, the space has been truncated to some computational region. Some problems involve solutions that are rapidly decaying in space, so that the truncation is irrelevant as long as the computational grid is large enough. However, this is not generally true. Some wave equations require an absorbing boundary that will somehow absorb waves that strike it, without reflecting them, and without requiring infeasible resolution. The first attempts involved absorbing boundary conditions. In 1994, however, the problem of absorbing boundaries for wave equations was transformed in a seminal paper by Berenger [23]. Instead of finding an absorbing boundary condition, he found an absorbing boundary layer. A layer of artificial absorbing material that is placed adjacent to the edges of the grid, completely independent of the boundary condition. He showed that special absorbing medium could be constructed so that waves do not reflect at the interface: a perfectly matched layer, or PML. Although PML was originally derived for electromagnetism (Maxwell's equations), the same ideas are immediately applicable to other wave equations [24].

For a detailed explanation on this subject and the basic parameters' definitions we refer the reader to Comsol's documentation: COMSOL Multiphysics Reference Manual>Global and Local Definitions>Infinite Elements, Perfectly Matching Layers and Absorbing Layers>Perfectly Matching Layers. However, we stress the fact that there is no general way to define a good PML. It should be tailored according to the specific problem. Also, the mesh plays an important role on the attenuation of the incoming waves on the PML. When it comes on PML meshing, more resolution is not synonym of better results. Sometimes increasing the number of mesh elements or defining a PML with high curvature scaling parameter or scaling factor can increase the reflection of the incoming

waves. For the domains set as PML is advised to use the a "Swept" or "Mapped" mesh for better control. Also, a minimum of 5 mesh elements from the inner to the outer border is desired.

2.3.1 2D models

One of the most quick and simple simulations one can do in order to gain some insight on the behavior of the chosen material and crystal cut is an eigenfrequency study in two dimensions. Consider the Fig. 2.1. The model is repeated three times focusing on different aspects. The width of the model is exactly λ_0 and a periodic boundary condition is applied on left and right sides which are highlighted in Fig. 2.1b. This forces all relevant physical quantities to be the same at these boundaries, allowing for the acoustic modes that comply that condition to be calculated. This simulates an infinite substrate on which waves of wavelength λ_0 are traveling.

In Fig. 2.1a we fix the geometric parameters: h and l are the height and width of the strips, respectively. D is the depth of the substrate and D_{PML} is the depth of the perfectly matched layer (PML).

The second model we would like to introduce is a 2D cut of the saggital plane of one of the typical structures we presented in the Introduction, as can be seen in Fig. 2.2. This is used in a frequency domain study to calculate the transmission through different combinations of strips and cavities. For a 2-port type of device where there are a generating and a receiver ports, we set half of the generating IDTs as "Ground" and for the other half, "Terminal" with the "Terminal type" option set as "Voltage". And for the receiving IDTs, half as "Floating Potential 1" and half as "Floating Potential 2". We then take the difference between the extracted voltages of these floating electrodes at the receiver and divide by the applied

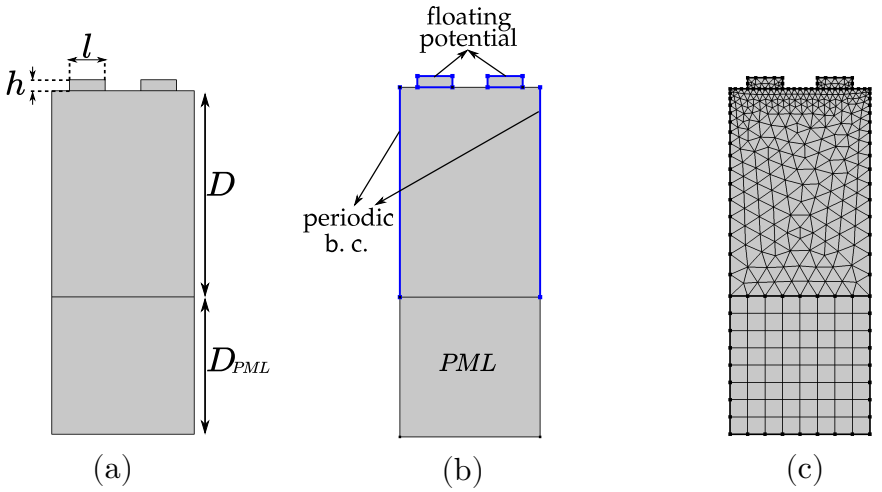

Figure 2.1: Simple 2D model of λ_0 width used to find eigenfrequencies. (a) Geometric parameters: h and l are the height and width of the strips, respectively. D is the depth of the substrate and D_{PML} is the depth of the perfectly matched layer. (b) Periodic boundary conditions are applied on both sides of the model, forcing the relevant physical values to be the same at it. At the strips a floating potential is applied, forcing them all to have the same potential for the shorted simulations, or having only adjacent boundaries sharing the same potential for simulating the floating case. (c) Example of a mesh tailored to have higher element density closer to the surface, where the energy of the Rayleigh waves are concentrated.

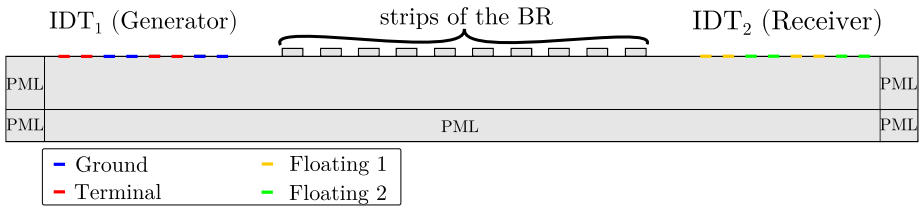

Figure 2.2: Example of a 2-port device composed of split-finger IDTs defined by line segments and one Bragg mirror (with 10 strips) build with an array of rectangles.

voltage at the generator. According to COMSOL's AC/DC Module User's Guide [25] (section "Lumped Ports with Voltage Input") this is the direct approach to calculate the transmission through the structure.

A similar model was created to simulate an one-port device. In Fig. 2.3 we can see a model with three pairs of single-finger IDT and two BRs of 10 strips each. Here, we apply the same electrical boundary conditions as in the generating IDT of the preceding model, however the figure of importance is the reflection.

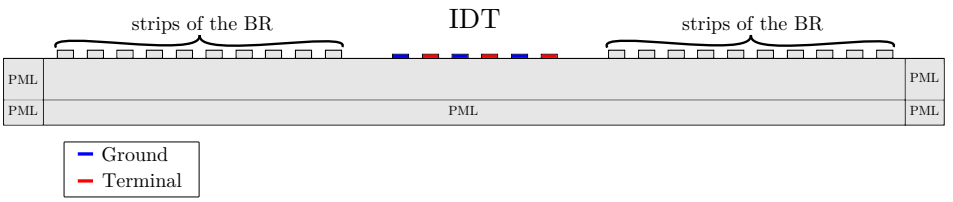

Figure 2.3: Example of a 1-port device composed of three pairs of single-finger IDTs defined by rectangles and two Bragg mirrors (with 10 strips each) build with an array of rectangles.

2.3.2 3D models

In Fig. 2.4 we introduce a model equivalent to the one in Fig. 2.1. The conditions which were applied to boundaries lines there, here are applied to surfaces. Moreover, as the wave velocity changes according to the propagation direction, the size of the model is not the same in the perpendicular direction. That is, from a top view, the model is not a square but a rectangle. Therefore, the perturbation on top has also to comply to that. Instead of using circular or square pillars, one has to use an ellipse or a rectangle if the stop bands in both perpendicular directions are to be matched in frequency. In the Results chapter, this will become clear as we use this model to calculate the band structure of the crystal

under investigation.

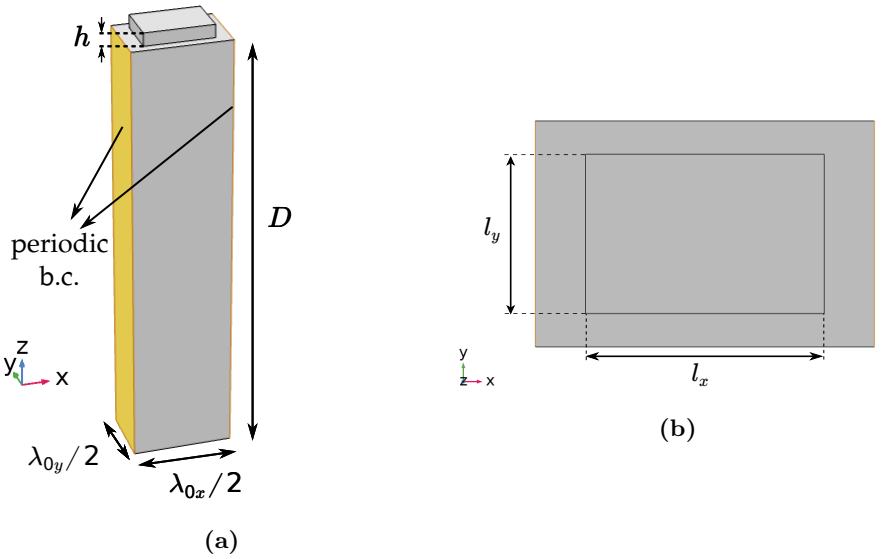

Figure 2.4: 3D model used to find eigenfrequencies. We use λ_{0X} and λ_{0Y} as the size in the X and Y directions in order to simulate an unit cell. (a) Geometric parameters: h is the height of the pillar and D is the depth of the substrate. Periodic boundary conditions are applied on the opposite sides of the model on both directions, forcing the relevant physical values to be the same at it. At the pillars a floating potential is applied, forcing the potential to be the same at the area underneath. (b) Top view of the model. l_X and l_Y are the size of the rectangular pillar in the X and Y directions, respectively.

A 3D equivalent of the model in Fig. 2.2 is also build (see Fig. 2.5). However, we apply periodic boundary conditions to the front and back of the model (xz-plane). This way, we simulate the desired number of pillars and cavities in one direction but simulate an infinite grid on the perpendicular direction. This allow us to do a 3D investigation without increasing the computational demand too much. For this reason we refer to this model as 'pseudo 3D'.

A 'real 3D' model was built as well. The interest in realizing this relies

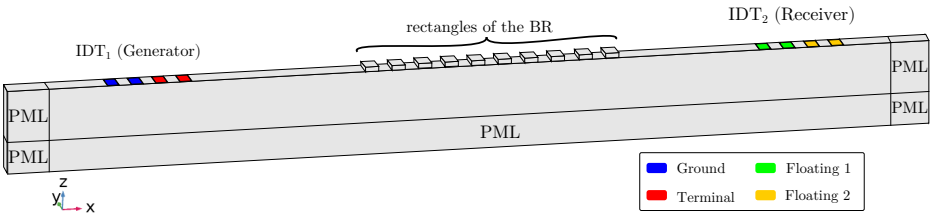

Figure 2.5: Example of a 2-port device composed of split-finger IDTs defined by surface domains and one Bragg mirror (with 10 pillars) build with an array of rectangles. We apply periodic boundary conditions to the surfaces on the front and on the back of the model. Therefore, what is simulated is a structure with the desired number of pillars and cavities in the X-direction, but infinite in the Y-direction. That is why we call this a 'pseudo 3D' model.

on the fact that some detail or even an acoustic mode may be lost or suppressed in the simplifications done to diminish the computational cost. Nonetheless, we verified that this was not the case. So the model served as an additional verification step of the robustness of the other models but, as the computation time increased too much, its usefulness was severe limited.

To give an idea of how much time each of the simulation models take for to calculate one frequency point we refer to the table 2.1.

2.4 Experimental details

In this section we give more details on the fabrication of our devices and experimental protocols used to measure them.

2.4.1 Fabrication

As already stated in the Introduction the main process used to fabricate our devices is photolithography. Here we explain the technique in detail (see Fig. 2.6 for a scheme). The whole process requires several steps. The

Table 2.1: Time scale and the number of degrees of freedom (DOF) to solve for of some specific simulation models. The time refers to the calculation time of one frequency point. The DOF are the nodal variables, namely the displacement field and the electric potential.

Model	**Structure**	**Time (min)**	**DOF**
2D eigenfrequency	2 strips	0.07	54000
2D, X-direction	5 cavities, 20-strips BRs	0.21	400000
2D, Y-direction	2 cavities, 120-strips BRs	0.45	780000
3D eigenfrequency	1 rectangle (unit cell)	0.28	54000
pseudo 3D, X-direction	2 cavities, 40-strips BRs	1.6	850000
pseudo 3D, Y-direction	2 cavities, 120-strips BRs	18	2400000

first one is the removal of any residues and moisture of the surface of the substrate, usually a 2 to 4 inch wafer. After cleaning the wafer, a thin layer of a resist is spin coated on its surface and then baked on a hot plate. The baking is used to evaporate the coating solvent and to harden the resist. Then the resist is exposed to a pattern of intense light*. The desired pattern is drawn on a mask, usually made of chrome on glass. The parts exposed to the light suffer a chemical change that allows some of the resist to be removed by a solution called 'developer'. Positive resist becomes soluble in the developer when exposed, while for negative resist, is the unexposed regions that are soluble. Then, a series of chemical treatments either etches the exposure pattern into the material or enables deposition of a new material in the desired pattern on top of the wafer. In our case, we use deposition followed by a final step which is called 'lift-off'. Lift-off consists in dissolving the layer of photoresist, removing the deposited material from unwanted areas. In addition, there are other means of exposing the resist

*The most widely used technique today is photolithography which uses UV light for exposure. However, there are other technologies such as electron beam and x-ray lithographies that provide better resolution due to its smaller diffraction limit.

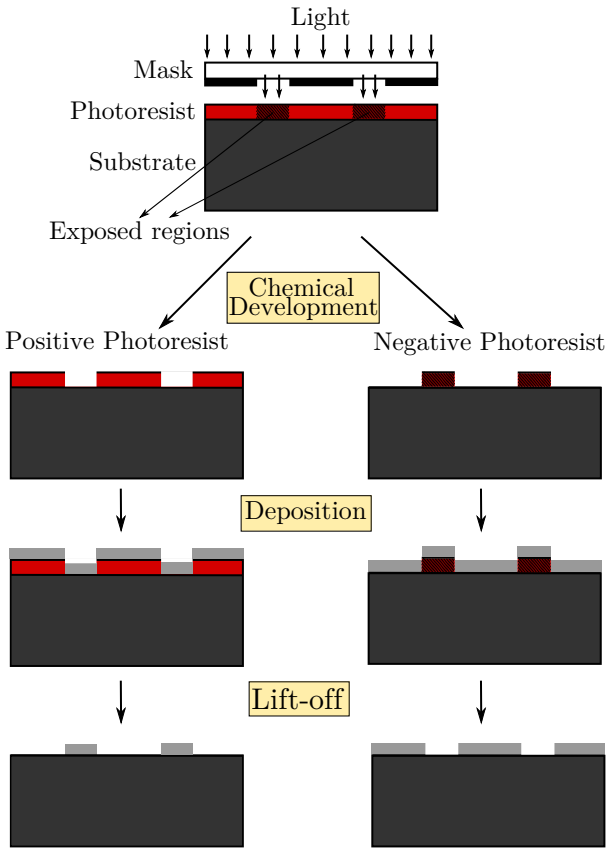

Figure 2.6: Scheme of a standart photolithography process followed by the deposition of the desired material and subsequent lift-off.

which do not use UV light for the its chemical change. One other method is named electron beam lithography (EBL). EBL is a direct writing technique that uses an accelerated beam of electrons to pattern features on substrates that have been coated with an electron beam sensitive resist. In the same way as the UV light does, the exposure to the electron beam changes the solubility of the resist, enabling selective removal of either the exposed or non-exposed regions of the resist by immersing it in a developer. The

main advantages of EBL over photolithography is that there is no need for a mask, the exposure is done directly by the beam of electrons controlled by electric and magnetic fields, and the resolution can be as small as 10nm. Whereas for photolithography, the resolution is limited to 180 nm. However, EBL is a much more expensive and time-consuming process. It was used to fabricate the photomask, i. e., the piece which was then used to select the exposed parts of the wafer during the photolithography. Also, it was the chosen method to fabricate the samples during the stay at Chalmers, due to the small pitch of the IDTs required for the high frequency resonators used in the experiments there.

The missing link in the whole fabrication process is how the metal is deposited once the pattern is written into the resist. This was done by resistive thermal evaporation, one of the simplest of the physical vapor deposition (PVD) techniques. Basically, the chosen material for depositing is heated, using electrical energy, in a vacuum chamber until its surface atoms have sufficient energy to leave the surface. The vaporized molecules then travel from the source to the substrate where they nucleate together, forming a thin-film coating. High levels of vacuum are needed for two reasons. First, because when gas is evacuated from a chamber, vapor molecules inside it can travel longer distances before they collide with a gas molecule. That is, the mean free path must be longer than the distance between evaporation source and substrate. Collisions with gas molecules are undesirable during evaporation because they change the direction of travel of material vapor and thus can adversely affect the coverage on the substrate. The second reason is film purity. Gases that are present in air can be deleterious to film properties if they become incorporated into the deposition. If Aluminum is deposited in the presence of oxygen, for example, it will form Aluminum oxide.

2.4.2 S-parameters

At radio frequency (RF) and microwave range of frequencies, measurements of current and voltage are very complex. It is difficulty to obtain perfect opened and shorted circuits standards over a broad bandwidth, and active devices may be unstable under open/short conditions. To overcome this problem, voltage, current, or power emanating from a source impedance, Z_s, and delivered to a load, Z_l, can be considered to be in the form of incident and reflected waves traveling in opposite directions along a transmission line of characteristic impedance Z_0. If $Z_l = Z_0$ then the incident wave is totally absorbed in the load. If $Z_l \neq Z_0$ then some of the incident wave is not absorbed in the load but is reflected back towards the source. If $Z_s = Z_0$ then the reflected wave would be absorbed by the source entirely. For $Z_s \neq Z_0$ the reflected wave from the load is re-reflected from the source back toward the load and the entire process repeats itself. In summary, the degree of mismatch between Z_0 and Z_l, or Z_s, determines the amount of incident wave that is reflected. The ratio of the reflected wave to the incident wave and the ratio of transmitted wave to the incident wave are known as the reflection and the transmission coefficients, respectively. These figures of merit, in RF experiments are known as the *S-parameters*. S-parameters refer to the scattering matrix of a microwave network (the "S" in S-parameters refers to scattering). The 1948 Radiation Laboratory series, "Principles of Microwave Circuits" [26] introduced the emerging microwave community to practical approaches to solving microwave design problems using scattering parameters in the design of circuits.

They are defined as follows (see Fig. 2.7): a portion of the wave coming from a source and arriving at port 1 will be reflected (b_1) and another portion will be transmitted (a_1) through the two-port device. A fraction of the transmitted signal is then reflected (a_2) from the load and becomes incident upon the output port (port 2). A portion of this signal (a_2) is then reflected from the output port back towards the load (b_2), while a

fraction is transmitted through the two-port device back to the source. The S-parameters connects all these quantities mathematically:

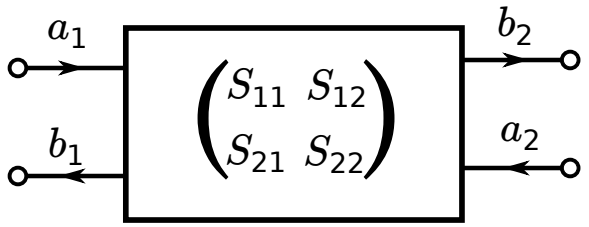

Figure 2.7: Generalized 2-port network. a_1 and a_2 are the incident waves while b_1 and b_2 are the reflected waves on the respective ports. S_{11} is the input port voltage reflection coefficient; S_{12} is the reverse voltage gain; S_{21} is the forward voltage gain; and S_{22} is the output port voltage reflection coefficient.

$$\begin{aligned} b_1 &= S_{11}a_1 + S_{12}a_2 \\ b_2 &= S_{21}a_1 + S_{22}a_2 \end{aligned} \qquad \begin{pmatrix} b_1 \\ b_2 \end{pmatrix} = \begin{pmatrix} S_{11} & S_{12} \\ S_{21} & S_{22} \end{pmatrix} \begin{pmatrix} a_1 \\ a_2 \end{pmatrix} .$$

S-parameter magnitudes are presented in linear magnitude or logarithmic based decibels (dB). Because S-parameters are complex voltage ratios, the formula for decibels in this case is

$$s_{ij} = 20\log_{10}|S_{ij}| .$$

We usually present our results in dBs subtracted by the corresponding s-parameter of a delay line (same IDTs but no structure in between). This way, zero transmission means that the signal did not change with the introduction of the structure under test.

2.4.3 Typical experiment

The usual experiment done to access the behavior of the designed cavities involves the use of a probe station in which two positioners are

located. Each positioner holds an metallic arm which carries a Z-probe of 250 μm separation fabricated by Cascade Microtech (see Fig. 2.8). Each tip of the probe contacts each pad of an IDT structure. These probes are connected to a Vector Network Analiser (VNA) with a 50 Ω reference impedance used to register the s-parameters for each device under test. The typical measurement is executed at 0 dBm power, 100 kHz IF bandwidth and averaged 16 times. One crucial step has to be done before presenting the results though. A fast Fourier transform is performed on the raw data in order to avoid the signals from cross talk and unwanted reflections (from different structures on the wafer or from triple-transit). In Fig. 2.9 we show one example of the filtering process of a measurement. We first do the Fourier transform, passing the data from the frequency to the time domain. Then, knowing the velocity of the wave and the distance between IDTs we select only the part of the signal which is related to the structure under test. Next, the inverse Fourier transform is done, which gives us the final experimental result. In Fig. 2.10 we display one example of such procedure for a three cavity device, showing the raw and treated data.

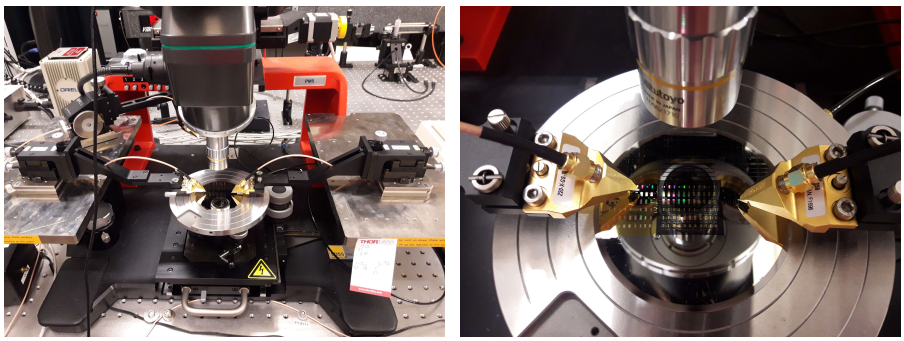

(a) **(b)**

Figure 2.8: (a) Photo of the probe station. Each positioner holds a Z-probe which is connected to one port of the vector network analizer. (b) Z-probes in detail. The tips are used to touch the pads connected to the IDTs of each structure siting on the wafer.

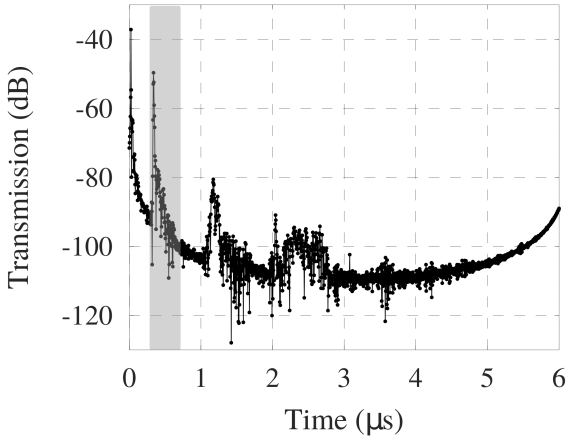

Figure 2.9: Fourier transform of the data from Fig. 2.10a showing the raw data in the time domain. The selected signal is highlighted in the gray area. We identify the peak near the origin as coming from cross talk and the subsequent signals, outside of the selected range,as coming from triple-transit and other structures on the wafer. As we know the velocity of the wave and the distance between IDTs it is easy to identify and select the relevant points.

For the experiments performed during the stay at the Chalmers Institute in Gothemburg, a different setup was used. There, the experiments were performed in very low temperatures, inside a Helium-3/Helium-4 dilution cryostat at base temperature of 10 mK. The sample was bond to a sample holder and connected to VNA which was set to measure transmission. However, what was really measured from the sample, being a one port resonator, was the reflection. This was the case because a circulator was involved (see Fig. 2.11a). A circulator is a passive three-port device, in which the radio-frequency signal entering a port is transmitted only to the next port in rotation. This way input and output signal could be separated in the different lines of the cryostat. This is done to avoid that the entering signal caused a temperature rise. The inputs are connected to a series of attenuators to avoid heating up the fridge, while the output is connected

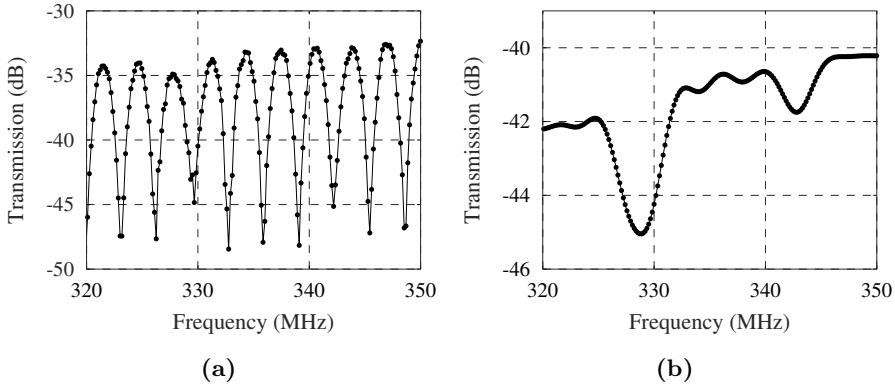

Figure 2.10: Example of a Fourier filtering of the data from a three cavity device. (a) Raw data in dB. No structure can be identified because signals from cross talk, triple-transit and from other structures on the wafer are all mixed up. (b) Data after filtering is performed.

with a series of amplifiers, so that the signal can be read.

The dilution cryostat used (Fig. 2.12) to achieve such low temperature works with a mixture of ^{3}He and ^{4}He. When a mixture of the two stable isotopes of helium is cooled below a critical temperature, it separates into two phases (see Fig. 2.11b). The lighter "concentrated phase" is rich in ^{3}He, and the heavier "dilute phase" is rich in ^{4}He. The concentration of ^{3}He in each phase is temperature-dependent. Since the enthalpy of the ^{3}He in the two phases is different, the "evaporation" of ^{3}He from the concentrated phase into the dilute phase may provide highly effective cooling. In a gross simplification, the concentrated phase of the mixture is pretty much liquid ^{3}He, and the dilute phase is effectively ^{3}He gas. The ^{4}He composing the bulk of the dilute phase is inert and noninteracting, and may be neglected. The evaporation of ^{3}He from the "liquid" phase to the "gas" phase cools the sample. This process works even at the lowest temperatures because the equilibrium concentration of ^{3}He in the dilute phase is finite even at zero temperature. When the refrigerator begins operation (see Fig. 2.12

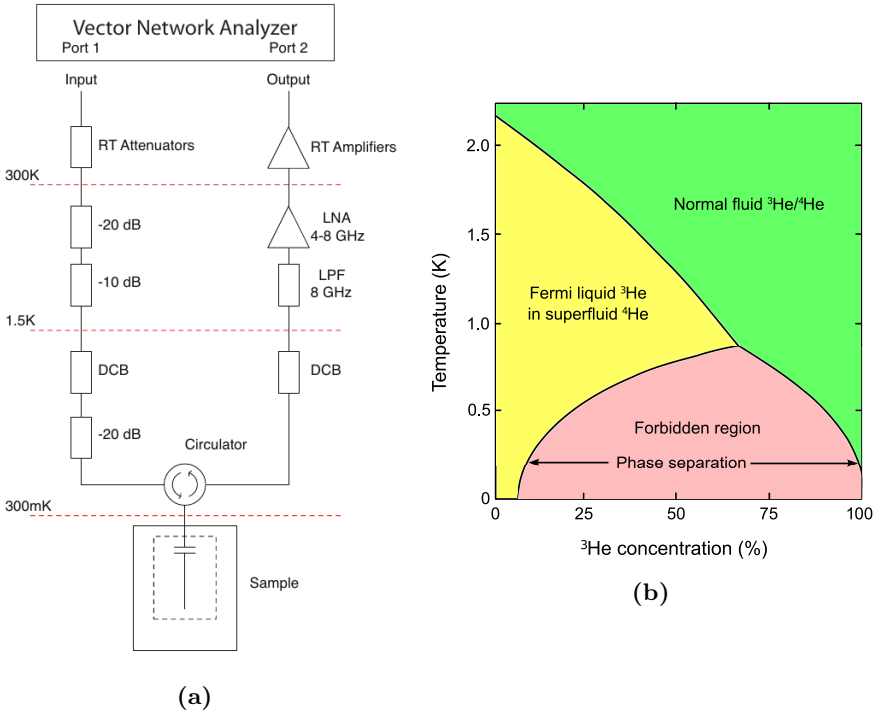

Figure 2.11: (a) The internal electronics of the cryostat measurement lines. RT is room temperature, LNA is low noise Amplifier, LPF is low pass filter and DCB id direct current blocker. Above the 300 K dashed line are room temperature amplifiers and attenuators outside the cryostat. Via circulator, the signal from port 1 (input) of the VNA is directed to the sample after passing the attenuators. The signal reflected from the sample enters port 2 (output) after being amplified. (b) Phase diagram of the ^{3}He ^{4}He mixture. The phase separation under approximately 0.8 K is exploited in the dilution cryostat.

for a scheme), the 1K pot is used to condense the ^{3}He/^{4}He mixture in the dilution unit. It does not cool the mixture sufficiently to form the phase boundary, but simply to bring it to 1.2K. Phase separation may be attained only once the temperature falls below the tri-critical point at

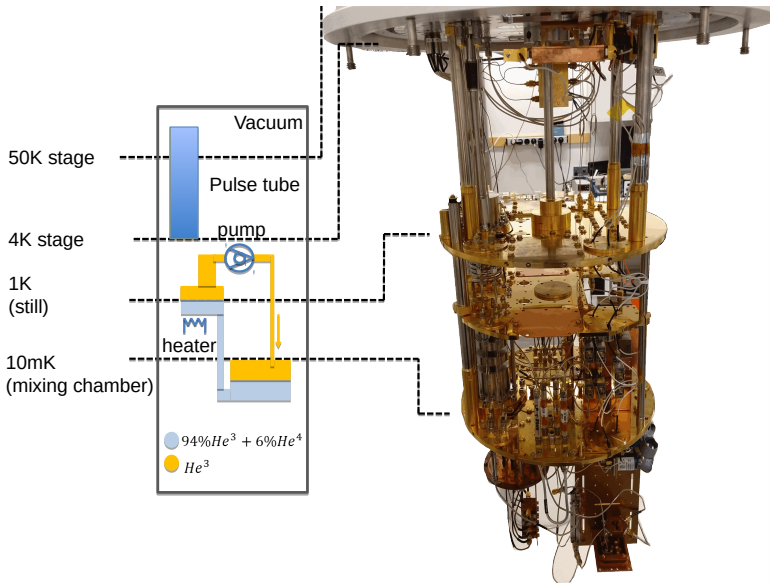

Figure 2.12: Photo of the cryostat with a schematic of its most relevant components.

0.86K. This cooling is provided by the still; incoming ^{3}He is cooled by the still before it enters the heat exchangers and mixing chamber. Gradually, the rest of the dilution unit cools to the point where phase separation occurs. It is important that the ^{3}He concentration and volume of the mixture are chosen correctly, so that the phase boundary occurs inside the mixing chamber and the liquid surface lies in the still. If this is not done, the fridge will not cool to base temperature. Thus it is critical to preserve the balance of the mixture. During continuous operation, the ^{3}He must be extracted from the dilute phase (to prevent saturation) and resupplied to the concentrated phase. The ^{3}He is pumped away from the liquid surface in the still where, at ≈0.6K, ^{3}He evaporates preferentially (1000 times faster than ^{4}He). ^{3}He leaving the mixing chamber is used to cool the returning flow of concentrated ^{3}He in a series of heat exchangers.

A room temperature vacuum pumping system is used to remove ^{3}He from the still and compress it before passing it through impurity-removing filters and cold traps (one at 277K, the other at 4.2K) and returning it to the cryostat. The inflowing mixture is pre-cooled by the main helium bath and condensed on the 1K pot. A flow impedance (in the form of a capillary tube) is used to maintain a sufficiently high pressure in the 1K pot region for the gas to condense. The experimental apparatus one wants to measure is mounted in the mixing chamber to ensure adequate thermal contact.

2.4.4 Interferometry measurements

As we deal with planar devices, a detailed investigation of the acoustic field distribution of the coupled acoustic cavities can be performed by optical means. Diffraction techniques [27], deflection techniques [28], microscopic reflectance and reflectance anisotropy [29] as well as interferometric techniques [30, 31] can be applied to that matter. Non-optical techniques such as atomic force microscopy or scanning tunneling microscopy can be used to access the SAW field as well. However, while non-optical approaches have the sensitivity and resolution required to image SAW, optical ones are preferred because they are non-contact methods that do not perturb the SAW. In addition, they do not place any restrictions on the temperature of the sample.

For this work, a Michelson interferometer was used to image the acoustic field (see Fig. 2.13 for the setup) giving us complementary information regarding the distribution of the field along the probed structures. The interferometer works by the use of a beam of a 532 nm single-mode laser which is sent to a beam-splitter (BS). One beam goes to a mirror (M) which is mounted on a piezoelectric stand. The second beam is focused onto an approximately 1 μm spot on the surface of the sample after going through a microscope objective. This beam then interferes with the reference beam at a fast photodiode. If the light beam reaching the sample is in the

way of a SAW, the interference pattern will oscillate with a frequency equal to that of the SAW frequency and an amplitude proportional to the SAW amplitude. The amplitude of the interferometric oscillations induced by the surface displacement δz depends on the difference in path length of the interferometer arms, which is controlled by δm ($\delta z << \delta m$). The maximum sensitivity to the surface displacement is obtained when $\delta m = (2m+1)\frac{\pi}{2} (m = 0, 1, ...)$, leading to $I_D = A(1 + \sin(\delta z - \delta m))$. If $\delta z - \delta m = 0[2\pi]$, the amplitude will be minimal while the frequency will double to f_{SAW}. This information will be used by the lock-in amplifier to settle the piezoelectric mirror to the optimum position. This setup provide us with sufficient spatial and time resolutions to discern individual wavefronts. By using a spectrum analyzer, the photodiode signal is detected at the first side band of the SAW frequency, which is proportional to the time-averaged squared amplitude of the vertical particle displacement. The measured signal, however, is modified by the optical reflection of the surface being probed. That is, as the surfaces of the substrate and of the metal used for the perturbations differ in their reflectivity, a higher or smaller signal will be measured depending on the proportion of light reflected from each surface. In the regions where there are interfaces between the metal-coated and metal-free regions, each gives a contribution to the interferometric signal which the exact proportion cannot be known. This is the reason why, when we present the results, one can clearly see the rise or fall of the displayed amplitude connected to the specific area of the device which is being probed. The spatial profiles obtained by scanning the laser beam, nonetheless, provide very useful information about the energy distribution along the surface of the samples, a feature which cannot be accessed by the electrical characterization.

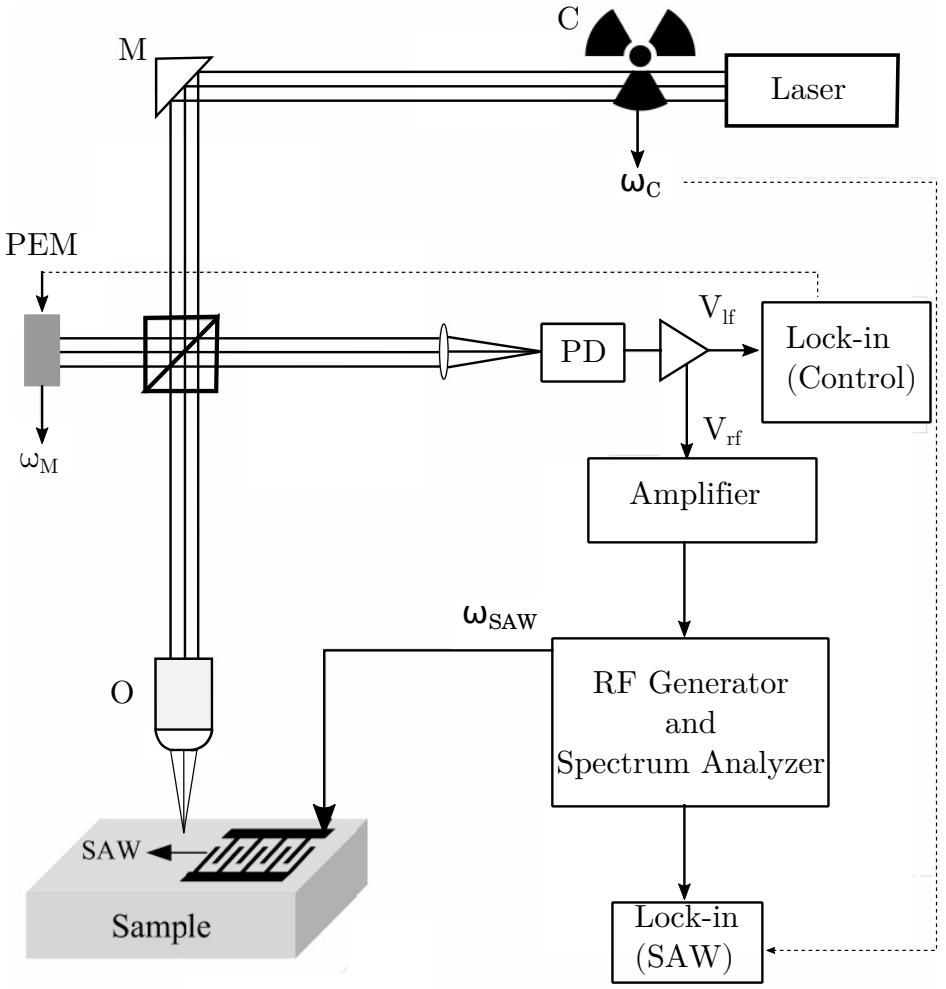

Figure 2.13: Experimental setup for microscopic optical measurements where A is the analyzer, BS is the beam splitter, C is the chopper, M is the mirror, O is the objective lens, P is the polarizer, PD is the photodiode and PEM is the photoelastic modulator.

3

Results

After an introduction on the methods, simulations models and experimental details we are now in position to present the original results reached during our investigation. Reviewing the timeline, we started by improving the 2D simulations in order to be aware of the different parameters that we could use to have a higher degree of control of the acoustic fields of the devices. Being capable of designing devices with more accuracy, better predicting the measurements outcomes, we explored on the idea of tuning them. Applied heat was an option we could implement straightforwardly and that gave us interesting results. Being more conscious about the effects of temperature change on the cavities we reached out to one of our network partners which had experience in measuring SAW cavities at low temperature. The outcome was a successful collaboration which resulted in an idea for improving the quality factor of the cavities. And lastly, it was somewhat natural the subsequent extension of our simulation into the 3D realm, followed by the experiments coupling cavities in two dimensions. In a nutshell, that sums it all. On the following sections we dissect each of the cited developments, giving the broad context in which they are inserted in.

3.1 Simulations compared with previous work experiments

While developing our simulation model, as a mean of confirming the effectiveness of it, we ran the simulations with the nominal parameters of the samples used in previous experiments. We varied both the number of cavities and the electrical boundary condition of the strips in the BRs, simulating the same devices which appear in the Introduction. That is, BRs of 20 gold strips and cavities of $3\lambda_{SAW}/2$ size on top of a 128°-rotated Y-cut $LiNbO_3$ substrate, being $\lambda_{SAW} = 11.2\ \mu$m. As it can be seen in Fig. 3.1, the simulation agrees very well with the experiments, especially in the shorted case. For the shorted BRs, the small discrepancies observed between the theoretical and experimental spectra can be partially attributed to limitations off the fabrication process. Roughness and inhomogeneities of the metal fingers impede the Bragg mirrors to reach its full reflection capacity, a feature not present on the simulation since the distance between strips can be made with arbitrary precision, as long as the mesh is fine enough. The same argument holds for the transduction on the fingers of the IDT. In addition, the electrical boundary conditions are implemented in our model by forcing all strips to be at zero potential. In reality, the non-zero resistivity of the metal results into departure of the propagation velocity of the ideal case. Moreover, in the samples, a small layer of NiCr is deposited under the gold strips for better adhesion, a detail not included in our model. Nonetheless, we stress the fact that we use no adjustment parameters and the simple 2D model implemented is more than enough to predict all relevant features, even without the small corrections above mentioned. For the floating BRs the discrepancies are more intricate. We know from COM theory (and others theoretical models) that with the increase of the reflectivity of the strips and BRs there is an increment in the depart between theory and experiment. There they attribute this

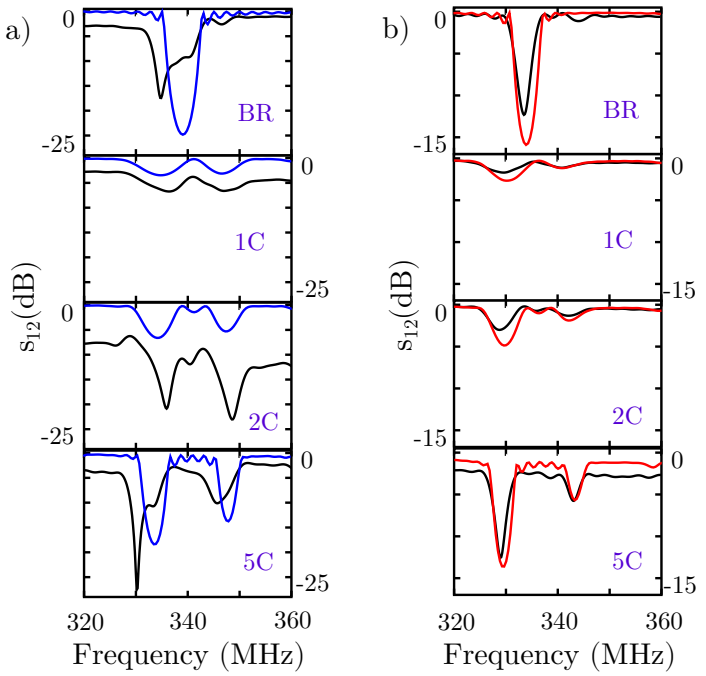

Figure 3.1: Comparison between 2D simulations (solid black lines) and experimental results for (a) floating and (b) shorted devices. We plot the transmission parameters (s_{12}) in dB of each structure subtracted by the transmission of a delay line (no structures between IDTs).

to velocity shifts due to waveguiding and other 3D effects (coupling to shear waves) [18]. Also, some problems can occur when short* devices are under investigation, once that the theory is developed considering infinite structures. Here, we believe that the higher reflectivity in the floating case induces an "effective thin film" under the BRs which, in Y-cuts of $LiNbO_3$, is a know method to generate leaky surface waves (LSAW) [32]. This would explain the attenuation and deformation we see in the signal. Our suspicion that 3D effects do not play a part here is based on the subsequent

*Short meaning small. That is, whose total length is not orders of magnitude bigger than the size of the perturbation

3D simulations we did of the same devices (see Fig. 3.2). In principle we

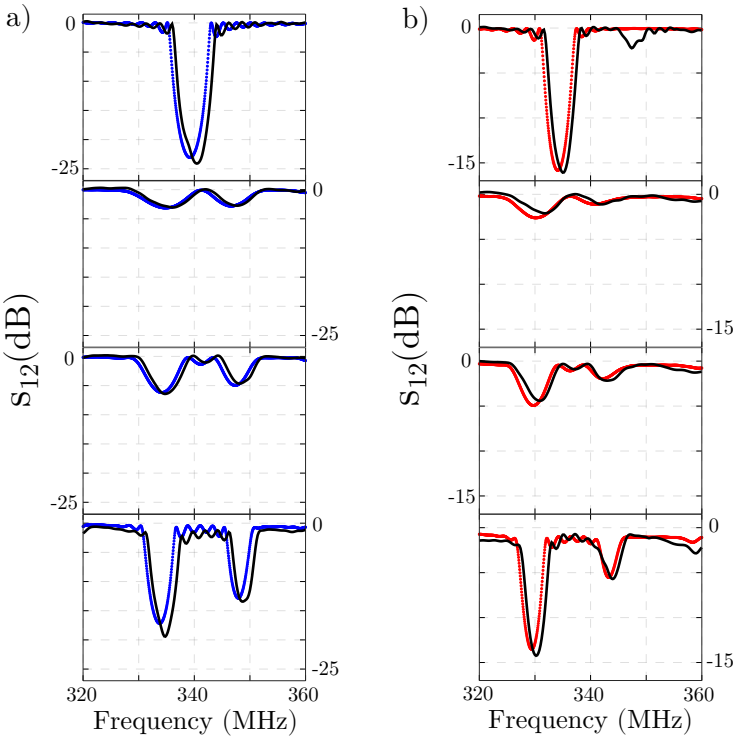

Figure 3.2: Comparison between 2D and 3D simulations. a) Transmission for the floating configuration. 2D (blue dots) and pseudo 3D (black solid lines). b) Transmission for the shorted configuration. 2D (red dots) and pseudo 3D (black solid lines).

cannot completely discard the coupling with shear modes, given that we use the 'pseudo 3D' model to simulate. So one could argue that, in a full 3D model, there could appear a different mode. However, as the possibility of vibration in the perpendicular direction to the saggital plane is indeed open in our model, we tend to reject that a full 3D simulation would give a different result. All things considered, we note that, in both models, there is excellent agreement with the experiment and the resonant frequencies

are predicted with less than 1% accuracy.

3.2 Eigenfrequency study

Another way to visualize how the waves behave according to different sets of parameters is to run an eigenfrequency study. This simulates a small part of the device in which a periodic boundary condition is applied. By doing so, the model extracts the *natural* frequencies of vibration that arise from the material under study considering that, on the selected boundaries, the physical quantities (such as displacement or electric field) repeat themselves. Even though this configuration is not as realistic as the whole 2D modeling, it is useful as a very quick mean of checking how the waves respond to the variation of the size and kind of material used on top of different substrates. And especially, the variation of the electric boundary condition selected - floating or shorted, as already discussed before. In Fig. 3.3 one can see how the eigenfrequencies calculated can change as the strips are introduced in the model. In a) the eigenfrequencies are degenerated, whereas in b), it splits into two. By modifying the electric boundary condition under the strips we can appreciate the differences between different settings. Fig. 3.3c exhibits the results of this study where the height of the strips is varied. We note that one of the eigenfrequencies, f_1, changes according to the electric boundary condition, while f_2 is not affected by it. The reason is that f_2 is related to the state where the energy of the waves is more concentrated under the air gap between strips, therefore being insensible to the potential underneath. f_1, on the other hand, relates to the state where the energy is more concentrated under the strips, being more affected by their condition. Both eigenfrequencies are, nonetheless, affected by the mass loading which decreases the velocity of the waves.

Apart from that, there is another important feature which can also be

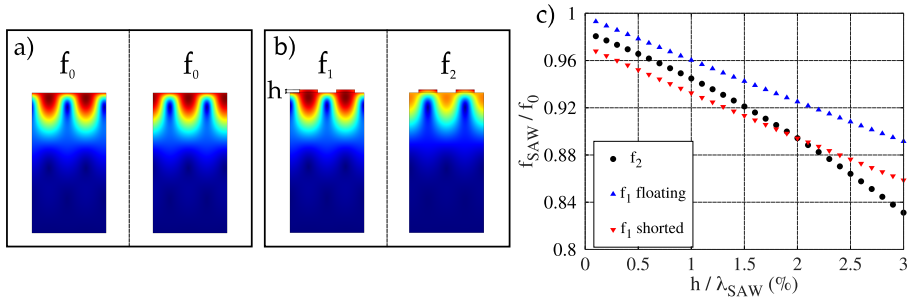

Figure 3.3: In a) there is no strips on top of the surface, and both eigenfrequencies are degenerated. In b), now with the strips, the frequencies differ. c) Comparison between floating and shorted strips for the normalized resonant frequencies versus the relative thickness of the strips, h. As can be seen, f_2 remains the same regardless of the electric boundary condition, while f_1 is influenced by it.

learned from this study. In the Introduction, in the Bragg reflector section, we mentioned that the stop band generated by a mirror was a function of the reflectivity of each strip, r, and that this quantity is composed of a mechanical and an electrical part. This means that, once the height and the electric configuration of the perturbation is chosen, the width of the stop band is fixed, regardless of the number of strips used. The number of strips will determine how much of the incident energy is reflected. The more strips, the higher is the total reflection, i. e., deeper the stop band. Here, we would like to bring the attention to the fact that the difference between eigenfrequencies is connected to the bandwidth. A bigger difference between f_1 and f_2 directly implies a wider bandwidth which, in turn, signifies a higher reflection. Therefore, this study can be exploited to estimate the efficiency of the perturbation. Note that, on Fig. 3.3c, for the shorted configuration, there is a combination of parameters for which $f_1 = f_2$. For this particular situation, the mirror would be invisible to the wave and no reflection would take place. This is related to the fact that, in this peculiar

case, the mechanical and electrical reflectivities of the strips have opposite signs while having the same absolute value. Both conditions combined translates in the overall reflection going to zero. This strategy could be applied to improve the power delivered by long single finger IDTs, for example (this was investigated for embedded IDTs [33]).

3.3 Thermally dynamical tuning

Being more confident about predicting the behavior of our devices allowed us to pursuit other objectives. One of the concerns we had was to achieve experimentally the tuning of our structures. That is, to have some degree of control on the functioning of the coupled cavities so that the acoustic field in different parts of the structure could be tuned by means other than the frequency excitation. We know that lately, a lot of effort have been made to achieve this in similar devices. Among them some ideas are: use of variable impedances [11, 34, 35, 36], external magnetic field [37], acoustoelectric interaction [38, 39], electrostriction [40, 41] and thermal modulation [42, 43]. We developed further on the last of these effects. By exploiting the thermal instability of the substrate as a tool to control the acoustic field we demonstrate a continuous, memoryless and dynamical tunable device. This was achieved by applying a DC voltage to the ends of the metal grid of the shorted BRs of some structures. The electric current through the metal cause a temperature rise due to resistive heating, which changes the frequency response of the device. This effect was used to achieve to up to 0.3% frequency variation.

We focused specifically in a device with three cavities (see Fig. 3.4)[†]. The split-finger aluminum interdigital transducers (IDTs) of the delay lines were designed for an acoustic wavelength of $\lambda_{SAW} = 11.2$ μm, which

[†]Nominal parameters of the device are the same as the ones in the coupled cavities devices of the Introduction. We repeat here for convenience.

corresponds to a center resonance frequency of approximately 340 MHz for a Rayleigh wave propagating in the X-direction. They are formed by only 3 pairs of split-fingers, which makes them very broadband. This way, each of the resonances can be equally excited. The coupled cavities were fabricated by depositing NiCr/Au gratings with thicknesses $h = 10/110$ nm within the SAW delay lines.

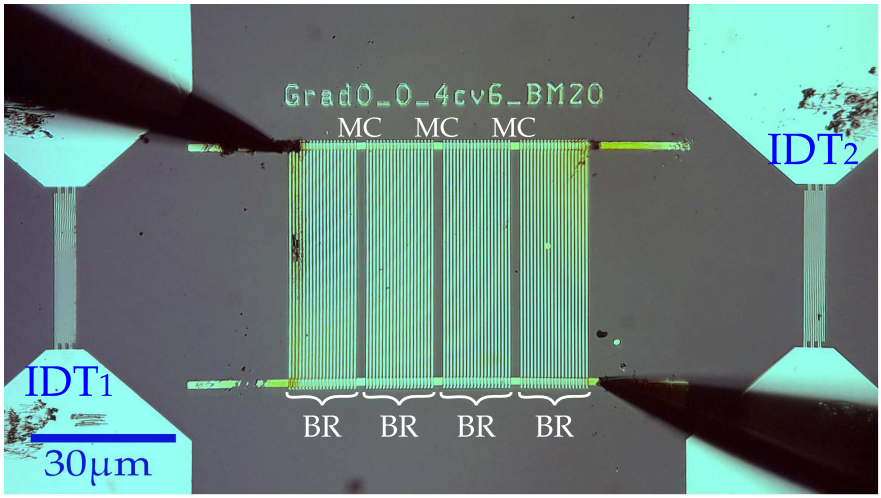

Figure 3.4: Micrograph of sample with 3 microcavities(MC) defined by metal strips forming Bragg reflectors (BR). The transmission (s_{12} parameter) between IDTs 1 (source) and 2 (detection) is measured while a voltage is applied at the tips contacting the opposite ends of the metal grid.

Due to the coupling, the acoustic field can be activated in different regions of these multi-cavities device by exciting it with different eigenfrequencies. Investigations in which SAW are coupled to quantum emitters, for example, could take advantage of that [44]. Moreover, several works on sensors report an improvement on sensibility due to the use of coupled resonators [45]. The tunability introduces a new degree of control by which one can, for example, switch from a high transmission state to a low transmission one (from a peak to a valley) while keeping the same

frequency excitation.

By the use of shorted devices we contacted the ends of the grid (see Fig. 3.4) with a 5 μm copper tip and applied a DC voltage, V_S, on it. In Fig. 3.5a one can see the frequency shift on the transmission spectrum of the device of three cavities for $V_S = 3\ V$ as compared with the response without applied voltage. The mechanism behind this effect is the resistive heating of the metal grid which warms up the sample. The temperature rise changes the relevant parameters of the substrate, such as the elastic and piezoelectric constants, resulting in the frequency shift that we observe. In this matter, the so-called temperature coefficient of frequency (TCF) is used to characterize the temperature stability of materials. The value for the 128°-rotated Y-cut $LiNbO_3$ is of -76 ppm/°C [46], which, for a 0.16% frequency change corresponds to a temperature variation of 20 °C approximately.

The behavior of this shift according to the applied voltage can be seen in Fig. 3.6a. It is worth to comment that we could not apply higher voltages due to the fragility of the thin gold layers deposited. Nonetheless, we note that the shift could reach higher values if the grid were more extended in space, covering a large area of the delay line. Moreover, going to higher frequencies would also allow a higher contrast, since the wave would be more concentrated on the surface where the temperature rise is taking place.

As a mean of verifying the consistency of this claim we have also performed simulations where we include the temperature dependence of the material parameters in the 2D model. The parameters changes due to temperature were implemented according to the measurements of reference [47]. We did this in COMSOL Multiphysics by defining a temperature dependent analytic function under the tab "Global Definitions". Then we simply set this function to each of the matrix elements of the relevant material properties, namely, the coupling and elasticity matrix as well as

the relative permittivity (under "Materials" tab, select the desired material and edit its properties). Each of these elements is, then, a function whose arguments are the temperature and the coefficients appearing in [47]. As it can be seen in Fig. 5.1b, the overall shape of the transmission, the difference between peaks and the shift due to the temperature rise, which are all the relevant physical parameters under consideration, are in excellent agreement with the experiment. Again, we stress the fact that we use no adjustment parameters and the simple 2D model implemented is more than enough to predict all relevant features, even without the small corrections mentioned earlier.

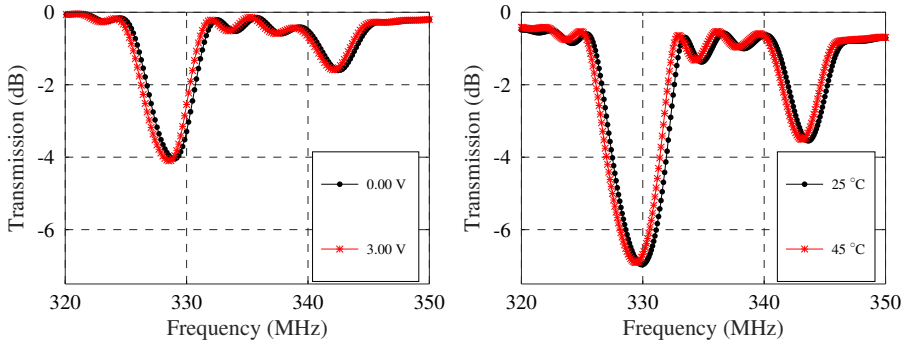

Figure 3.5: a) Measured s_{12} (in dB) of the structure with 3 cavities. With a voltage applied to the grid ("x" markers) the frequency is shifted due to the heating of the substrate underneath caused by resistive heating of the metal strips. b) Simulated s_{12} (in dB) of structure with 3 cavities. The 2D model was used to simulate the acoustic field propagation along the sagittal plane of the structure.

We then proceed to inspect the time scale of this process. For that matter we applied a 50% duty cycle square voltage, modulated from 0 V to 3 V. By inspecting how the transmission changes for a specific frequency (zero span measurement), the acquisition of data was fast enough for us

to probe the shift. Fig. 3.6b summarizes our findings. In it, three results are displayed: in black the transmission when no voltage is applied; in red, when a constant voltage of 3V is applied and in blue, when the square potential is on, all for a frequency of 332 MHz. By fitting an exponential decay $s_{12} = a\ \exp(-t/\tau)$, where s_{12} is the transmission, a is a constant and τ relates to the time scale of the process and averaging over several cycles we find $\tau_c \approx 220$ ms and $\tau_h \approx 160$ ms, where the subscripts c and h are related to the cooling and heating phases, respectively.

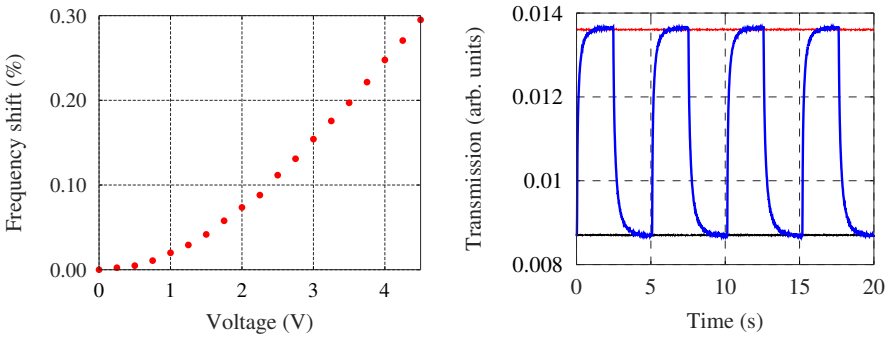

Figure 3.6: a) Frequency shift versus applied voltage of the first of the 3 peaks appearing in Fig. 3.5a. b) Measured s_{12} parameter (linear scale, arbitrary units) as a function of time (thick solid line) for square modulated potential on the tips changing from 0 V to 3 V at a repetition rate of 0.2 Hz. The frequency is fixed at 332 MHz. The bottom and top solid horizontal lines are the transmission s_{12} values for zero voltage and constant 3 V applied at the tips, respectively.

The units of the transmission here do not match the ones in Fig. 3.5a due to the fact that, on the latter, a gating is performed on the raw data. We do a fast Fourier transform in order to filter the signals from cross-talk and reflections from other structures on the wafer. However, data on Fig. 3.6b receive no such treatment because it is a zero span measurement.

By comparing our simulations to the experiments we have demonstrated that a plausible raise in temperature is compatible to our findings. However, more effects can occur due to the application of an electrical potential which are, likewise, used as a tuning resource. One is electrostriction [48], which causes a piezoelectric stiffning or is also used to induce piezoelectricity in nonpiezoelectric substrates [49]. Another is simply the strain that deforms the material, altering the path length of the wave. Nonetheless, approaches that explore one or both effects are fundamentally different from ours. They use the substrate as a capacitive mean. The voltage difference is applied either between top and bottom surfaces or on each of the IDTs, that is, on separated areas on the surface. Due to the dielectric properties of the substrate some have to use voltages on the order of kV. The strain caused by such an electric field distributed along the substrate is why its parameters are changed. In our case, however, the voltage is applied between different points of a piece of metal which sits on the surface. So the applied electric field is majorly confined to the metal. Moreover, some [40, 41] exhibit a memory effect. That is, the shift is seen to persist even after the perturbation is turned off. This makes them unsuitable for dynamical modulations like we show here, as it was already noted in [50]. Others depend on the bias signal [51], whereas ours is insensitive to that. These led us to conclude that the observed effect results majorly from the temperature rise.

In order to further support our claim that the observed effect is solely thermal we did an independent experiment in which no voltage was applied. On this setup we mounted the wafer on top of a hot plate and measured the transmission through the structure with three cavities for different temperatures, waiting the appropriate time for the stabilization of the system. The data we observed is consistent with the previous results. For comparison, we note that the same 0.16% shift that was observed when 3 V was applied, in this new experiment corresponds to a 10 °C

rise above room temperature. This result, together with the arguments presented above, proves that we are dealing with a simple thermal effect. The temperatures were measured with an infrared thermometer aimed at the top of the surface of the wafer. According to its specifications, from a distance of around 3 cm, it reads the temperature of a spot of 2.5 mm diameter with a precision of ± 2 °C.

Contrasting our method to the ones available in the literature we see some improvements. As already mentioned, the ones relying on electro- [40, 41] or magnetostriction [37] exhibit an hysteresis curve. Acoustoelectric [38, 39] require more complex fabrication due to the multi-layer structure. And thermal modulation [42, 43] do not mention dynamical tunability. Our results were published in [52].

3.4 Low temperature resonator (Chalmers)

The results achieved by exploiting the thermal response of the substrate made us more conscious about how a temperature change could affect the behavior of the cavities. As one of our network partners specialized in very low temperature experiments with SAW resonators, it was obvious to reach out to them for discussing the issue. The group we are referring to is the one of Prof. Dr. Per Delsing, from the Chalmers University of Technology, in Gothemburg, Sweden. They were also part of the SAWtrain network and one of the PhD projects was carried there, by Gustav Andersson, under the supervision of Prof. Dr. Delsing. After some early discussion on the subject, Gustav approached me with an idea about studying, with a SAW resonator at low temperature, sources of loss in superconducting quantum circuits. The idea was a suggestion of Marco Scigliuzzo, another PhD student from their group. His idea led to my three months stay at Chalmers, which led to a successful collaboration resulting in a publication [53]. In this section we present a short introduction on the subject followed

by the idea and the results achieved.

Within the study of superconducting quantum circuits, the so-called two-level systems (TLSs) are among the most important sources of loss that limits the performance of such devices. TLSs are tunneling states which have a broad distribution of energy splitting and can be thermally activated at low temperatures, causing anomalous properties and noise. Regarded as an uncontrolled intrinsic systems, they couple both to electromagnetic fields and to strain. These states occur due to either defects in the crystal structure or the presence of polar impurities. Recently, a lot of work have been done to understand their properties and mitigate the losses caused by TLSs [54, 55]. However, they have been studied since the 1960s and a quite established TLSs model was already developed in the early 1970s [56, 57, 58], prior to the emergence of superconducting qubits, in experimental and theoretical research on the ultrasonic properties of amorphous solids. Although the microscopic nature of TLSs is still not well understood, the phenomenological standard tunneling model (STM) [59, 60, 61, 62] describes successfully many of the low-temperature properties of amorphous solids, and we will use its theoretical results throughout our analysis.

Typically, the behavior of such systems is studied by measuring the lifetimes and resonance frequencies of superconducting resonators and qubits [63, 64, 65]. Nonetheless, TLSs have a strong influence on the propagation of sound waves, especially at the low power regime, being a very relevant loss channel. SAW devices have been used in a number of quantum acoustic experiments, coupling mechanical modes to superconducting qubits [66]. Exotic regimes of atom-field interaction have been demonstrated [67], as well as the controlled generation of quantum states of SAW [68]. Two-level systems have also been demonstrated to induce significant loss in SAW resonators at cryogenic temperatures [69]. The interaction occurs between a phonon and a TLS as an absorption followed by an emission

of another phonon due to the TLS relaxation. This mechanism explains the power dependence of the acoustic attenuation (see Fig. 3.8c)): with increasing acoustic power, the upper level saturates and, therefore, the number of effective TLSs decreases, diminishing these losses. We took advantage of the small free spectral range (FSR) intrinsic of the SAW resonators to perform a two-tone spectroscopy experiment. Probing one resonance at the low power regime while exciting a neighboring one with a second tone using higher power we could saturate the TLSs, recovering the quality of the resonator. This was the idea. As a matter of fact, two-tone spectroscopy of TLSs has been performed using the fundamental and harmonic modes of a superconducting coplanar waveguide resonator [70], as well as more recently with the two normal modes of a system of coupled resonators [71]. However, the large mode spacing of coplanar waveguide resonators limit these experiments to a small number of frequency points. In our experiments, as we deal with SAW, the devices exhibit a spectrum with multiple closely-spaced modes with small differences in spatial distribution, due to the short wavelength of sound. This allow us to access a big number of states, enabling us to probe the shape of the spectral hole burnt in the TLS ensemble.

The term "hole burning" stands as a generalized synonym for all kinds of saturation spectroscopic techniques in inhomogeneously broadened bands [72]. At the frequency where saturation is performed, a dip appears in the spectrum, the so-called hole[‡]. Here, as the absorption of the TLS ensemble is connect to losses in the resonator, we can inspect its linewidth by measuring the quality increase which is caused by the saturation of ground state TLSs.

[‡]In the solid state, inhomogeneous line broadening occurs because of structural disorder. For example, in a crystal there are lattice defects that cause statistically varying strain fields. These strain fields lead to statistically varying frequency shifts of the zero-phonon transitions of the probe molecules. As a consequence, the zero-phonon frequencies are spread out and the line experiences a broadening.

The measurements were carried out with a one-port SAW resonator composed of 50 pairs of aluminum double fingers IDTs and two 800 strips BRs separated by a distance $d = 1440\ \mu m$, evaporated on top of a GaAs substrate (see Fig. 3.7 for a scheme). The IDTs have a 1.2 μm period, designed to generate waves around 2.40 GHz while the BRs provide a stop band of approximately 40 MHz. With a free spectral range of FSR = v_{SAW}/L = 1.97 MHz, our device supports 20 modes within the stop band. The device was put inside a dilution cryostat which was kept at the base temperature of 10mK. The resonator was probed measuring the reflection of the IDT via a circulator. Two-tone experiment was done with a VNA probing the reflection on a resonance as a signal generator was used at the same port to pump a neighbouring resonance, thus populating TLSs.

The STM models a TLS as a particle in a double-well potential, where two minima of similar energy are separated by a tunnel barrier [56]. For the loss saturation of a single mode of frequency f_r , the standard theory derived from the STM [59, 62] gives

$$\frac{1}{Q_{int(n)}} = \frac{1}{Q_{TLS}(0)} \frac{\tanh \frac{hf_r}{2k_BT}}{\sqrt{1 + \left(\frac{n}{n_C}\right)^{\beta}}} + \frac{1}{Q_{res}} , \tag{3.1}$$

where Q_{int} is the internal Q-factor, Q_{TLS} the Q-factor corresponding to TLS loss and n (n_C) is the average (critical) phonon number in the resonator. Residual internal loss not due to TLS is represented by Q_{res}. The shape of the saturation curve is characterized by the phenomenological parameter β, where the scaling $\beta = 1$ is expected from the standard theory, while values $\beta < 1$ are commonly found in superconducting resonators. Since the temperature is low we use the approximation $\tanh[hf_r/(2k_BT)] = 1$ for the purpose of fitting. Fig. 3.8a shows the resonator spectrum measured with a vector network analyzer. The internal Q-factor is extracted from fits to the data and plotted as a function of probe power is in Fig. 3.8c. We observe an order-of-magnitude change with power, indicating that SAW

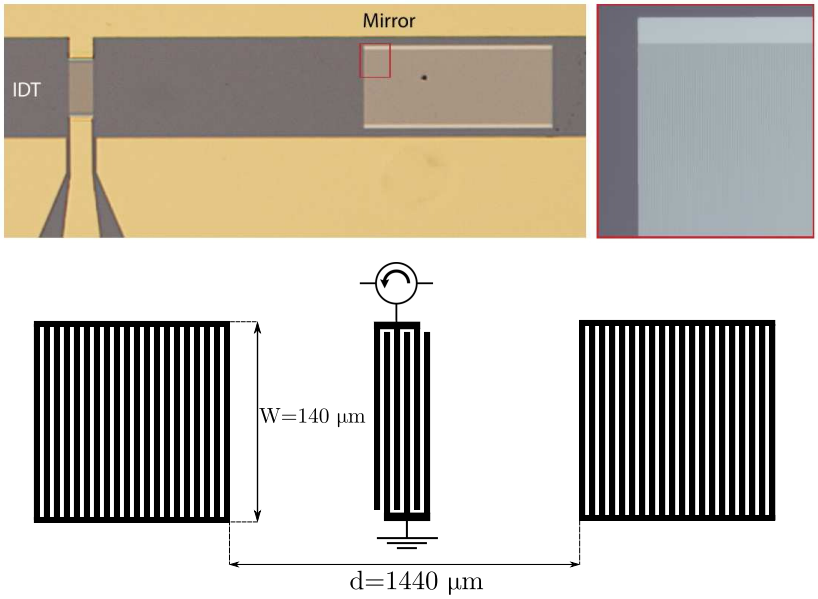

Figure 3.7: Microscope image showing the IDT and right hand Bragg mirror and schematic illustration of the SAW resonator. The IDT and mirrors are fabricated in aluminum on a GaAs substrate with gold ground planes. Inset shows part of the Bragg mirror. The IDT with 50 periods provides a coupling port and is centered with respect to the BRs. The mirrors have N = 800 fingers each that are shorted together. As the length of the resonator is more than 1000 wavelengths, the spatial distributions of the different modes are nearly identical. The resonator is measured in reflection using a microwave circulator.

propagation losses at low temperature are limited by TLS loss. Fitting to eq. 3.1, we find good agreement with theory and obtain $\beta = 1.05$, close to $\beta = 1$ as predicted by the STM. An example of fit to the pump mode resonance is seem in Fig. 3.8b. The resonances exhibit a non symmetrical character which makes the typical gaussian or lorentzian shapes unsuitable for fitting. Therefore, we used a Fano [73] shape [§] resonance in order to

[§]Other functions are indicated for this purpose as well, such as Voigt, pseudo-Voigt

get the Q-factors from the data.

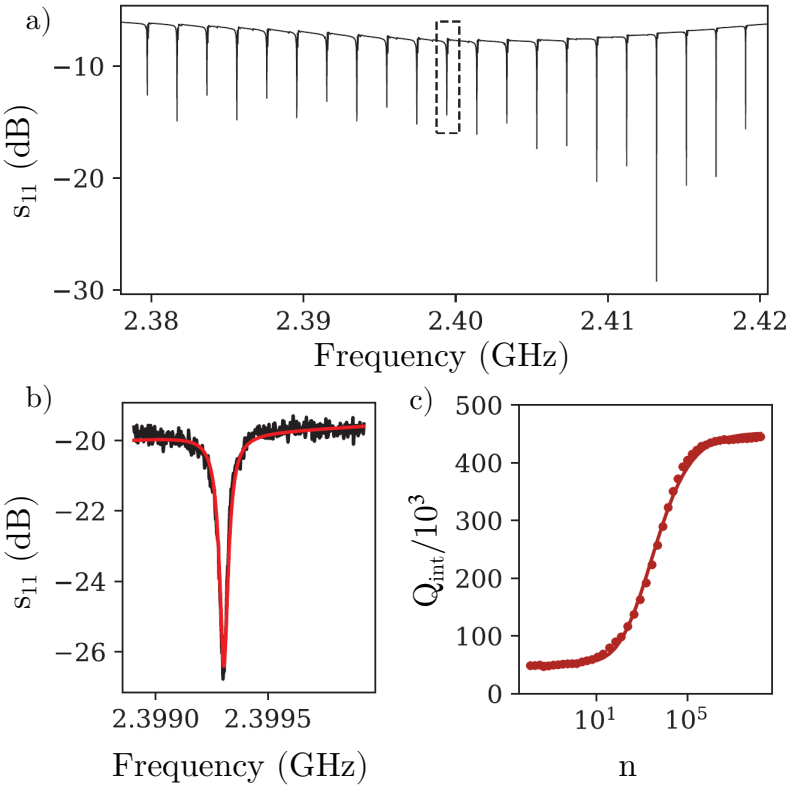

Figure 3.8: a) Reflection coefficient of the SAW resonator measured at high power ($n \approx 4 \times 10^5$). The dashed outline indicates the pump mode at 2.399 GHz. b) Example of fit to the pump mode resonance at low power ($n < 1$). c) Internal Q-factor as a function of phonon number for the pump mode (dots). The loss saturation is fitted (solid line) with eq. 3.1.

Let us focus now on the two-tone spectroscopy scheme. In this setup, a drive tone was applied at a mode in the center of the stop band ($f_r = 2.399$ GHz) and we probed a second mode. As the IDT response is frequency dependent, all the modes have slightly different external quality factors.

or sigmoidal [74], for example.

For this reason, we decided to have the pump fixed to a single mode, thus avoiding the pump power adjustments necessary to get the same average phonon number in different modes. The measurement then consists in sweeping the power in the pump mode and monitor the change in Q-factor and resonance frequency, mode by mode. This yields the loss and frequency shift as a function of phonon number in the pump mode n as well as pump-probe detuning $\Delta = \omega_{probe} - \omega_{pump}$. Based on the STM, expressions for the probe mode response were derived in [71], and give for the frequency shift

$$\frac{\delta f_r}{f_r \tanh \frac{hf_r}{2k_BT}} = -\frac{3\sqrt{2}\tan\delta}{8}\frac{\Delta}{\Omega}\frac{\sqrt{1+\frac{\Omega^2}{2\Delta^2}}-1}{\sqrt{1+\frac{\Omega^2}{2\Delta^2}}+1} \ . \tag{3.2}$$

The effective drive strength of the pump Ω may be expressed as $\hbar\Omega = 2\gamma A_{pump}$, where γ is the average elastic dipole moment coupling the TLS to the pump field of amplitude A_{pump} . This implies the drive strength depends on the average phonon number in the resonator as $\Omega \propto A_{pump} \propto \sqrt{n}$. Here, $\tan\delta$ is the dielectric loss tangent due to TLS. The frequency shift moves probe modes closer to the pump mode and for a given Δ it is maximized by a finite $n = n_{max}$. This can be understood from the dispersive interaction, where each off-resonant TLS contributes a shift $\Delta\omega_{r,i} \propto 1/(\omega_r - \omega_i)$ [62]. Saturating TLSs disables this interaction. For pump phonon numbers $n > n_{max}$, TLSs on both sides of the probe mode get saturated, and the frequency shift starts to diminish. For $n < n_{max}$ TLSs are saturated predominantly on one side of the probe mode. The average phonon number in a resonator driven at power P with a pump tone of frequency f_{pump} is given by [75]

$$\mathrm{n} = \frac{\kappa_e}{(\kappa/2)^2 + \Delta^2}\frac{P}{hf_{pump}} \ ,$$

being $\kappa_e \equiv \frac{\omega_r}{Q_e}$ and $\kappa \equiv \frac{\omega_r}{Q_l}$ the external and total decay rates, respectively. Thus,

$$\mathrm{n} = 4\frac{Q_l}{\omega_r}\frac{Q_l}{Q_c}\frac{1}{1+(2Q_l\Delta/\omega_r)^2}\frac{P}{hf_{pump}} \ .$$

Loaded and external Q-factors (Q_l and Q_e) are extracted by fitting the complex transmission data to an appropriate model [76].

Now, for the change in probe mode loss we have

$$\delta\left(\frac{1}{Q_{TLS}}\right)\frac{Q_{TLS}}{\tanh\frac{hf_r}{2k_BT}} = -1-\left(\frac{\Delta}{\Omega}\right)^2\left\{6+3\Theta\ln\left[1+\left(\frac{\Omega}{\Delta}\right)^2(1-\Theta)\right]\right\}, \tag{3.3}$$

where

$$\Theta = \sqrt{1+2\left(\frac{\Delta}{\Omega}\right)^2}.$$

The internal Q-factor as a function of pump power of modes detuned from the pump by 2, 4 and 8 times the FSR is shown in Fig. 3.9b along with fits to eq. 3.3. Comparing to the single mode loss, we note that saturation in detuned probe modes occurs at higher pump powers. At phonon numbers below single mode saturation ($n < n_s \approx 10^5$), only TLSs near-resonant with the pump mode are saturated, with little impact on the loss in other modes. As the pump power is increased, TLSs are saturated across a wider frequency span, reducing losses in nearby modes. This is illustrated in Fig. 3.9a.

The full probe response as a function of detuning and pump power is shown in Fig. 3.10. The loss due to TLS is plotted in Fig. 3.10a and a fit to eq. 3.3 is shown in Fig. 3.10c. For pump phonon numbers $n > n_s$ the losses in the pumped mode are completely saturated and no additional effects of increased pump power can be resolved. The shape of the spectral hole, however, depends strongly on power in the entire range accessible in this experiment. The spectral hole due to the pump continues to widen as the pump power is increased even though pump mode losses are completely saturated. On the contrary, holes in the absorption spectrum burnt using pump phonon numbers below n_s are not well resolved by the free spectral range of the resonator. Fig. 3.10b shows the measured frequency shifts, and the fit to eq. 3.2 is plotted in Fig. 3.10d. We observe that unlike the

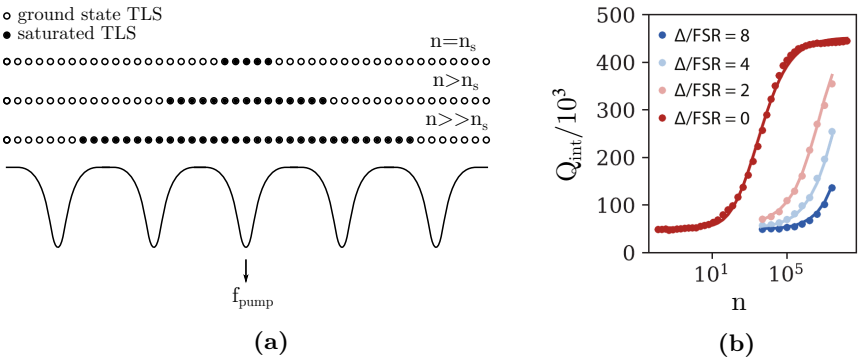

Figure 3.9: a) Illustration of TLS saturation due to the pump. Near resonant TLSs in the ground state can be excited by the SAW field and induce loss. Saturated TLSs do not contribute to loss. At the single mode saturation phonon number n_s, TLS loss is mitigated in the pump mode, while losses in other modes are nearly unaffected. As the strength of the pump tone is increased, the spectrum of the saturated TLSs becomes wider, reducing loss substantially in nearby modes. b) Internal Q-factor as a function of phonon number for the pump mode (red dots). It is the same graph as in 3.8c complemented with three probe modes below the pump. The pump-probe detunings are indicated and fits are shown as solid lines. The loss saturation in the detuned probe modes is fitted with eq. 3.3

loss saturation, the frequency shift is not monotonous in power for a given detuning Δ. This is consistent with the model of the dispersive interaction between off-resonant TLSs and the SAW modes.

Our measurements revealed the shape of the spectral hole burnt in a TLS ensemble by a strong pump. We have shown that the response in acoustic susceptibility due to pumping is qualitatively well captured by theory based on the STM [71]. Furthermore, our results suggest using acoustic pumping to mitigate TLS loss in superconducting qubits. While improvements in design and fabrication methods have led to a rapid increase in coherence in recent years, active means of TLS saturation have not been developed due to the incompatibility of microwave pump fields

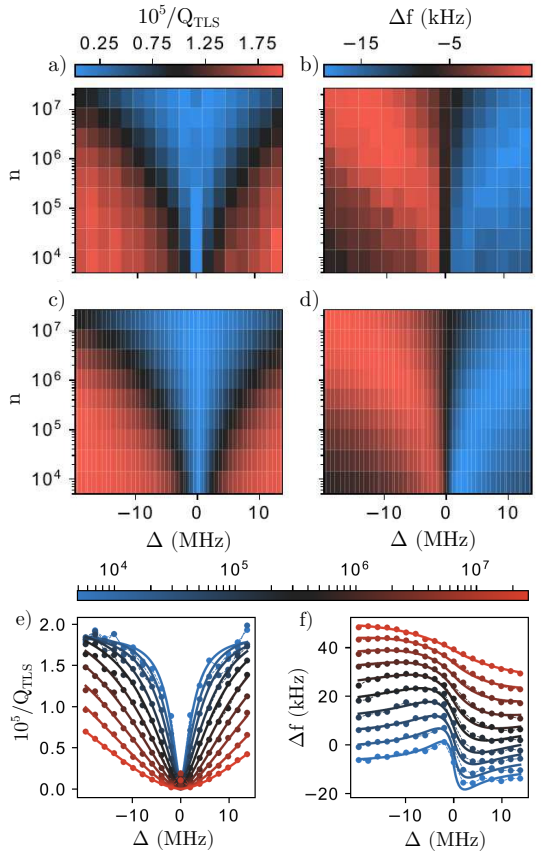

Figure 3.10: Two-tone spectroscopy of the TLS ensemble. A drive tone is applied at the pump mode and response in the other modes are measured as a function of detuning Δ and the number of pump phonons n. The TLS loss $1/Q_{TLS}$ is shown in a). In c) we show the fit to eq. 3.3. The pump also induces a frequency shift in the probe mode, plotted in b), with a fit to eq. 3.2 shown in d). e) shows the loss data as dots with fits to eq. 3.3 (solid lines), with the color scale indicating the pump phonon number. The corresponding plot for the frequency shift is shown in f) with a 5 kHz offset between traces. The frequency resolution in Δ in the measurement is exactly the free spectral range of the resonator.

with device functionality. This limitation does not necessarily apply to the acoustic pumping scheme demonstrated here. For a spectral hole due to an applied SAW drive, it is straightforward to reach a linewidth of several tens of MHz, which allows for pumping at sufficient detuning to prevent spurious excitations due to crosstalk, but still within range of the spectral hole. The generation of high-frequency SAW on non-piezoelectric substrates, including silicon, is well established [77] and could be integrated with superconducting quantum information processing devices. Acoustic resonators also have a lower intrinsic sensitivity to temperature than superconducting devices, which should make them well suited for studying the temperature dependence of TLS-induced noise and dissipation across a wide temperature range.

3.5 2D coupled cavities

The achievement of the tunability of the devices was a milestone for our project. Moreover, in the collaboration with Chalmers, apart from investigating a new regime of application (very low temperature) we also probed a different configuration of cavity by using the one-port IDT device. Having exploiting these different possibilities for the one-dimensional arrangement of the cavities, it was only natural to try to push forward for a two-dimensional expanded version of the our coupled scheme. Concerning this, we know that much of the investigation with SAW in two dimensions is done with a class of structures know as phononic crystals (PCs), which have attracted a great deal of attention lately. They are usually defined as artificial materials made of periodic arrangement of scatterers embedded in a matrix, enabling the control of the propagation of elastic waves. The term “artificial” means periodic material system that were made by technology or craft. It is used to differentiate them from natural crystals. The periodicity is measured by a length, the lattice constant, that is much

larger than the interatomic distances in natural crystals, being the elastic waves considered the asymptotic limit of acoustic phonons. Investigation on PCs goes back to 1993 [78], in an analogy to the concept of photonic crystals for light and since then it has drawn a lot of interest. The growing interest in this periodic structures is connected to their peculiar properties, such as anomalous dispersion (negative refraction) [79], occurrence of band-gaps [78] and near zero group velocity [80]. Very recently, they were also used to enhance sensing capabilities [81]. When the periodicity of a PC is broken, it is possible to create highly localized defects within the acoustic band gap, in analogy to localized modes in photonic crystals, as already mentioned, a concept which itself was inpired by localized impurity states in semiconductors (coming from the theory of electrons in crystal lattices). Extended defects such as rows of different inclusions in the phononic lattice have been shown to be efficient wave guides [82]. Defect modes can then lead to functionalities such as filtering and multiplexing [83] and sensing [84]. Using negative-index PCs, flat superlenses able to focus elastic waves with a resolution lower than the diffraction limit have been realized [85, 86]. The coupled-resonator scheme have been used for guiding and the bending of acoustic waves in highly confined waveguides [87, 88]. Very recently, Jiang et al. [89] proposed a laminated pillar-based PC on a semi-infinite ZnO substrate used to investigate the effects of the physical parameters on dispersive characteristics of SAW. Wang et al. [90] investigated experimentally Lamb-wave propagation in coupled-resonator elastic waveguides formed by a chain of cavities in a two-dimensional phononic crystal slab with cross holes. The same group investigated experimentally chains of evanescently coupled microresonators forming phononic polymers [91] that could find applications in ultrasonic sensing, for implementation in topological phononics, and for the design of optomechanical resonator chains. Delfino et al. [92] engineered a coupled resonant acoustic waveguide to manipulate the propagation of ultrasonic

waves for wavelength division multiplexing.

Motivated by this effervescent topic of research and the great effort made to achieve PCs of good quality and of predictable behavior we set off to pursue the design and fabrication of 2D grid structures with coupled defects. We were able to experimentally achieve the simultaneous coupling of cavities in perpendicular directions. The cavities we use are defined by defects in a 2D rectangle grid of rectangular pillars. The requirement for achieving such results was the fine refinement of the simulation tools. Both the 2- and 3-D simulations were needed for designing the structures we will present here. Therefore, before we show the experimental details let us focus on some key simulation results.

We start with the 3D eigenfrequency study model in order to obtain a general sense of the role that each parameter plays in the behavior of the modes. We use a rectangle, and not a square, for both the unit cell and the perturbation because the material used in our experiments is $LiNbO_3$, which is anysotropic. Therefore, for a structure to work in the same frequency range on both perpendicular directions, the λ_{SAW} for each direction will have to be different. More specifically, proportionally different to the difference in the velocity of the SAW in each direction. We use the subscript 'X' to denote the X-direction of the 128°-rotated $LiNbO_3$ and the subscript 'Y' for the perpendicular direction. As v_X=3992 m/s and v_Y=3675 m/s in the following results $\lambda_Y < \lambda_X$. More specifically $\lambda_Y = 0.94\lambda_X$[¶]. The simulation results in Fig. 3.11 and Fig. 3.12 are only for the X-direction because the perpendicular case follows similarly.

As the different modes respond differently to the mass loading effect it is important to see how they behave with the change in height of the perturbation. In Fig. 3.11a we can see the result of the simulation for a

[¶]The chosen difference in λ is not exactly proportional to the difference in velocity for the free surface due to the fact that the introduction of the perturbation affects the wave velocity differently in each direction.

rectangle of gold on top of a $LiNbO_3$ substrate. We varied the height of the pillars while keeping the size of the rectangle fixed. Similarly, we

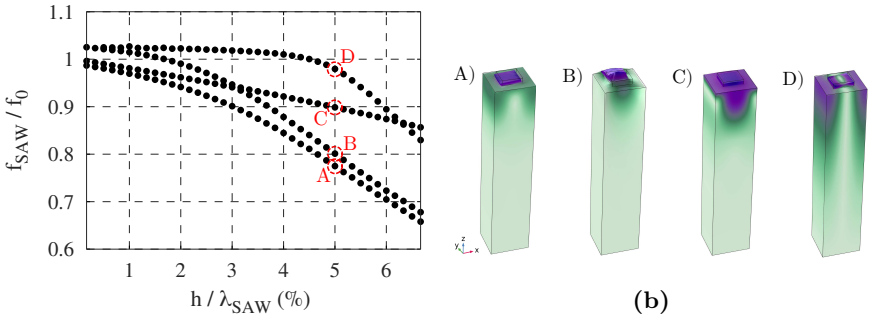

(a) **(b)**

Figure 3.11: a) Sweep value of h for a constant r of 0.5, that is, for a rectangle of size $\lambda/4$. b) Absolute displacemente of modes of Fig. 3.11a, that is, with $h/\lambda = 5\%$.

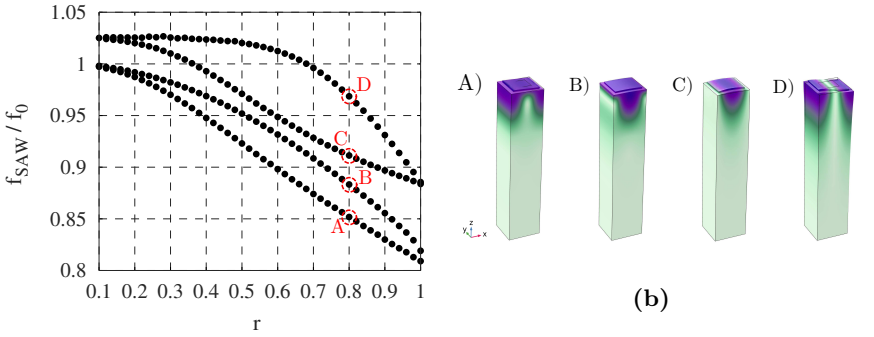

(a) **(b)**

Figure 3.12: a) Sweep value of r for a constant h of 300 nm, that is, $h/\lambda = 2.5\%$. b) Absolute displacement of modes of Fig. 3.12a, that is, with $r = 0.8$.

verified how the modes respond to the change in size of the rectangle,

represented in Fig. 3.12a by the parameter r, being $l_{X,Y} = r\lambda_{X,Y}/2$, where $l_{X(Y)}$ is the side of the rectangle in the $X(Y)$-direction. From these tests we take that the height by wavelength proportion should not exceed 3% in order to avoid the coupling of the Rayleigh mode with a shear one. Also, that a $r > 0.5$ could be used to maximize the distance between Rayleigh eigenmodes which, in turn, results in a wider stop band for the Bragg mirrors.

We also show the dispersion curve for this unit cell. In Fig. 3.13 one can see the band diagram of the out-of-plane polarization in the pillar-based phononic crystal made of gold rectangles on $LiNbO_3$, calculated along high-symmetry directions of the first irreducible Brillouin zone. The solid lines represent the sound line, analogous to the light line in photonic systems, and is the linear dispersion of Rayleigh mode in an homogeneous medium. Coupling to bulk waves (BAWs) occurs for SAWs outside of the sound line, known as the sound cone (shaded area in Fig. 3.13c)).

The shape and size of the optimum perturbation was possible to decide with the fast eigenfrequency study. In order to decide the number of pillars and cavity size we need to use a model of the full device. We start with a 2D model, which gave us a good indication of these parameters. Our aim is to have coupling of two cavities in each direction and, consequently, extended coupling of cavities in both perpendicular directions. For that to work, at least one of the resonant peaks have to be located approximately at the same frequency for both directions.

By testing various simulation parameters we came to a number of strips of 40 for the X-direction and 120 for the Y-direction. On deciding this number one has to take into account that the more perturbations added, more close in frequency the peaks will be. Closer peaks would make it harder to coincide only one peak of each direction. Or, putting in other words, it would make it easier to coincide a given peak of one direction with both the peaks of the perpendicular set of cavities. This would mean

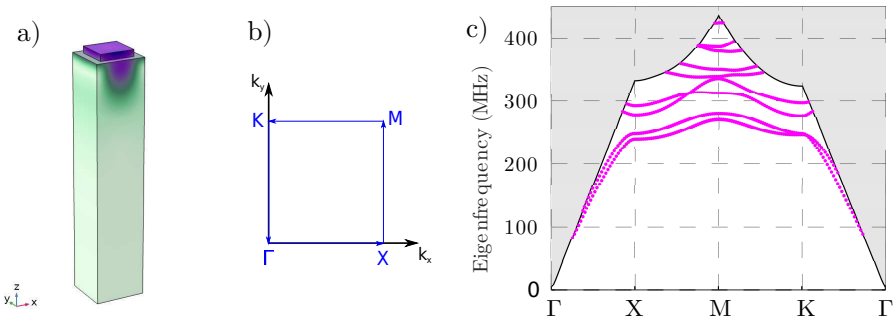

Figure 3.13: a) Unit cell used for calculating the dispersion. b) The first Brillouin zone for the reduced wave vector. c) Band structure along the high-symmetry directions of the first irreducible Brillouin zone generated for a model with $\lambda_X = 12\ \mu m$, $\lambda_Y = 11.28\ \mu m$, $r = 0.7$ and $h = 600\ \mu m$. The dots represent propagating SAW bands within the first Brillouin zone. The solid black line is the sound line, and is the linear dispersion of Rayleigh mode in an homogeneous medium. The shaded area is the sound cone, where coupling to bulk waves can occur.

no selectivity of the mode to excite. Using fewer perturbations, on the other hand, may cause the peaks not to be sufficiently accentuated. That is, the eigenfrequency would not be well defined and the eigenmode would not be excited properly. Regarding the size of the cavity we note that, as it was increased, the resonant peak moved towards higher frequencies. This happens because the velocity of the wave is lower under the gold covered area. As the size of the cavity is increased, the effective velocity of the wave under the whole structure increases, causing the frequency variation. Fig. 3.14a shows this effect. Besides, it is important to realize that the cavity size cannot be chosen arbitrarily. It has to conform to the spacing of the pillars in the grid in both directions. Therefore, the cavity must be simply the removal of a number of rectangles, so that the regular spacing between the pillars in the grid can be maintained. Here

we adopt the convention that, when we say that the size of the cavity is 7, for example, it means that there is a 7 rectangle gap in the matrix grid. We tested several cavity sizes until settling for the ones appearing in Fig. 3.14b. Nonetheless, we stress that the 2D simulations only give us an indication of the parameters to be used. The device is fundamentally different from the ones studied before, which used only strips for the BRs. As the perturbations here are pillars we do not expect to see the kind of agreement between 2D and 3D simulations as we saw in the case of strips (see Fig. 3.2).

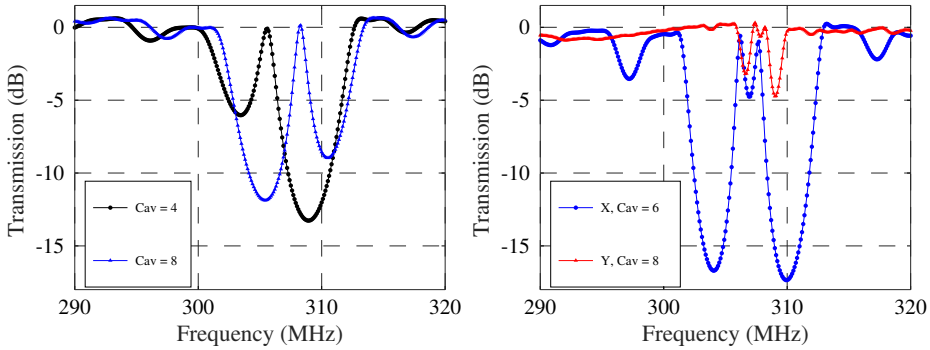

Figure 3.14: a) Transmission for a 2D model simulating a one cavity device with two BRs of 40 strips for a wave traveling in the X-direction. The position of the resulting peak changes according to the size of the cavity. The legend follows our convention that the number corresponds to the number of strips removed from the BR. b) Transmission for a 2D model simulating a two cavity device with three BRs of 40 (100) strips for the X(Y)-direction. For a frequency of approximately 307.5 MHz we would have the excitation of cavities in both directions.

Fig. 3.16a exhibits the calculated transmission for both X and Y directions using a 3D simulation model. Indeed, we use the pseudo 3D model because a complete 3D model would require much more computational

power, as we discussed in the previous chapter. For this reason, although these simulations are surely more realistic than the simple 2D ones, we do not expect them to be in such good agreement with the experiments. Using the 3D model with the applied periodic boundary conditions we are actually simulating a device where the cavities are line defects, not limited in the direction perpendicular to the wave fronts. Therefore, the experimental peaks are expected to be much less prominent than the simulated ones. Following the same reasoning, the experimental dips will be more pronounced, due to the greater number of pillars in the path of the waves which contribute for a higher overall reflection. Being aware of these limitations we designed the devices considering the optimum simulation results - 40 (120) rectangle pillars BRs with cavity size of 7(9) for the X(Y)-direction - and added some structures with variations on the size of the cavities.

The measurements were carried out using a two-port device composed of IDTs with 5 pairs of split-fingers, where $\lambda_X = 12$ μm and $\lambda_Y = 11.28$ μm, meaning that fingers of pitch $p_X = 1.5\mu$m and $p_Y = 1.42$ μm were used. The micrograph in Fig. 3.15a shows some of the structures while in in Fig. 3.15b we see the a 7 by 7 cavity in detail. The size of the gold rectangles are 5.1 μm by 4.8 μm, and they are separated by 0.9 μm by 0.84 μm in the X- and Y-directions, respectively. A peculiarity of this device is that we designed with a 3-pad system, where the central one is used in both excitations, either of the cavities on the bottom (left) half of the structure or upper (right) half, considering the X(Y)-direction.

In Fig. 3.16b we show the transmission in both X and Y directions for a structure composed of cavities of size 7x11. We note that for a frequency of approximately 307.43 MHz we have the excitation of both the second peak in the X-direction and the first peak in the Y-direction. Showing, therefore, the achievement of simultaneous coupling of cavities on both directions.

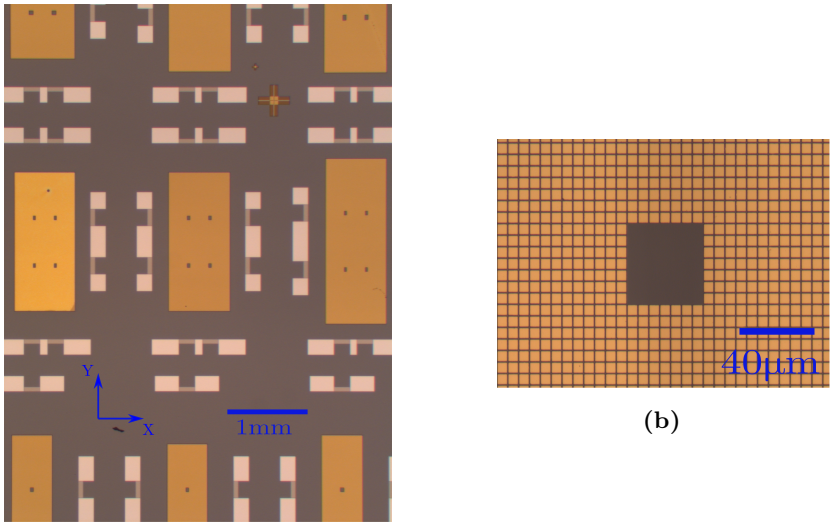

(a) (b)

Figure 3.15: a) Micrograph of the sample where some 2D cavity structures appear. b) Zoom in a cavity of 7x7 size, that is, there are a 7 rectangle gap in the structure in both directions.

To further support our results we have performed interferometry measurements which access the vertical displacement of the sample (as described at the end of the Methods chapter)[‖]. The aim of this kind of experiment is to map the SAW field on the direction normal to the surface sample, giving complementary information to that of the electrical characterization. In Fig. 3.17a we see a sketch of the device where we identify an IDT which was excited by the RF source to generate the waves and the line along which the interferometric scans were performed. For

[‖] These experiments were initially thought to be performed by myself at the Paul-Drude Institute, in Berlin. However, due to COVID-19, I could not travel and the measurements were made by our collaborators there. Nonetheless, we were in close contact, through calls and virtual meetings, during the whole time needed to complete such experiments.

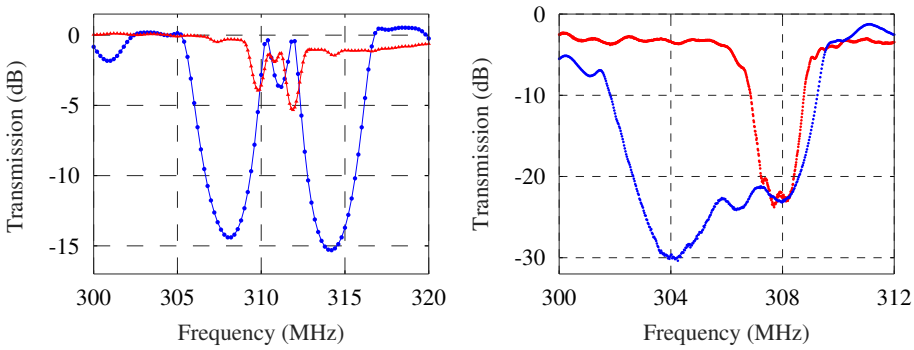

Figure 3.16: Blue (red) markers are for the X(Y)-direction. a) Pseudo 3D simulation result. We calculate the transmission for each direction. For the X-direction we include two cavities of size 7 located between three sets of 40 pillars of 120 nm height. For the Y-direction, the cavities are of size 9 and we use 120 pillars for each BR. (b) Measured transmission for each direction, minus the respective delay line. This sample is composed of a matrix of 40x120 pillars and cavities of size 7x11. At around 307.4 MHz we identify both the second peak for the X-direction and the first peak for the Y-direction, which verifies the coupling in two dimensions.

the X direction, the vertical surface displacement along line A was probed while the sketched IDT was excited. For the Y direction, line B was scanned while the excitation was applied to the IDT on the top right. That is, the measurements in both cases are done parallel to the wave fronts, moving away from the excited IDT and scanning a line passing through the area where the cavities are located. Fig. 3.17b shows a diagram of the experiment where δz represents the vertical displacement accessed and δm represents the moving of the mirror which is used to optimize the interference pattern. For a detailed scheme and account of the measurement setup please refer to the end of the Methods chapter (Fig. 2.13).

We stress the fact that these interferometric measurements only probe

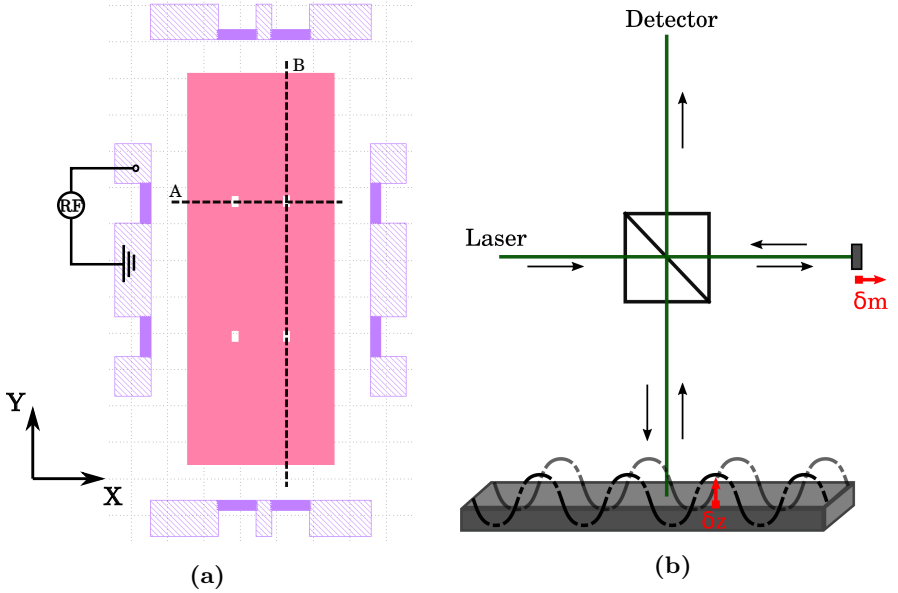

Figure 3.17: a) Sketch of the device and the lines along which each of the interferometric scans was performed. Along line A for the X direction, with sketched IDT excited. Along line B for the Y direction, with the source now moved to the top right IDT. b) A schematic of the interferometer. Interference of the laser light due to different paths length is measured by the detector. δz represents the vertical displacement accessed and δm represents the moving of the mirror which is used to optimize the interference pattern. For a detailed scheme and account of the measurement setup please refer to the end of the Methods chapter (Fig. 2.13).

the vertical surface displacement and not the horizontal motion which always accompanies the Rayleigh SAW. Besides, what is measured is a signal proportional to the vertical surface displacement at a specific phase. Therefore, what it gives us is an instant picture of the standing wave formed along the structure. All constrains considered, the interferometer provides valuable information regarding the behavior of the whole device according to the frequency excitation applied. As it was discussed at the

end of the Introduction, this sort of technique grants a reliable picture of the *envelope* of the standing wave (see Fig. 1.8 and discussion of it). In particular, in identifying the nodes of the standing waves, which are independent of the particular phase being recorded.

Fig. 3.18 shows the result of a scan along the X direction where the IDT was excited with frequencies going from 303 MHz to 309 MHz in steps of 0.5 MHz. The scan starts at approximately 100 μm before the grid, so that position zero marks its beginning. Vertical purple dots mark the start and the end of the grid while the black ones mark the start and end of the two cavities. Within the expected stopband one can identify some small ranges where the activation of the cavities are more intense. These regions are connected to the resonances which appear in the transmission spectrum, being a visual representation of the different interplay between cavities, according to the applied excitation. This demonstrate one of the interesting features of this type of device which is the selective activation of different surface regions.

For comparison, some single frequency scans were also done for a control structure which is composed of the same rectangular grid as the typical device, but with no defects in it, i. e., it holds no cavities. As can be seen in Fig. 3.19, within the stopbands of each direction, we can only see the amplitude of displacement decreasing as we move away from the IDT. A simple effect of the reflection capability of the Bragg mirror. Focus now on Fig. 3.20, which shows two different profiles measured along the X direction. For 306.7 MHz a decrease in amplitude can be observed around the area of the first cavity (on the left) while the second cavity concentrates most of the energy enclosed by the structure. Whereas, for 307.7 MHz, most of the energy is concentrated on the first half of the path probed. The energy confinement observed is not so extreme due to the fact that the quality factor of the cavities is not very high. This is a constraint on our design due to the pursuit of the coupling between them. Still, and as a consequence, a

rich interplay between cavities is clearly appreciated. The same holds true for the measurements along the Y direction. Fig. 3.21 is the equivalent of the figure we have just discussed. For two different frequency excitation within the stopband a very distinct picture is observed. Due to the longer BR, bigger distance between cavities and smaller coupling factor for this direction, the wave attenuation decreases the interplay among cavities. Nonetheless, one can easily recognize that the behavior in 3.21a does not follow the simple attenuation seen in 3.19b, although both are for the same frequency. And, for 3.21b, an anti-node can be identified before the first cavity, which concentrates most of the energy accumulated on the structure.** The graphs mentioned in this paragraph are equivalent to single frequency selected profiles of Fig. 3.18. However, they are really new measurements which were performed for single frequency excitation, where a extended integration time was implemented for each collected point along the way. Therefore, they are a more clear and reliable measure of the reflectivity (as can be appreciated in the scale of the displacement), although more time consuming.

In essence, these measurements reveal some of the nuances on the coupling between the cavities for each direction. Furthermore, as an interplay between them can occur for the exact same frequency excitation, we note that what was achieved in such devices is a two dimensional coupling. In order to better perceive this mentioned transverse coupling directly we devised a final measurement. It consists of applying the RF source to the X direction (as in the Fig. 3.17a) and probe the transmission with one of the IDTs designed for the Y direction, that is, out of the path of the generated waves and positioned 90 degrees in respect to the first IDT. With this configuration we are in position to see how the coupling in one direction can affect the perpendicular one. Fig. 3.22 exhibits our findings.

**All of the measurements displayed in this section are normalized according to a reference signal to account for the different reflectivity of the metal-coated and metal-free areas.

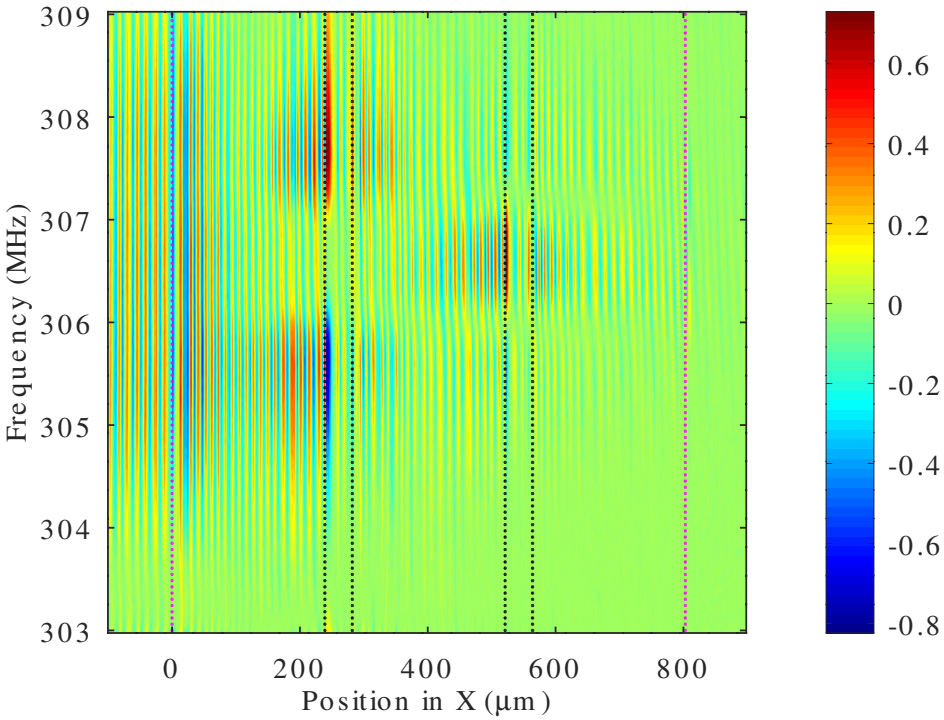

Figure 3.18: Vertical displacement (in arbitrary units) for a line scan along the X direction for a range of frequencies around the stopband. Vertical purple dots mark the start and the end of the grid while the vertical black dots mark the two cavities. Some small ranges of higher activity between cavities can be recognized, demonstrating the selective activation of the different regions on this device.

Here, looking at the time domain, we note a peak in the transmission for the structure with cavities which is not present in the control device. The time in which the referred peak appears matches the time one would expect for the wave to propagate following a path between both IDTs with a 90 degree curve on the area where the cavity between them is located.

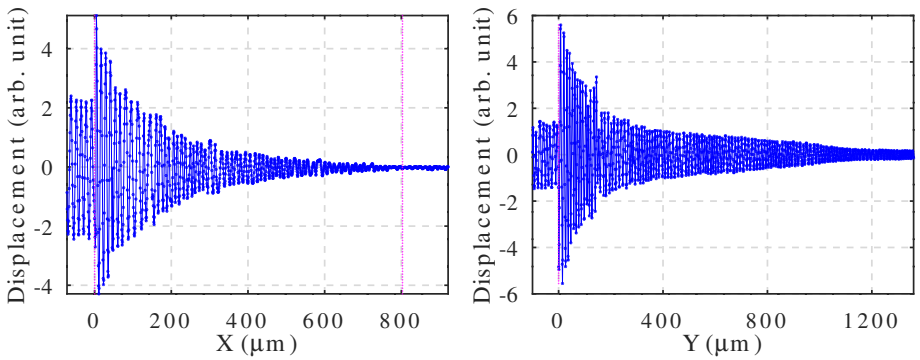

Figure 3.19: Measured spacial profiles for the vertical displacement along the X, in a), and Y, in b), directions for the control device (same rectangular grid but no defects, i. e., no cavities). For frequencies within the stopband the wave is mostly reflected, decreasing its amplitude of vibration along the path. Due to the extended length of the grid in the Y direction, the measurement in b) was not done until the end of the grid as the one exhibited in a). This is why we do not see the amplitude decreasing as much.

Due to the very low level of the signal measured there was no possibility of measuring it with the interferometer tools. As the signal reaching the second IDT (out of the path of the waves and rotated by 90 degrees) is loosely two orders of magnitude lower than the one for the straight transmission, the generated vibration is estimated to be in the order of pm (considering the fact that the vibrations usually are of the order of Å). Nonetheless, the peak in time which is observed is the signature of the transverse coupling. This means that our design configuration remarkably allows for the control of the acoustic field outside of the path of the generated waves. A direct way one could use to try to increase this effect would be to bring all cavities more closely together in space, by using fewer perturbations for each BR. This, however, would bring the resonant peaks closer together, decreasing its distinguishability, a feature especially

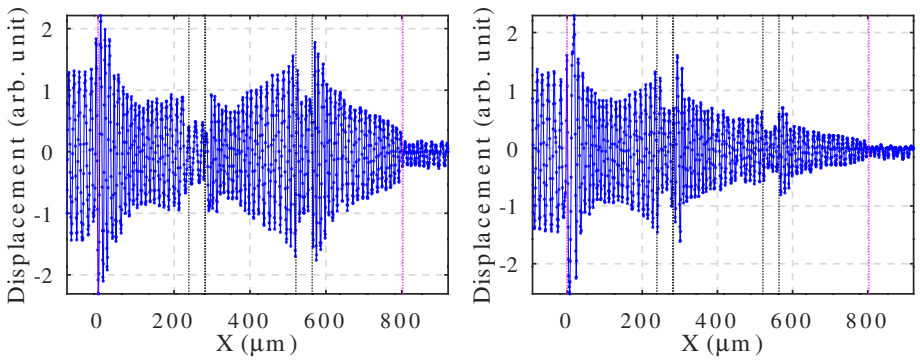

Figure 3.20: Measured spacial profiles for the vertical displacement along the X direction for a device with two cavities. a) and b) are for the frequencies 306.7 and 307.7 MHz, respectively. For the control device the wave simply decreases its amplitude of vibration along the path. Here, however, we see the interplay between cavities.

limiting already for the Y direction (resonances are spaced by 0.5 MHz, approximately). One manner to guarantee that the peaks are satisfactorily apart would be to design the devices for higher frequencies or, equivalently, to increase the reflectivity of each individual structure composing the BRs (in our case, rectangles of 120 nm height). Additionally, such a strategy would, of course, make the devices close packed.

In summary, our results show the coupling of SAW cavities defined by defects in a two-dimensional pillar based phononic crystal structure. SAW can be excited and coupled, with the same frequency excitation, in two perpendicular directions on the surface of an anisotropic material. We have demonstrated that, through our coupled 2D scheme, we can control the acoustic field distribution outside of the path of the traveling wave, traditionally restricted to the area defined between the IDTs. The advances shown here could be used to construct more complicated designs

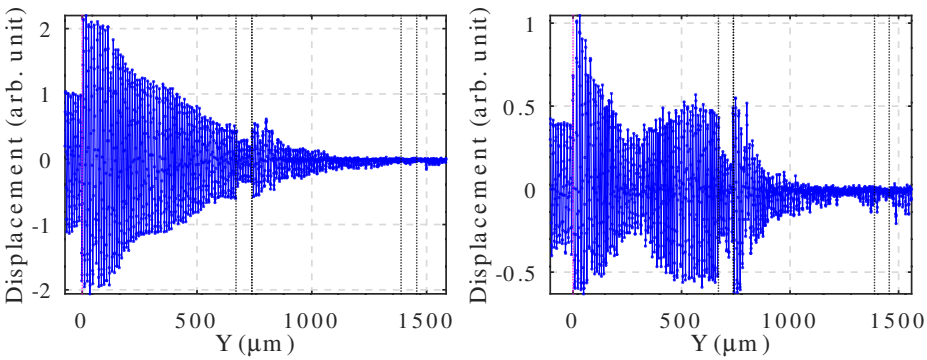

Figure 3.21: Measured spacial profiles for the vertical displacement along the Y direction for a device with two cavities. a) and b) are for the frequencies 307.4 and 308.0 MHz, respectively. For the control device the wave is simply reflected, decreasing its amplitude of vibration along the path. Here, we see again the interplay between cavities. Again, we stress that in the Y direction, due to the extendend size of the grid, the measurements were not performed until its end.

for phononic circuits for SAW-based devices. Functionalities such as waveguiding and enhanced sensing capabilities could also be explored. Moreover, relying on a PC structure, it has an additional benefit of reducing the physical length required for a given delay as compared to the traditional gratings with hundreds of metal strips. Such developments surely could not be reached without the highly predictive finite element simulation model developed by us which was used for designing our devices. Very good agreement between simulation and experiment was achieved with it.

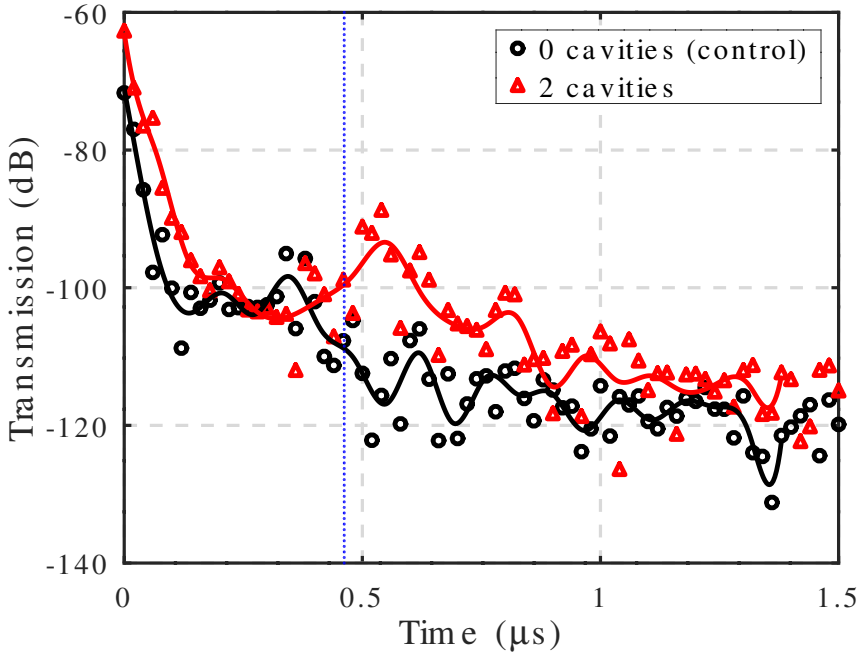

Figure 3.22: Measured transverse transmission, in the time domain, for the IDTs rotated 90 degrees in respect to one another. That is, an IDT for the X direction and an IDT for the Y direction were used, instead of the usual measurement of IDTs facing each other. The vertical line marks the expect time for the signal to reach the receiving IDT. Agreeing with this expectation, we note a peak for the signal from the structure with cavities that is 20 dB higher than the control one.

4

Conclusion

In this thesis we have investigated how carefully designed structures can be used to control the acoustic field on the surface of a piezoelectric material. We have developed simulation models based on the finite element method to predict the behavior and to design SAW devices, which were then fabricated and measured. With it, we showed that our models have a good predictive power and that our devices exhibit a high degree of control of the waves traveling along the path of the designed structures.

Regarding the advances made in the modeling, we started by building a 2D simulation model that replicates the saggital plane of the devices. The model agreed very well with the experimental results of earlier investigations on SAW devices. Also, we did a simpler model, simulating a 2D unit cell, which we used for faster calculations. This unit cell, of one wavelength width and with applied periodic boundary condition, forced all physical quantities to be the same at the boundaries, emulating an infinite substrate where the parameters of perturbations can be tested. With it, we clarified the nuances between using floating versus shorted configurations, as well as how the size of the perturbations affected the acoustic eigenmodes.

We then proceed to build a similar unit cell, now in 3D, enabling us to rapidly calculate not only the effects of the changes in isolated parameters,

such as the size of the strips and pillars, but also the whole band structure along the high-symmetry directions of the material. These computations were crucial for choosing the parameters to be used in the more time-consuming, whole device pseudo 3D simulations. The pseudo 3D model, emulated the sagittal plane cut but with a significant difference: a half wavelength width was introduced in the perpendicular direction of the geometry, allowing the model to vibrate in that direction as well. This was also contrasted with earlier experimental results, proofing the robustness of our calculations. The 3D model was imperative as a final step before deciding the designs for the fabrication of the devices.

With respect to the experimental achievements, firstly we have accomplished the tuning of the response of the SAW cavities. The thermal response of the substrate served as a tool for controlling the acoustic field. This was carried out by applying a voltage to the end of the metal strips which connects the end of the strips of the BRs. The resistive heating of the metal grid warmed up the sample, which in turn changed the parameters of the material causing a frequency shift. This allowed us to demonstrate a continuous, memoryless and dynamical tunable device.

Secondly, in a successful collaboration with our network partners from the Chalmers University of Technology we have shown a way to mitigate losses in resonators at very low temperature. We have made measurements which revealed the shape of the spectral hole burnt in a TLS ensemble. This was accomplished by a two-tone spectroscopy scheme. The scheme consisted in inspecting one resonance (the drive tone) of a multi-mode SAW resonator while sweeping the power in a neighboring mode (the pump tone) and monitoring the change in Q-factor and resonance frequency of the mode under inspection. We have shown that the response in acoustic susceptibility due to pumping is qualitatively well captured by the theory based on the STM. Our results suggest using acoustic pumping to mitigate TLS loss in superconducting qubits.

Finally, we have extended some of the earlier results on coupling SAW cavities to the two dimensional realm. Our results showed the coupling of SAW cavities defined by defects in a two-dimensional pillar based phononic crystal structure. The design we used enabled SAW to be excited and coupled, with the same frequency excitation, in two perpendicular directions on the surface of an anisotropic material.

4.1 Outlook

Concerning the tuning of the devices, one idea for improvement is designing devices to operate at higher frequencies. This would concentrate the energy of the waves closer to the surface where the heating is taken place, increasing the effect. Also, more extended structures could be used, covering more of the area where the waves travel. A different approach which could be explored for tuning the devices without using heat is to use a 2D material for connecting the strips of the BRs instead of another metal strip, as used here. By using graphene, for example, one could change the configuration of the BRs on the go by controlling a bias applied voltage. Or, perhaps by the use of another family of 2D materials, transition metal dichalcogenides such as WSe_2, WS_2 and $MoSe_2$, whose conductive properties can be modified by the light of an excitation laser. That way, maybe the switching could be done in a reduced time scale.

On what concerns the inspection of the TLS ensemble we have already pointed out that the acoustic resonators are a more robust platform than superconducting devices for studying temperature dependence of TLS-induced noise. Moreover, our results are clear evidence, due to the verified agreement with STM theory, that the TLS loss for SAW waves behave in a similar fashion to that of microwave resonators, which is a very useful information for the engineering of future systems for quantum acoustics with SAWs.

Finally, with respect to the 2D cavities coupling, some possibilities could be explored. The coupling of more cavities would surely open more routes for the control of the acoustic field. The higher selectivity allowed by a multi-cavity structure would grant a (de)multiplexing feature to such device, for example. Furthermore, the rectangular pillars we used are a very simple design. More elaborate patterns could lead to a wider and complete band gap, which would improve the confinement of the acoustic energy within the defects, although fabrication would be cumbersome. Lastly, functionalities such as waveguiding and sensing capacities are regularly explored with this kind of platform.

5

Resumen en castellano

Las ondas acústicas de superficie (SAW, acrónimo en inglés) son modos de propagación de energía elástica a lo largo de la superficie de un sólido cuyas amplitudes de desplazamiento disminuyen exponencialmente a medida que se aleja de dicha superficie. Cuando se propaga en materiales piezoeléctricos, un potencial eléctrico con la misma periodicidad espacial y temporal acompaña a la onda de superficie. La existencia del tipo básico de SAW, en un material isotrópico, fue demostrada por primera vez en 1885 por Lord Rayleigh [1], por lo tanto, la onda a menudo se llama onda de Rayleigh. Esta onda se propaga a lo largo de la superficie plana de un semi-espacio, con el movimiento de partículas en el plano sagital (el plano que contiene la normal a la superficie y la dirección de propagación). Rayleigh estudió señales sísmicas observadas después de un choque en el suelo. Él demostró que un componente tardío, siguiendo las señales esperadas debido a las ondas longitudinales y transversales, podría explicarse por la existencia de una onda superficial más lenta. La señal también podría ser relativamente fuerte debido a que la onda se extiende en dos dimensiones en lugar de tres. Posteriormente, hubo un gran número de trabajos de otros geofísicos con intereses sísmicos. En un tratado publicado en 1911 [2], Love estudió las ondas superficiales de cizalla, cuyo movimiento es perpendicular al

plano sagital. Esta llamada onda de Love, puede existir cuando un semi-espacio está cubierto con una capa de material con una velocidad más baja de onda cizalla de volúmen. Love también mostró que una onda de tipo Rayleigh podría existir en un sistema de varias capas. El trabajo a respecto de la onda de Rayleigh en sustratos de varias capas en el Instituto de Investigación de Terremotos, en Tokio, en la década de 1920 [3] mostró que podría existir una serie de modos superiores además del fundamental, siendo el primero de estos modos superiores, conocido como onda de Sezawa. Aunque hayan venido de estudios sobre terremotos, las ondas de Rayleigh, Love y Sezawa se han utilizado en dispositivos SAW modernos.

El interés en SAW para aplicaciones en electrónica surgió de los requisitos de mejora de radar a fines de la década de 1950. La primera sugerencia para usar transductores SAW planos fue hecha independientemente por Rowen y Mortley en dos patentes en 1963 [4, 5]. Su motivación era simplificar el comportamiento y la fabricación de los dispositivos tradicionales de retraso de señales utilizados para la compresión de pulso (un requisito para mejorar la capacidad de rango de los radares en ese momento). La primera realización experimental de estas estructuras planas fue realizada por White y Voltmer en 1965 [6]. Ellos introdujeron el transductor interdigital uniforme (IDT, del inglés *interdigital transducer*), un dispositivo utilizado para generar y recibir las ondas en un sustrato piezoeléctrico, para acoplar campos eléctricos a campos elásticos. Para comportarse como un semi-espacio, el sustrato solo necesita tener unas pocas longitudes de onda de grosor porque la onda tiene una profundidad de penetración pequeña.

En las últimas dos décadas, ondas acústicas de superficie (SAW) propagándose en estructuras periódicas han atraído mucha atención y han sido la base de un gran número de investigaciones. Marcadores SAW, por ejemplo, explotan la posibilidad de usar dispositivos activos o pasivos para codificar información y usarla en muchas aplicaciones,

desde el control de tráfico, hasta seguridad o identificación de partes en cintas transportadoras. Diseños muy similares son utilizados en sensores, especialmente de temperatura y masa. Asimismo, una miríada de avances científicos han sido hechos en el estudio de cristales fonónicos (PCs, del inglés *phononic crystals*). Estos, generalmente se definen como materiales artificiales hechos de una disposición periódica de dispersores incrustados en una matriz, lo que permite el control de la propagación de ondas elásticas. El término "artificial" significa un sistema de material periódico que fue hecho por tecnología o artesanía y se utiliza para diferenciarlos de los cristales naturales. La periodicidad se mide por una longitud, la constante de red, que es mucho más grande que las distancias interatómicas en cristales naturales, siendo las ondas elásticas consideradas el límite asintótico de los fonones acústicos. La investigación en PCs se remonta a 1993 [78], en una analogía con el concepto de cristales fotónicos para la luz y desde entonces ha despertado mucho interés. El creciente interés en estas estructuras periódicas está relacionado con sus propiedades peculiares, como la dispersión anómala (refracción negativa) [79], la aparición de banda proibida [78] y velocidad de grupo casi cero [80]. Muy recientemente, también se usaron para mejorar las capacidades de detección [81]. Cuando se rompe la periodicidad de una PCs, es posible crear defectos altamente localizados dentro del intervalo de banda acústica, en analogía con los modos localizados en cristales fotónicos, como ya se mencionó, un concepto que fue inspirado por estados de impurezas localizados en semiconductores (concepto que vinó de la teoría de los electrones en redes cristalinas). Se ha demostrado que los defectos extendidos, a lo largo de las filas modificadas en la red fonónica, son guías de onda eficientes[82]. Los modos de defectos pueden conducir a funcionalidades como las de filtrar y la multiplexación [83] y de detección [84] también. Utilizando PCs de índice negativo, se han realizado superlentes planas capaces de enfocar ondas elásticas con una resolución inferior al límite de difracción [85, 86].

El esquema de resonador acoplado se ha utilizado para guiar y doblar ondas acústicas en guías de onda altamente confinadas [87, 88]. Muy recientemente, Jiang et al. [89] propusieron un PC basado en pilares laminados en un sustrato de ZnO semi-infinito utilizado para investigar los efectos de los parámetros físicos en las características dispersivas de SAW. Wang et al. [90] investigaron experimentalmente la propagación de ondas de Lamb en guías de ondas elásticas de resonador acoplado formadas por una cadena de cavidades en una losa de cristal fonónico bidimensional con agujeros transversales. El mismo grupo investigó experimentalmente las cadenas de microresonadores acoplados de forma evanescente que forman polímeros fonónicos [91] que podrían encontrar aplicaciones en la detección ultrasónica, para la implementación en topologia de fonones y para el diseño de cadenas de resonancia optomecánica. Delfino et al. [92] diseñaron una guía de onda acústica resonante acoplada para manipular la propagación de ondas ultrasónicas para la multiplexación por división de longitud de onda. La mayoría de los estudios de PCs están enfocados en la propagación de ondas elásticas o ondas acústicas de volumen. Sin embargo, dichas ondas generalmente se generan fuera de la muestra de interés. SAWs, por otro lado, pueden ser excitadas convenientemente en la superficie de un sólido piezoeléctrico.

El efecto piezoeléctrico es un fenómeno físico que se describe en términos de ecuaciones diferenciales parciales (PDE, *partial diferential equations* en inglés). Sin embargo, para la mayoría de las geometrías y situaciones prácticas, estas PDE no pueden resolverse analíticamente. En cambio, se puede construir una aproximación de las ecuaciones, basada en diferentes tipos de discretizaciones. Estos métodos de discretización se aproximan a las PDE con ecuaciones de modelos numéricos, que pueden resolverse utilizando métodos numéricos. El método de elementos finitos (FEM, del inglés *finite element method*) es una de las técnicas numéricas más prominentes utilizadas para realizar tales aproximaciones.

Históricamente, se dice que el FEM tiene su origen en el *Introducción al análisis del infinito* (1748), de Leonhard Euler [12], que sienta las bases del análisis matemático. Sin embargo, los primeros artículos matemáticos sobre FEM se pueden encontrar en los trabajos de Schellbach [13], en 1851, y Courant [14], en 1943. Los desarrollos modernos comenzaron a mediados de la década de 1950, siendo independientemente desarrollados por ingenieros para abordar problemas relacionados con la ingeniería aeroespacial y civil en análisis de estrés, flujo de fluidos, transferencia de calor y otras áreas. El primer libro sobre el tema, por Zienkiewiczand Chung [15], fue publicado en 1967.

Se han propuesto varios métodos fenomenológicos para modelar y análisis de ondas acústicas. Estos incluyen el acoplamiento de modos (COM), modelo de matriz P, modelos de circuitos equivalentes y angulares modelo de espectro de ondas. La comparación de estos modelos muestra que, si se usa correctamente y con parámetros precisos, se obtienen resultados casi idénticos obtenido con todos ellos. Para el caso de una sierra clásica tipo Rayleigh en sustrato de cuarzo, con interacciones débiles y banda de frecuencia estrecha, todos los modelos dan excelentes resultados. Por otro lado, todos los modelos proporcionan solo descripciones satisfactorias de dispositivos que emplean ondas transversales superficiales (STW) y ondas acústicas superficiales con fugas (LSAW). Como son fenomenológicos, su función depende fundamentalmente de ciertos parámetros explícitos, que deben conocerse con gran precisión. Los parámetros se pueden lograr de varias formas: directamente, por ejemplo, mediante láser técnicas de sonda, indirectamente trazando uno de los modelos citados a mediciones de dispositivos o estructuras de prueba, o teóricamente de analíticas teorías de perturbación o simulaciones numéricas más rigurosas. Entre estos, se dice que las mediciones eléctricas de estructuras de prueba especialmente diseñadas ser el método más confiable. Y es precisamente la respuesta eléctrica la que suele ser de gran interés en los dispositivos SAW.

Desafortunadamente, experimental La extracción de parámetros es costosa y requiere mucho tiempo, ya que Los parámetros deben determinarse individualmente para cada sustrato con cada material, tamaño, forma y estructura de los electrodos. Además, incertidumbres en las propiedades y la geometría de los electrodos debido a la tecnología de fabricación limita la precisión de los resultados obtenidos. Como dice Plessky, en relación con el modelo COM: Como descripción general simplificada de ondas de diferente naturaleza física en medios periódicos el modelo se utilizará siempre, pero para un diseño exacto La tendencia será utilizar los métodos numéricos FEM, al menos parala determinación de los parámetros COM. Hay algunas desventajas en el uso de FEM [19]. Por ejemplo, la solución nunca está en una forma cerrada, que no permite el examen de una respuesta del sistema a un cambio en un determinado parámetro. Además, existen errores inherentes: la verdadera geometría se simplifica; la cantidad de campo siempre se supone que es un polinomio sobre un determinado elemento; y el uso de técnicas de integración muy simples, como la cuadratura de Gauss. Y finalmente, hay errores computacionales inherentes como el número finito de dígitos ($\pi = 3.14159265$, por ejemplo). No obstante, las ventajas son enormes: puede manejar geometrías muy complejas, condiciones de contorno y carga (dependiendo del tiempo o la frecuencia) en una amplia variedad de problemas físicos.

Cuando se trata de FEM, generalmente muchas matemáticas están involucradas en la decisión de elegir funciones de interpolación, lo que requiere conocimiento de espacios funcionales (como Hilbert y Sobolev), y también se deben realizar muchas pruebas para decidir que tipo de solucionador usar y el abordaje numérico. Afortunadamente, hoy en día, hay una gran cantidad de software comercial disponible que proporciona al usuario instrucciones sobre los mejores modelos para cada problema relacionado con la física que uno quiere resolver. En nuestro caso, utilizamos la plataforma de software COMSOL Mutiphysics [20] con su sistema CAD

3D incorporado, así como su solucionador integrado. Como veremos a continuación, algunas simulaciones muy rápidas pueden ser útiles para proporcionar información invaluable sobre el posible diseño de dispositivos. Además, encontramos que las simulaciones en 2 y 3-D, a pesar de consumir mucho tiempo, dan resultados precisos para situaciones muy distintas. Las simulaciones se ejecutaron en una computadora personal de escritorio con procesador Linux (Ubuntu) 3.40 GHz de 64 bits y 16 GB de RAM.

Con el adecuado desarrollo de modelos de simulación y con base en resultados anteriores, donde el acoplamiento entre varias cavidades se logró en una formación unidimensional, pudimos lograr dos resultados experimentales claves. Primero, el ajuste dinámico de cavidades en una dimensión. Esto se logró aplicando un voltaje de CC a los extremos de la red metálica de los BRs en cortocircuito de algunas estructuras. La corriente eléctrica a través del metal provoca un aumento de la temperatura debido al calentamiento resistivo, lo que cambia la respuesta de frecuencia del dispositivo. Este efecto se utilizó para lograr una variación de frecuencia de hasta 0.3 %, que se puede utilizar para controlar la transmisión acústica a través de la estructura. En la Fig. 5.1a uno puede ver el cambio de frecuencia en el espectro de transmisión del dispositivo con tres cavidades para $V_S = 3\ V$ en comparación con la respuesta sin voltage aplicada. Luego procedemos a inspeccionar la escala de tiempo de este proceso. Para eso aplicamos un voltaje cuadrado del ciclo de trabajo del 50%, modulado de 0 V a 3 V. Inspectando cómo cambia la transmisión para una frecuencia específica (medición de intervalo cero), la adquisición de datos fue lo suficientemente rápida para para sondear el turno. Al ajustar un exponencial decaimiento $s_{12} = aexp(t/\tau)$ donde s_{12} es la transmisión, a es una constante y τ se relaciona con la escala de tiempo del proceso y el promedio de varios ciclos encontramos $\tau_c \approx 220$ ms y $\tau_h \approx 160$ ms, donde los subíndices c y h están relacionados con las fases de enfriamiento y calentamiento, respectivamente. Además, también hemos realizado

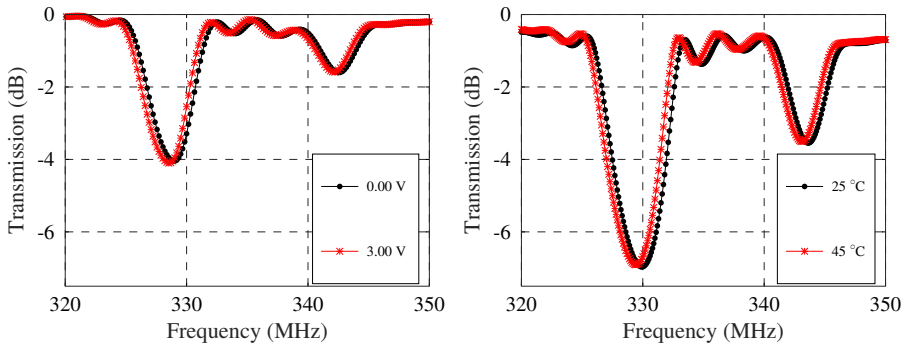

Figure 5.1: a) s_{12} (medido en dB) de la estructura con 3 cavidades. Con el voltage aplicado a la red (simbolos "x") la frecuencia cambia debido al calentamiento del sustrato causado por el calentamiento resistivo de las tiras metalicas. b) s_{12} simulado (en dB) de la estructura con 3 cavidades. El modelo 2D fue usado para simular la propagación acústica a lo largo del plano sagital de la estructura.

simulaciones de elementos finitos del espectro de transmisión de un sistema modelo que exhibe una dependencia de la temperatura consistente con los datos experimentales. Como se puede apreciar en Fig. 5.1b, el formato de la transmisión, la diferencia entre picos y el cambio debido al aumento de la temperatura, que son todos los parámetros físicos relevantes en consideración, están en excelente acuerdo con los experimentos. Estos avances que se muestran aquí permiten un control fácil, continuo y dinámico y podrían aplicarse para una variedad de sustratos. Comparando nuestras simulaciones con los experimentos que hemos demostrado que un aumento plausible de temperatura es compatible con nuestros hallazgos. Sin embargo más efectos pueden ocurrir debido a la aplicación de un potencial eléctrico que también se utilizan como recurso de ajuste. Uno es la electrostricción, que provoca una rigidez piezoeléctrica o también se utiliza para inducir piezoelectricidad en sustratos no piezoeléctricos [49]. Otro es simplemente

la tensión que se deforma el material, alterando la longitud de trayectoria de la onda. No obstante, se acerca que exploran uno o ambos efectos son fundamentalmente diferentes de los nuestros. Utilizan el sustrato como medio capacitivo. La diferencia de voltaje es aplicado entre las superficies superior e inferior o en cada uno de los IDT, es decir, en áreas separadas de la superficie. Debido a las propiedades dieléctricas del sustrato algunos tienen que utilizar voltajes del orden de kV. La tension causado por tal campo eléctrico distribuido a lo largo del sustrato es por eso sus parámetros se cambian. En nuestro caso, sin embargo, el voltaje se aplica entre diferentes puntos de una pieza de metal que se asienta en la superficie. Por tanto, el campo eléctrico aplicado se limita principalmente al metal. Además, algunos exhiben un efecto memoria. Es decir, se ve que el cambio persiste incluso después de que se apague la perturbación. Esto los hace inadecuados para modulaciones dinámicas como las que mostramos aquí. Otros dependen de la señal de sesgo, mientras que el nuestro es insensible a eso. Esto nos llevó a concluir que el efecto observado resulta principalmente de la aumento de la temperatura. Para respaldar aún más nuestra afirmación de que el efecto observado es únicamente térmica hicimos un experimento independiente en el que no se aplicó voltaje. En esta configuración, montamos la oblea encima de una placa caliente y medimos la transmisión a través de la estructura con tres cavidades para diferentes temperaturas, esperando el tiempo adecuado para la estabilización del sistema. Los datos que observamos son consistentes con los resultados anteriores. A modo de comparación, observamos que el mismo cambio de 0.16% que se observó. Cuando se aplicaron 3 V, en este nuevo experimento corresponde a un 10 C por encima de la temperatura ambiente. Este resultado, junto con los argumentos presentado anteriormente, demuestra que estamos ante un simple efecto térmico. Las temperaturas se midieron con un termómetro infrarrojo dirigido a la parte superior de la superficie de la oblea. Según sus especificaciones, desde a una distancia de unos 3 cm,

lee la temperatura de un punto de 2,5 mm de diámetro con una precisión de ± 2 C. Comparando nuestro método con los disponibles en la literatura, vemos algunas mejoras. Como ya se mencionó, los que dependen de la electro- o magnetostricción presentan una curva de histéresis. Acústica eléctrica requieren una fabricación más compleja debido a la estructura de múltiples capas. Y la modulación térmica no menciona la sintonización dinámica.

El segundo resultado clave fue la extensión de este acoplamiento 1D de cavidades para el ámbito 2D, utilizando una red bidimensional compuesta de pilares rectangulares. Es decir, llevamos a cabo el acoplamiento simultáneo de cavidades en direcciones perpendiculares. Dichas cavidades consisten en defectos introducidos propositalmente en la red de pilares. Esto es, la remoción de algunos rectángulos con el intuito de atrapar la energía acústica. Testeando varias combinaciones hemos llegado al número óptimo de 40 perturbaciones en la dirección X y de 120 en la dirección Y. Para llegar a tales números el modelo de simulación 3D fue utilizado extensivamente para predecir el comportamiento de las estructuras fabricadas posteriormente. En un primer momento, montamos una celda unitaria, la cual utilizamos para hacer un barrido en los parámetros relevantes (altura y lados del rectángulo) con la intención de obtener el mayor 'gap' de energía posible que coincidiera en ambas direcciones. Enseguida, con los parámetros óptimos obtenidos de las simulaciones en celda, hicimos una nueva ronda de simulaciones con el modelo pseudo 3D, en el cual el número de rectángulos en una dirección es simulado exactamente igual al que será utilizado en el dispositivo, sin embargo, en la dirección perpendicular, aplicamos condiciones de contorno periódicas con vistas a reducir el tamaño del modelo y, por tanto, reducir el tiempo de computación. Los resultados experimentales comparados con la simulación se muestra en la figura 5.2.

La principal herramienta utilizada para investigar estos dispositivos fue

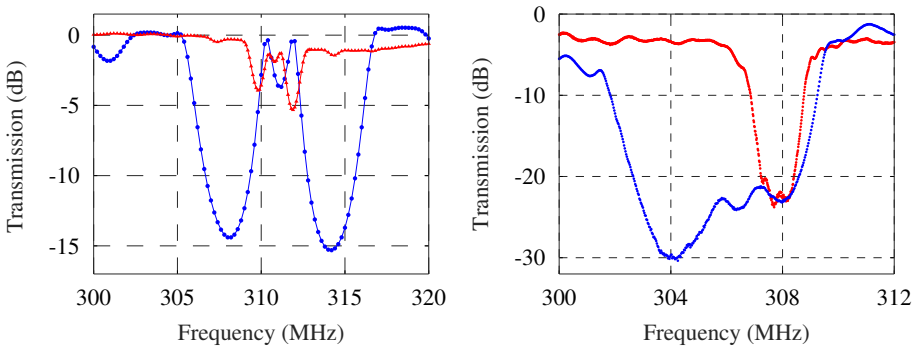

Figure 5.2: Símbolos azules (rojos) corresponden a la dirección X(Y). a) Resultado de la simulación pseudo 3D. Calculamos la transmisión para cada dirección. Para X incluimos dos cavidades de tamaño 7 localizadas entre tres conjuntos de 40 pilares de 120nm de altura. Para Y, las cavidades son de tamaño 9 y utilizamos 120 pilares para cada BR. (b) Transmisión medida para cada dirección, restando la línea de retardo (delay line). Esta muestra consiste de una matriz de 40x120 pilares y cavidades de tamaño 7x11. Alrededor de 307.43 MHz identificamos ambos el segundo pico de la dirección X y el primero pico de la dirección Y, comprobando así el acoplamiento bidimensional.

un modelo de simulación basado en el método de elementos finitos (FEM). Con el desarrollo exitoso del modelo, pudimos predecir el comportamiento de nuestros dispositivos con gran precisión.

Aparte de estos dos últimos resultados presentamos también un tercer resultado clave, alcanzado en estrecha colaboración con el grupo del Prof. Dr. Per Delsing de la Universidad Tecnológica de Chalmers, en Gothemburg, Suecia, durante una estancia allí. Con el uso de una cavidad SAW a muy baja temperatura, estudiamos las fuentes de pérdida en los circuitos cuánticos superconductores. Más específicamente, pérdidas debidas a sistemas de dos niveles (TLS, del inglés *two-level systems*). Los

TLSs son estados de túnel, considerados como sistemas intrínsecos no controlados, que tienen una amplia distribución de división de energía y pueden activarse térmicamente a bajas temperaturas, siendo una fuente importante de pérdida. Nuestros resultados arrojan algo de luz sobre el ancho de línea del conjunto de TLSs y sugieren una forma de mitigar las pérdidas debido a TLS en qubits superconductores.

Dentro del estudio de los circuitos cuánticos superconductores, el llamado sistemas de dos niveles (TLS) se encuentran entre las fuentes más importantes de pérdida que limita el rendimiento de dichos dispositivos. Los TLS son estados de tunelización que tienen una amplia distribución de energía y se pueden activar térmicamente a bajas temperaturas, provocando propiedades anómalas y ruido. Considerado como sistemas intrínsecos incontrolados, se acoplan a ambos campos y colar. Estos estados ocurren debido a defectos en el estructura cristalina o la presencia de impurezas polares. Recientemente, mucho se ha trabajado para comprender sus propiedades y mitigar la pérdidas causadas por TLS. Sin embargo, se han estudiado desde 1960 y ya se desarrolló un modelo TLS bastante establecido en principios de la década de 1970, antes de la aparición de superconductores qubits, en la investigación experimental y teórica sobre las propiedades ultrasónicas de sólidos amorfos. Aunque la naturaleza microscópica de los TLS todavía es no bien entendido, el modelo fenomenológico estándar de tunelización (STM) describe con éxito muchos de los propiedades de los sólidos amorfos, y utilizaremos sus resultados teóricos a lo largo de nuestro análisis. Normalmente, el comportamiento de tales sistemas se estudia midiendo la vidas y frecuencias de resonancia de resonadores superconductores y qubits. No obstante, los TLS tienen una gran influencia en la propagación de ondas sonoras, especialmente en el régimen de baja potencia, siendo un canal de pérdida relevante. Los dispositivos SAW se han utilizado en varios experimentos acústicos, acoplando modos mecánicos a superconductores qubits. Se han demostrado regímenes exóticos de

interacción átomo-campo, así como la generación controlada de estados cuánticos de SAW. También se ha demostrado que los sistemas de dos niveles inducen pérdidas significativas en resonadores SAW a temperaturas criogénicas. La interacción ocurre entre un fonón y un TLS como una absorción seguida de una emisión de otro fonón debido a la relajación TLS. Este mecanismo explica la dependencia de potencia de la atenuación acústica: aumentando la potencia acústica, el nivel superior se satura y, por tanto, el número de TLS efectivos disminuye, lo que disminuye estas pérdidas. Tomamos ventaja del pequeño rango espectral libre (FSR) intrínseco del SAW resonadores para realizar un experimento de espectroscopia de dos tonos. Probar uno resonancia en el régimen de baja potencia mientras se excita a uno vecino con un segundo tono usando mayor potencia podríamos saturar los TLS, recuperando la calidad del resonador. Esta fue la idea. De hecho, la espectroscopia de tonos de TLS se ha realizado utilizando el fundamental y modos armónicos de un resonador de guía de ondas coplanar superconductor, así como más recientemente con los dos modos normales de un sistema de acoplado resonadores. Sin embargo, el espaciado de modo grande de la guía de ondas coplanar los resonadores limitan estos experimentos a un pequeño número de puntos de frecuencia. En nuestros experimentos, como tratamos con SAW, los dispositivos exhiben un espectro con múltiples modos estrechamente espaciados con pequeñas diferencias en la distribución espacial, debido a la corta longitud de onda del sonido. Esto nos permite acceder a un gran número de estados, permitiéndonos sondear la forma del agujero espectral quemado en el conjunto TLS.

Las mediciones se realizaron con un resonador SAW de una puerta, el cual soportaba múltiples modos de resonancia. El dispositivo se colocó dentro de un criostato de diluición que se mantuvo a la temperatura base de 10 mK. Mediamos la reflexión en una resonancia mientras se usaba un generador de señal en la misma puerta para excitar una resonancia

vecina, poblando así los TLSs. Comparado con el caso de medir una resonancia sin excitar ninguna otra, observamos una mejora en la calidad de la resonancia sondada bien como un desvio en frecuencia de su pico. Las medidas experimentales junto con los ajustes basados en el modelo STM se encuentran en la Fig. 5.3.

Nuestras mediciones revelaron la forma del agujero espectral en un conjunto de TLSs hecho a través de una fuerte excitación. Hemos demostrado que la respuesta en la susceptibilidad acústica debida a la excitación está bien modelada cualitativamente por la teoría basada en el STM (acrónimo en inglés para modelo estándar de tunelamiento) [71]. Además, nuestros resultados sugieren el uso de la excitación acústica para mitigar la pérdida de TLS en qubits superconductores. Si bien las mejoras en los métodos de diseño y fabricación han conducido a un rápido aumento de la coherencia en los últimos años, no se han desarrollado medios activos de saturación de TLS debido a la incompatibilidad de los campos de las bombas de microondas con la funcionalidad del dispositivo. Esta limitación no se aplica necesariamente al esquema de excitación acústica que se muestra aquí. Para un agujero espectral debido a una excitación SAW aplicada, es sencillo alcanzar un ancho de línea de varias decenas de MHz, lo que permite excitar con suficiente 'detuning' para evitar excitaciones falsas debido a 'crosstalk', pero aún dentro del rango del agujero espectral. Los resonadores acústicos también tienen una menor sensibilidad intrínseca a la temperatura que los dispositivos superconductores, lo que debería hacerlos muy adecuados para estudiar la dependencia de la temperatura del ruido inducido por TLS y la disipación en un amplio rango de temperatura.

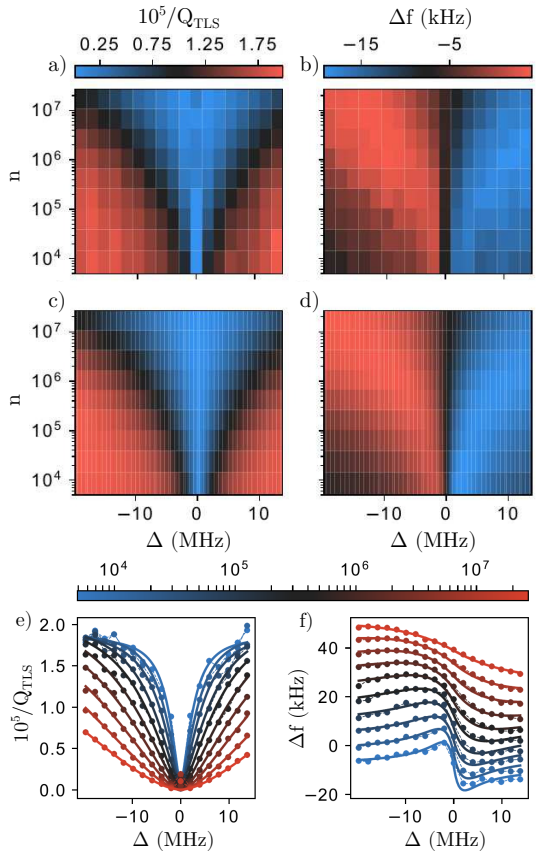

Figure 5.3: Espectroscopia a dos tonos del conjunto TLS. Un tono de excitación es aplicado a una resonancia mientras la respuesta en las otras resonancias es medida en función del 'detuning' Δ y del número de fonónes de la excitación n. Las pérdidas por TLS $1/Q_{TLS}$ se muestran en a). En c) mostramos el ajuste a la eq. 3.3. La excitación del segundo modo también genera un desvio de frecuencia en el modo sob observación - gráfica en b) - con un ajuste a la eq. 3.2 mostrado en d). e) muestra la pérdida como puntos junto con los ajustes a la eq. 3.3 (líneas sólidas), con la escala de color indicando el número de fónones de la excitación. La gráfica correspondiente al desvio en frecuencia es mostrado en f) con una diferencia añadida de 5 kHz offset entre trazos para mejor visualización.

5. RESUMEN EN CASTELLANO

References

[1] Lord Rayleigh. **On waves propagating along the plane surface of an elastic solid**. *Proc. Math. Soc.*, **17**:4–11, 1885. 1, 89

[2] A.E.H. Love. *Some Problems of Geodynamics*. Cambridge University Press, 1911. 1, 89

[3] K. Sezawa. **Dispersion of elastic waves propagated on the surface of stratified bodies and on curved surfaces**. *Bull. Earthquake Res. Inst. Tokyo*, **3**:1–18, 1927. 2, 90

[4] W. S. Mortley. *UK Patent*, **988**(102), May 1963. 2, 90

[5] J. H. Rowen. *U. S. Patent*, **289**(3 114), December 1963. 2, 90

[6] R. M. White and F. W. Voltmer. **Direct piezoelectric coupling to surface elastic waves**. *Appl. Phys. Lett.*, **7**:314–316, 1965. 2, 90

[7] D. P. Morgan. **A history of surface acoustic wave devices**. *International Journal of High Speed Electronics and Systems*, **10**(3):553–602, 2000. 3, 5

[8] Chris Mack. *Fundamental Principles of Optical Lithography: The Science of Microfabrication*. John Wiley & Sons, Ltd, 2007. 6

[9] D. P. Morgan. *Surface Acoustic Wave Filters: With Applications to Electronic Communications and Signal Processing*. Academic Press, 2007. 10, 24

[10] D. L. T. Bell and R. C. M. Li. **Surface-acoustic-wave resonators**. **64**, pages 711–721, May 1976. 11

[11] M. M. de Lima Jr., P. V. Santos, Yu. A. Kosevich, and A. Cantarero. **Tunable coupled surface acoustic cavities**. *Appl. Phys. Lett.*, **100**(261904), 2012. 13, 14, 15, 16, 51

[12] Leonhard Euler (translated by J. D. Blanton). *Introduction to Analysis of the Infinite*. Springer New York, 1988. 18, 93

[13] Schellbach. **Probleme der Variationsrechnung**. *Journal für die reine und Angewandte Mathematik*, **41**:293–363, 1851. 18, 93

[14] R. Courant. **Variational methods for the solution of problems of equilibrium and vibrations**. *Bull. Amer. Math. Soc.*, **49**:1–23, 1943. 18, 93

[15] Y. K. Cheung O. C. Zienkiewicz. *The finite element method in structural and continuum mechanics: numerical solution of problems in structural and continuum mechanics*. McGraw-Hill, 1967. 18, 93

[16] E. Süli. **Lecture Notes on Finite ElementMethods for Partial Differential Equations**. Online at http://people.maths.ox.ac.uk/suli/fem.pdf. 18

[17] C. C. W. Ruppel, W. Ruile, G. Scholl, K. C. Wagner, and O. Manner. **Review of models for low-loss filter design and applications**. *Proceedings of IEEE Ultrasonics Symposium*, **1**:313–324, 1994. 21

[18] V. Plessky and J. Koskela. **Coupling-of-modes analysis of SAW devices**. *International Journal of High Speed Electronics and Systems*, **10**(04):867–947, 2000. 22, 47

[19] Robert D. Cook, David S. Malkus, Michael E. Plesha, and Robert J. Witt. *Concepts and Applications of Finite Element Analysis*. John Wiley & Sons, October 2001. 22, 94

[20] **COMSOL Multiphysics, Release 4.2a (COMSOL Inc., Maine, 2010)**. https://www.comsol.com. 23, 24, 94

[21] W. L. Bond. **The mathematics of the physical properties of crystals**. *The Bell System Technical Journal*, **22**(1):1–72, January 1943. 24

[22] B. Delaunay. **Sur la sphère vide**. *Bulletin de l'Académie des Sciences de l'URSS, Classe des Sciences Mathématiques et Naturelles*, **6**:793–800, 1934. 25

[23] J. P. Bérenger. **A perfectly matched layer for the absorption of electromagnetic waves**. *J. Comput. Phys.*, **114**(1):185–200, 1994. 26

[24] S. G. Johnson. **Notes on Perfectly Matched Layer (PMLs)**. Online at http://math.mit.edu/ stevenj/18.369/pml.pdf, August 2007. 26

[25] **COMSOL Multiphysics ACDC Module User's Guide**. http://www.lmn.pub.ro/ daniel/ElectromagneticModelingDoctoral/Books/COMSOL4.3/acdc/ACDCModuleUsersGuide.pdf. 29

[26] C. G. Montgomery, E. B. Purcell, E. Mills, and R. H. Dicke. *Principles of microwave circuits*. McGraw-Hill, Massachusetts Institute of Technology, Radiation Laboratory, New York, 1948. 35

[27] L. Zhuoyun, A. A. Maznev, A. Mazurenko, and M. Gostein. **Laser-based surfaceacoustic wave spectrometer for industrial applications**. *Internation Conference on Photoacoustic and Photothermal Phenomena*, 2003. 42

[28] T. Omori, K. Hashimoto, H. Kamizuma, L. Yang, and M. Yamaguchi. **High-speedlaser probing system for surface acoustic wave devices based on knife-edge method**. *Jpn. J. Appl. Phys.*, 2005. 42

[29] P. V. Santos. **Acoustic field mapping on gaas using microscopic reflectance andreflectance anisotropy**. *Appl. Phys. Lett.*, 1999. 42

[30] P. T. Tikka, J. V. Knuuttila, and M. M. Salomaa. **Scanning michelson interferometerfor imaging surface acoustic wave fields**. *Optics Letters*, 2000. 42

[31] O. Matsuda, Y. Sugawara, D. H. Hurley, T. Tachizaki, T. Muroya, and O. B. Wright. **Scanning ultrafast sagnac interferometry for imaging two-dimensional surface wavepropagation**. *eview of Scientific Instruments*, 2006. 42

[32] K. Yamanouchi and K. Shibayama. **Propagation and amplification of Rayleigh waves and piezoelectric leaky surface waves in $LiNbO_3$**. *J. Appl. Phys.*, **32**:856–862, 1972. 47

[33] M. M. de Lima Jr., W. Seidel, H. Kostial, and P. V. Santos. **Embedded interdigital transducers for high-frequency surface acoustic waves on GaAs**. *J. of Appl. Phys.*, **96**(6), 2004. 51

[34] Peter S. Cross, William H. Haydl, and Robin S. Smith. **Electronically variable surface-acoustic-wave velocity and tunable SAW resonators**. *Appl. Phys. Lett.*, **28**(1), 1976. 51

[35] Michio Kadota, Yasuyuki Ida, and Tetsuya Kimura. **Band-Pass-Type Tunable Filter Using Surface Acoustic Wave Resonator Composed of Grooved Cu Electrodes on LiNbO3**. *Jpn. J. Appl. Phys*, **51**(07GC14), 2012. 51

[36] Masahiro Inaba, Tatsuya Omori, and Ken ya Hashimoto. **A Configuration of Widely Tunable Surface Acoustic Wave Filter**. *Jpn. J. Appl. Phys.*, **52**(07HD05), 2013. 51

[37] P. Smole, W. Ruile, C. Korden, A. Ludwig, E. Quandt, S. Krassnitzer, and P. Pongratz. In *Proc. of the 2003 IEEE Int. Freq. Contr. Symp. and PDA Exhib.*, 2003. 51, 57

[38] Rui Li, Pavel I. Reyes, Sowmya Ragavendiran, H. Shen, and Yicheng Lu. **Tunable surface acoustic wave device based on acoustoelectric interaction in ZnO/GaN heterostructures**. *Appl. Phys. Lett.*, **107**(073504), 2015. 51, 57

[39] J. Pedrós, F. Calle, R. Cuerdo, J. Grajal, and Z. Bougrioua. **Voltage tunable surface acoustic wave phase shifter on AlGaN/GaN**. *Appl. Phys. Lett.*, **96**(123505), 2010. 51, 57

[40] S. Alzuaga, W. Daniau, R. Salut, T. Baron, S. Ballandras, and E. Defay. **Tunable and high quality factor SrTiO3 surface acoustic wave resonator**. *Appl. Phys. Lett.*, **105**(062901), 2014. 51, 56, 57

[41] M. Schreiter, R. Gabl, D. Pitzer, R. Primig, and W. Wersing. **Electro-acoustic hysteresis behaviour of PZTthin film bulk acoustic resonators**. *J. Eur. Ceram. Soc.*, **24**(1589), 2004. 51, 56, 57

[42] V. F. Dmitriev, G. D. Mansfeld, and V. I. Pustovoit. **Tunable high- Q surface-acoustic-wave resonator**. *Tech. Phys.*, **52**(8), 2007. 51, 57

[43] Z. Huang and T. Wu. **Temperature effect on the bandgaps of surface and bulk acoustic waves in two-dimensional phononic crystals**. *IEEE TUFFC*, **52**(3), 2005. 51, 57

[44] Matthias Weiss and Hubert J. Krenner. **Interfacing quantum emitters with propagating surface acoustic waves**. *J. Phys. D: Appl. Phys.*, **51**(373001), 2018. 52

[45] M. Spletzer, A. Raman, H. Sumali, and J. P. Sullivan. **Highly sensitive mass detection and identification using vibration localization in coupled microcantilever arrays**. *App. Phys. Lett.*, **92**(114102), 2008. 52

[46] J. W. Burgess and M. C. Hales. **Temperature coefficients of frequency in LiNbO3 and LiTaO3 plate resonators**. *Proc. IEEE*, **123**(6), 1976. 53

[47] R. T. Smith and F. S. Welsh. **Temperature Dependence of the Elastic, Piezoelectric, and Dielectric Constants of Lithium Tantalate and Lithium Niobate**. *J. Appl. Phys.*, **42**(2219), 1971. 53, 54

[48] S. Alzuaga, W. Daniau, T. Baron, G. Martin, R. Salut, S. Ballandras, and E. Defaÿ. **SAW resonators using electrostrictive effect**. In *2013 IEEE International Ultrasonics Symposium (IUS)*, pages 749–752, 2013. 56

[49] K. Iamsakun, W. Elder, C. D. W. Wilkinson, and R. M. De La Rue. **Surface acoustic wave devices using electrostrictive transduction**. *J. Phys. D: Appl. Phys.*, **8**, 1975. 56

[50] A. Noeth, T. Yamada, V. O. Sherman, P. Muralt, A. K. Tagantsev, and N. Setter. **Tuning of direct current bias-induced resonances in micromachined Ba0.3Sr0.7TiO3 thin-film capacitors**. *Journ. of Appl. Phys.*, **102**(114110), 2007. 56

[51] Q. M. Chen, T. Zhang, and Q. M. Wang. **Frequency-temperature compensation of piezoelectric resonators by electric DC bias field**. *IEEE TUFFC*, **52**(1627), 2005. 56

[52] A. L. O. Bilobran, A. Garcia-Cristobal, P. V. Santos, A. Cantarero, and Jr. M. M. de Lima. **Thermally Tunable Surface Acoustic Wave Cavities**. *IEEE Transactions on Ultrasonics, Ferroelectrics and Frequency Control*, **67**:850, 2020. 57

[53] G. Andersson, A. L. O. Bilobran, M. Scigliuzzo, M. M. de Lima, J. H. Cole, and P. Delsing. arXiv:2002.09389 [quant-ph]. [link]. 57

[54] J. Burnett, L. Faoro, I. Wisby, V. L. Gurtovoi, A. V. Chernykh, G. M. Mikhailov, V. A. Tulin, R. Shaikhaidarov, V. Antonov, P. J. Meeson, A. Y. Tzalenchuk, and T. Lindström. **Evidence for interacting two-level systems from the 1/f noise of a superconducting resonator**. *Nature Communications*, **5**, 2014. 58

[55] S. E. De Graaf, L. Faoro, J. Burnett, A. A. Adamyan, A. Y. Tzalenchuk, S. E. Kubatkin, T. Lindström, and A. V. Danilov. **Suppression of low-frequency charge noise in superconducting resonators by surface spin desorption**. *Nature Communications*, **9**, 2018. 58

[56] W. A. Phillips. **Tunneling states in amorphous solids**. *Journal of Low Temperature Physics*, **7**(3-4):351–360, 1972. 58, 60

[57] P. W. Anderson, B. I. Halperin, and C. M. Varma. **Anomalous low-temperature thermal properties of glasses and spin glasses**. *Philosophical Magazine*, **25**:1–9, 1972. 58

[58] S. Hunklinger and W. Arnold. **12**, chapter 3 - Ultrasonic Properties of Glasses at Low Temperatures, pages 155–215. Academic Press, 1976. 58

[59] C. Müller, J. H. Cole, and J. Lisenfeld. **Towards understanding two-level-systems in amorphous solids - insights from quantum circuits**. *Reports on Progress in Physics*, **82**(12), 2019. 58, 60

[60] S. Machlup. **Noise in Semiconductors: Spectrum of a Two-Parameter Random Signal**. *Journal of Applied Physics*, **25**(341), 1954. 58

[61] P. Dutta and P. M. Horn. **Low-frequency fluctuations in solids: 1/f noise**. *Reviews of Modern Physics*, **53**(497), 1981. 58

[62] D. P. Pappas, M. R. Vissers, D. S. Wisbey, J. S. Kline, and J. Gao. **Two Level System Loss in Superconducting Microwave Resonators**. *IEEE Transactions on Applied Superconductivity*, **21**(871), 2011. 58, 60, 63

[63] P. V. Klimov, J. Kelly, Z. Chen, M. Neeley, A. Megrant, B. Burkett, R. Barends, K. Arya, B. Chiaro, Y. Chen, A. Dunsworth, A. Fowler, B. Foxen, C. Gidney, M. Giustina, R. Graff, T. Huang, E. Jeffrey, E. Lucero, J. Y. Mutus, O. Naaman, C. Neill, C. Quintana, P. Roushan, D. Sank, A. Vainsencher, J. Wenner, T. C. White, S. Boixo, R. Babbush, V. N. Smelyanskiy, H. Neven, and J. M. Martinis. **Fluctuations of Energy-Relaxation Times in Superconducting Qubits**. *Phys. Rev. Lett.*, **121**(90502), 2018. 58

[64] J. J. Burnett, A. Bengtsson, M. Scigliuzzo, D. Niepce, M. Kudra, P. Delsing, and J. Bylander. **Decoherence benchmarking of superconducting qubits**. *Quantum Information*, **5**(54), 2019. 58

[65] S. Schlör, J. Lisenfeld, C. Müller, A. Bilmes, A. Schneider, D. P. Pappas, A. V. Ustinov, and M. Weides. **Correlating Decoherence**

in Transmon Qubits: Low Frequency Noise by Single Fluctuators. *Phys. Rev. Lett.*, **123**(190502), 2019. 58

[66] M. V. Gustafsson, T. Aref, A. F. Kockum, M. K. Ekstrom, G. Johansson, and P. Delsing. **Propagating phonons coupled to an artificial atom**. *Science*, **346**(207), 2014. 58

[67] B. A. Moores, L. R. Sletten, J. J. Viennot, and K. W. Lehnert. **Cavity Quantum Acoustic Device in the Multimode Strong Coupling Regime**. *Phys. Rev. Lett.*, **120**(227701), 2018. 58

[68] K. J. Satzinger, Y. P. Zhong, H. S. Chang, G. A. Peairs, A. Bienfait, M.-H. Chou, A. Y. Cleland, C. R. Conner, E. Dumur, J. Grebel, I. Gutierrez, B. H. November, R. G. Povey, S. J. Whiteley, D. D. Awschalom, D. I. Schuster, and A. N. Cleland. **Quantum control of surface acoustic-wave phonons**. *Nature*, **563**(661), 2018. 58

[69] R. Manenti, M. J. Peterer, A. Nersisyan, E. B. Magnusson, A. Patterson, and P. J. Leek. **Surface acoustic wave resonators in the quantum regime**. *Physical Review B*, **93**(041411), 2016. 58

[70] J. M. Sage, V. Bolkhovsky, W. D. Oliver, B. Turek, and P. B. Welander. **tudy of loss in superconducting coplanar waveguideresonators**. *Journal of Applied Physics*, **109**(063915), 2011. 59

[71] N. Kirsh, E. Svetitsky, A. L. Burin, M. Schechter, and N. Katz. **Revealing the nonlinear response of a two-level system ensemble using coupled modes**. *Physical Review Materials*, **1**(12601), 2017. 59, 63, 65, 102

[72] John C. Lindon (Editor-In-Chief); George E. Tranterand John L. Holmes (Editors). *Encyclopedia of Spectroscopy and Spectrometry*. Academic Press, San Diego, CA, USA, 2000. 59

[73] U. Fano. **Effects of Configuration Interaction on Intensities and Phase Shifts**. *Phys. Rev.*, **124**(1866), 1961. 61

[74] T. Ida. **An efficient method for calculating asymmetric diffraction peak profiles**. *Review of Scientific Instruments*, **69**(3837), 1998. 62

[75] M. Aspelmeyer, T. J. Kippenberg, and F. Marquardt. **Cavity Optomechanics**. *Reviews of Modern Physics*, **86**(1391), 2014. 63

[76] M. S. Khalil, M. J. A. Stoutimore, F. C. Wellstood, and K. D. Osborn. **An analysis method for asymmetric resonator transmission applied to superconducting devices**. *Journal of Applied Physics*, **111**(054510), 2012. 64

[77] S. Büyükköse, B. Vratzov, J. Van Der Veen, P. V. Santos, and W. G. Van Der Wiel. **Ultrahigh-frequency surface acoustic wave generation for acoustic charge transport in silicon**. *Applied Physics Letters*, **102**(4774388), 2013. 67

[78] M. S. Kushwaha, P. Halevi, L. Dobrzynski, and B. Djafari Rouhani. **Acoustic band structure of periodic elastic composites**. *Phys. Rev. Lett.*, **71**(2):2022–2025, 1993. 68, 91

[79] M. A. Al-Lethawe, M. Addouche, A. Khelif, and S. Guenneau. **All-angle negative refraction for surface acoustic waves in pillar-based two-dimensional phononic structures**. *New J. of Phys.*, **14**(123030), 2012. 68, 91

[80] J. H. Page, P. Sheng, H. P. Schriemer, I. P. Jones, X. D. Jing, and D. A. Weitz. **Group Velocity in Strongly Scattering Media**. *Science*, **271**(634), 1996. 68, 91

[81] W. Dong, X. Ji, J. Huang, T. Zhou, T. Li, Y. Fan, and K. Xu. **Sensitivity enhanced temperature sensor: one-port 2D surface phononic crystal resonator based on AlN/sapphire**. *Semicond. Sci. Technol.*, **34**(055005), 2019. 68, 91

[82] V. Laude, M. Wilm, S. Benchabane, and A. Khelif. **Full band gap for surface acoustic waves in a piezoelectric phononic crystal**. *Phys. Rev. E*, **71**(036607), 2005. 68, 91

[83] A. Khelif, A. Choujaa, S. Benchabane, B. Djafari-Rouhani, and V. Laude. **Experimental study of guiding and filtering of acoustic waves in a two dimensional ultrasonic crystal**. *Z. Kristallogr.*, **220**:836–840, 2005. 68, 91

[84] T. Jiang, Q. He, and Z. Peng. **Enhanced directional acoustic sensing with phononic crystal cavity resonance**. *Appl. Phys. Lett.*, **112**(261902), 2018. 68, 91

[85] A. Sukhovich, L.J. Jing, and J.H. Page. **Negative refraction and focusing of ultrasound in two-dimensional phononic crystals**. *Phys. Rev. B*, **77**(014301):856–862, 2008. 68, 91

[86] A. Sukhovich, B. Merheb, K. Muralidharan, J.O. Vasseur, Y. Pennec, P.A. Deymier, and J. H. Page. **Experimental and theoretical evidence for subwavelength imaging in phononic crystals**. *Phys. Rev. Lett.*, **102**(154301), 2009. 68, 91

[87] A. Khelif, A. Choujaa, S. Benchabane, B. Djafari-Rouhani, and V. Laude. **Guiding and bending of acoustic waves in highly confined phononic crystal waveguides**. *Appl. Phys. Lett.*, **84**(4400), 2004. 68, 92

[88] D. Hatanaka, I. Mahboob, K. Onomitsu, and H. Yamaguchi. **Phonon waveguides for electromechanical circuits**. *Nat. Nanotechnol.*, **9**(520), 2014. 68, 92

[89] T. Jiang, C. Li, and Q. Han. **Surface acoustic waves in 2D-phononic crystal of laminated pillars on a semi-infinite ZnO substrate**. *Phys. Lett. A*, **383**(33):125956, 2019. 68, 92

[90] Y.-F. Wang, T.-T. Wang, J.-P. Liu, Y.-S. Wang, and V. Laude. **Guiding and splitting Lamb waves in coupled-resonator elastic waveguides**. *Comput. Struct.*, **206**(588), 2018. 68, 92

[91] T.-T. Wang, S. Bargiel, F. Lardet-Vieudrin, Y.-F. Wang, Y.-S. Wang, and V. Laude. **Collective resonances of a chain of coupled phononic microresonators**. *Phys. Rev. Appl.*, **13**(014022), 2020. 68, 92

[92] D. Reyes, E. Walker, Y. Zubov, H. Heo, A. Krokhin, and A. Neogi. **All-acoustic signal modulation and logic operation via defect induced cavity effects in phononic crystal coupled-resonator acoustic waveguides**. *New J. Phys.*, **21**(113012), 2019. 68, 92